AN EXPERIMENTAL INVESTIGATION OF TURBINE BLADE HEAT TRANSFER AND TURBINE BLADE TRAILING EDGE COOLING

A Dissertation

by

JUNGHO CHOI

Submitted to the Office of Graduate Studies of
Texas A&M University
in partial fulfillment of the requirements for the degree of

DOCTOR OF PHILOSOPHY

December 2004

Major Subject: Mechanical Engineering

AN EXPERIMENTAL INVESTIGATION OF TURBINE BLADE HEAT TRANSFER AND TURBINE BLADE TRAILING EDGE COOLING

A Dissertation

by

JUNGHO CHOI

Submitted to Texas A&M University
in partial fulfillment of the requirements
for the degree of

DOCTOR OF PHILOSOPHY

Approved as to style and content by:

Je-Chin Han (Chair of Committee)	Dennis O'Neal (Head of Department)
Meinhard T. Schobeiri (Member)	H.C. Chen (Member)
Kenneth D. Kihm (Member)	

December 2004

Major Subject: Mechanical Engineering

ABSTRACT

An Experimental Investigation of Turbine Blade Heat Transfer and Turbine Blade Trailing Edge Cooling. (December 2004)

Jungho Choi, B.S; M.S. Hanyang University

Chair of Advisory Committee: Dr. Je-Chin Han

This experimental study contains two points; part1 – turbine blade heat transfer under low Reynolds number flow conditions, and part 2 – trailing edge cooling and heat transfer. The effect of unsteady wake and free stream turbulence on heat transfer and pressure coefficients of a turbine blade was investigated in low Reynolds number flows. The experiments were performed on a five blade linear cascade in a low speed wind tunnel. A spoked wheel type wake generator and two different turbulence grids were employed to generate different levels of the Strouhal number and turbulence intensity, respectively. The cascade inlet Reynolds number based on blade chord length was varied from 15,700 to 105,000, and the Strouhal number was varied from 0 to 2.96 by changing the rotating wake passing frequency (rod speed) and cascade inlet velocity. A thin foil thermocouple instrumented blade was used to determine the surface heat transfer coefficient.

A liquid crystal technique based on hue value detection was used to measure the heat transfer coefficient on a trailing edge film cooling model and internal model of a gas turbine blade. It was also used to determine the film effectiveness on the trailing edge. For the internal model, Reynolds numbers based on the hydraulic diameter of

the exit slot and exit velocity were 5,000, 10,000, 20,000, and 30,000 and corresponding coolant – to – mainstream velocity ratios were 0.3, 0.6, 1.2, and 1.8 for the external models, respectively. The experiments were performed at two different designs and each design has several different models such as staggered / inline exit, straight / tapered entrance, and smooth / rib entrance. The compressed air was used in coolant air. A circular turbulence grid was employed to upstream in the wind tunnel and square ribs were employed in the inlet chamber to generate turbulence intensity externally and internally, respectively.

NOMENCLATURE

C	airfoil chord length (0.2268 m)
C_p	Pressure Coefficient ($= \frac{P_t - P_s}{0.5\rho V_1^2}$)
D	hydraulic diameter of exit on the trailing edge (m)
d	rotating rod diameter
e	rib height
h	local heat transfer coefficient (W/m^2K)
k	thermal conductivity of air at $23°C$ ($0.02598\ W/mK$)
M	Blowing ratio ($\frac{V_c}{V_m}$)
N	RPM of rotating rod
Nu	local Nusselt number based on blade chord length ($= hC/k$)
n	rotating rod number
P_t	total pressure at cascade inlet (Pa)
P_{s1}	static pressure at cascade inlet (Pa)
P_s	local static pressure on blade surface (Pa)
P	pitch between ribs
q''	local convective heat flux (W/m^2)
q''_{loss}	surface heat loss flux (W/m^2)
q''_{tot}	foil generated surface heat flux (W/m^2)

Re	Reynolds number based on chord length and inlet velocity ($=\frac{V_1 C}{\nu}$)
Re_t	Reynolds number based on hydraulic diameter of slot and exit velocity ($=\frac{V_c D}{\nu}$)
S	Strouhal number ($=\frac{2\pi N d n}{60V}$)
T_c	a mixture of the coolant temperature
T_f	local film temperature
T_i	the initial temperature of the surface
T_m	the mainstream temperature
T_{aw}	local adiabatic wall temperature (°C)
T_w	local surface temperature (°C)
t	the color change time
Tu	local turbulence intensity
$V(i)$	local instantaneous velocity (m/s)
$\overline{V}$	local time mean velocity (m/s)
V_c	averaged exit velocity (m/s)
V_1	cascade inlet velocity (m/s)
V_m	mainstream velocity (m/s)
ν	kinematic viscosity of air ($1.5534 * 10^{-5}\ m^2/s$)
ρ	density of air ($1.1766\ kg/m^3$)
η	the film cooling effectiveness

TABLE OF CONTENTS

Page

Page

LIST OF FIGURES

FIGURE Page

FIGURE Page

FIGURE Page

LIST OF TABLES

TABLE Page

INTRODUCTION AND LITERATURE REVIEW

Blade Heat Transfer and Pressure Coefficient

Flow transition and laminar boundary layer separation in low-pressure turbine blades are attracting increased interest in the industry, due to recent trends such as high altitude flight operations and increased bypass ratios. High-altitude flight operations result in a significant reduction in the gas density and thus a decrease of the Reynolds number inside a gas turbine engine. Turbine airfoils become very sensitive to flow perturbations and highly prone to flow separation, resulting in poor efficiency and higher localized heat transfer to the blades. Noise regulations have driven more manufacturers to offer engines with higher bypass ratios, reduced core flow, and consequently, lower Reynolds numbers. Reduced Reynolds number operation demands that turbine designers more carefully account for viscous effects, including rapid boundary layer growth, laminar-to-turbulence transition, and boundary layer separation. In addition, a recent tendency to reduce the number of blades and stages in turbo-machines has resulted in more highly loaded blades. A static pressure profile associated with increased surface loading tends to extend the transition region length over a larger fraction of the surface and strengthen separation. All these effects have led to increased interest in properly understanding boundary layer transition and flow separation under low-pressure turbine conditions.

This thesis follows the style of International Journal of Heat and Mass Transfer.

Many investigators have addressed the development of boundary layers and separation bubbles in low Reynolds number flows. However, until very recently most of the literature has focused on boundary layer transition as influenced by infinitesimal disturbances. Transition in the turbine engine environment, with elevated disturbance levels and periodic unsteadiness, is less well documented. High levels of mainstream turbulence cause earlier transition compared to lower turbulence levels: Such effects can prevent flow separation in the adverse pressure gradient region in the trailing edge portion of the suction surface of a turbine airfoil. Rivir [1] used an ultra low Reynolds number cascade environment. This study found persistent, massive separation at very low Reynolds numbers (25,000), in spite of elevated mainstream turbulence and added vortices. He also found that elevated mainstream turbulence or added vortices promoted flow reattachment at a higher Reynolds number. Volino et al. [2,3] documented boundary layer separation, transition and reattachment under Reynolds number and pressure gradient conditions typical of LPT airfoils. They concluded that Reynolds number and free-stream turbulence level do not have a significant effect on boundary layer separation unless they are high enough to induce transition upstream of separation while the location and extent of the transition zone, in contrast, depends strongly on Reynolds number and turbulence intensity. Van Treuren et al. [4] documented pressure distributions, loss coefficients, and the separation zones in a turbine cascade flow under low Reynolds number (25,000 – 50,000) conditions. They observed persistent massive separation at very low Reynolds numbers (25,000), in spite of the elevated mainstream turbulence and added vortices. However, at a higher Reynolds number of 50,000, flow

reattachment with elevated mainstream turbulence or with added vortices was eminent. Meinhard T. Schobeiri et al. [5,6] investigated boundary layer development, separation, and re-attachment along the low pressure turbine blade surface under unsteady flow condition. They observed that passing wake flow with its turbulent vertical core over the separation region caused a periodic contraction and expansion of the separation zone and unsteady wake flow reduce the losses due to the suppressed or reduced separation boundary layer. They addressed that fluctuation gradient is important factor to determine suppressing or preventing the onset and extent of the separation zone.

Many studies have investigated the fluid flow and heat transfer behavior in high Reynolds number flows. Blair [7,8] investigated the effect of grid generated turbulence on flat plate heat transfer. He showed that turbulent heat transfer coefficient in flow with for 6% grid-generated turbulence intensity increased by 18% compared to that without grid. Simonich and Bradshaw [9] and Hancock and Bradshaw [10] reported similar results. O'Brien and VanFossen [11] investigated the influence of jet-grid-generated turbulence on heat transfer from the leading edge of a circular cylinder in cross flow. They reported that for cylinder Reynolds numbers 48,000-180,000, the heat transfer coefficient for a turbulence intensity of 10-12% increases by 37-53% compared to the case with zero turbulence intensity. Bellows and Mayle [12] tested the heat transfer downstream of a leading edge separation bubble on a blunt body. They indicated that the heat transfer through a separation region and for the turbulence intensity of 0.4% increases almost an order of magnitude and is about 50% higher near the reattachment region than is predicted by the turbulent flat plate correlation.

Mehendale et al. [13] studied the effect of jet-grid-generated turbulence on leading edge heat transfer and found an increase of up to 50%. They also found that the inflow turbulence intensity (up to 15%) does not shift the location of the separation-reattachment region. The reattachment heat transfer coefficients are the same despite the inflow turbulence levels and are much higher than the values for the heat transfer coefficient in turbulent flat plate. Brown and Martin [14,15] investigated free-stream turbulence effects on turbine blade heat transfer coefficients. They reported that at gas turbine conditions, the scale and frequency of free-stream turbulence may be as important as its intensity in determining local heat transfer coefficients around the blade. Zhang and Han [16] studied the influence of mainstream turbulence on the surface heat transfer coefficient of a gas turbine blade. Their mainstream Reynolds numbers ranged from 100,000 to 300,000, based on the cascade inlet velocity and blade chord length. Their results showed that mainstream turbulence promoted earlier and broader boundary layer transition, caused higher heat transfer coefficients on the suction surface, and significantly enhanced the heat transfer coefficients on the pressure surface. They also showed that heat transfer coefficient augmentation on the suction surface increases and its peak ratio moves forward with increased mainstream turbulence level. Han et al. [17] studied the effect of unsteady wake on surface heat transfer coefficient of a gas turbine blade using a spoked wheel type wake generator. Their mainstream Reynolds numbers ranged from 100,000 to 300,000. Their results showed that the unsteady passing wake promoted earlier and broader boundary layer transition and caused higher heat transfer coefficients on both the suction surface and pressure surface. Ames [18] investigated the

influence of combustor simulated turbulence on turbine vane heat transfer for Re=790,000 (based on axial chord). He reported that transition occurred on the suction surface during which the heat transfer level increased rapidly. He also showed a strong effect of turbulence length scale on heat transfer.

Many studies have investigated on the effect of unsteady wake caused by the passing of upstream blade row. Many published results investigate the interaction between the wake flow and the boundary layer on the suction side of a turbine blade. It is well known that the unsteady wake impact causes an increased stagnation region heat transfer and an early laminar-turbulent boundary layer transition. This wake induced earlier transition covers a longer streamwise length on the suction surface of a turbine blade. Experiments have been conducted in turbines (Dunn [19], Dunn et al. [20,21], Blair et al. [7], and Abhari et al. [22]) or in laboratory simulations (O'Brien and Capp [23], Liu and Rodi [24], Dullenkopf et al. [25]). A squirrel cage type wake generator was used in laboratory simulations by Liu and Rodi [24]. However, a spoke wheel type wake generator was employed by O'Brien and Capp [23] Some investigators (Dunn et al. [20,21] and Abhari et al.[22]) used fast response sensors to detect the real time variation on the blade surface heat transfer induced by unsteady wake, while other researchers (Liu and Rodi [24], Dullenkopf et al. [25] and Blair et al.[7]) employed the standard method to obtain the mean (time-averaged) heat transfer on an airfoil in unsteady wake conditions. Mayle[26] developed a theory to incorporate the unsteady effect into a steady-flow analysis by introducing a time-averaged intermittency factor. They showed that the time-averaged heat transfer distribution on the airfoil surface can

be obtained from the predicted time-averaged intermittency factor and the laminar and turbulent heat transfer distributions as calculated from steady-flow conditions. They also found that the theory agrees with the measurement of the time-averaged heat transfer coefficient on the suction surface of a turbine blade in a spoked wheel generated wake flow condition.

It is well known that the turbine blade heat transfer coefficient varies with the wake Strouhal number. The wake Strouhal number is defined as the relative strength of the wake tangential velocity to the mainstream axial velocity, while the wake tangential velocity is proportional to the rotating rod rotational speed, the rotating rod number, and the rotating rod diameter. This means that the wake Strouhal number is composed of four variables: the rotating rod speed, rod number, rod diameter, and mainstream velocity. Zhang and Han [16] showed there is no combined effect with changing the four variables if Strouhal numbers are same. As mentioned, flow separation results in higher localized heat transfer in low-pressure turbine blades. However, to the knowledge of the authors, there is no investigation reported in the literature that has taken a close look not only at the flow separation and pressure loss, but also the Nusselt number distributions associated with flow separation in turbine blade cascade at low Reynolds number conditions. The main objective of this study is to provide both pressure coefficient and Nusselt number distributions on the surfaces of a turbine blade at low Reynolds number flows. This study also reports the effect of increasing Reynolds number from 15,700 to 105,000 and free-stream turbulence intensity from 0.6% to15.31% in suppressing separation, promoting boundary layer transition, and enhancing

heat transfer on blade surfaces. The experimental data presented in this paper have been used for calibrating DNS (Direct Numerical Simulation) calculating of turbine blade flow transition and heat transfer (Alabi [27]). The present study also represents a continuation of Zhang and Han [16] who studied turbine blade heat transfer at higher Reynolds number flows from 100,000 to 300,000

Trailing Edge Heat Transfer and Film Effectiveness

In modern gas turbine engines, thermal efficiency and power output of a gas turbine increase with increasing turbine inlet temperature. Since the level is close to the maximum allowable for the blade material, usually several cooling technique (shown in Figure 1), such as internal convective cooling and film cooling, are used to cool the hot blade. One of the hardest regions to cool is the trailing edge because the trailing edge must be thin to reduce aerodynamic losses. This cause a conflict with cooling requirement because manufacturing difficulty arises on internal cooling passage in the trailing edge. One of the cooling techniques in the trailing edge is using spanwise slots, which are obtained by removing material in the pressure side surface, and jet impingement blockage to increase internal heat transfer.

Detailed surveys of published studies on the internal cooling of gas turbine airfoils have been presented in Han et al. [28]. Many researchers have studied heat transfer enhancement in channels with turbulence promoters, pin fins, and impinging jets, with and without rotation. There have been number of studies of heat transfer for turbulent flows through channels with perforated ribs or ribs with various opening for flows to pass through, such as Kukreja and Lau [29], Hwang et al. [30], Liou and Chen

[31], and Buchlin [32]. Kukreja and Lau [29] conducted experiments using the transient liquid crystal technique to measure the local heat transfer distributions for turbulent flows through square channel with solid and perforated ribs on two opposite wall. The results showed that solid ribs enhanced more overall heat transfer and the pressure drop than perforated ribs. Increasing the size of the holes, number of holes, or the total hole area did not effect the heat transfer enhancement. Buchlin [32] tested five different type, such as perforated ribs, bottom hole, tilted hole, arch, column, and chevron type. He observed an increase of the local heat transfer immediately downstream of the perforated ribs and recommended an optimal design with chevron type perforated ribs. Moon et al. [33] investigated heat transfer between two blockages with holes and pressure drop across the blockage for turbulent flow in a rectangular channel using the mass transfer technique. They found that the jet impingement by the blockage with holes enhanced heat transfer five to eight times, but the pressure drop also increased significantly. Smaller holes in the blockage caused higher heat transfer and larger pressure drop also. They also observed that the local heat transfer was the lowest immediately downstream of the holes in the upstream blockage, the highest upstream of the downstream blockage, and relatively high in the region of reattachment of the jets. However, they mentioned the local heat transfer distribution was strongly dependent on the hole array configuration. Lau et al. [34] studied at different holes geometry in the blockage, such as round and square holes. They showed that the blockage with round holes enhanced more heat (mass) transfer on the wall. The result showed the square holes blockage

enhanced more heat (mass) transfer and larger pressure drop than the round holes blockage.

Several studies have been performed film cooling effectiveness in the trailing edge. A comprehensive survey of film cooling was investigated and complied by Goldstein [35] which includes data for discrete holes as well as slots. It has been well established that the slot coolant to mainstream flow blowing ratio and normalized distance downstream of slot breakout are key parameters to which film effectiveness is correlated. However, other parameters such as slot to mainstream flow density ratio, slot lip thickness to height ratio, slot width to height ratio, slot angle of injection relative to mainstream flow and main stream flow acceleration are recognized as having effects of various magnitudes on slot film effectiveness but are not as well established. Wieghardt [36] conducted an experimental study injecting heated flow out of slots angled 30 degree to the mainstream. For small temperature differences between mainstream and slot flow, as was the case in Wieghardt's study, where the flow can be considered of constant properties, the film effectiveness should be independent of whether the slot is hotter or colder than mainstream flow. Kicker and Whitelaw [37,38] investigated the influence of slot height, slot-lip-thickness and slot turbulence intensity on the film effectiveness for a uniform density, two dimensional wall jet. Papell [39] investigated the effects of slot angle (α) of injection relative to mainstream flow on film effectiveness and made measurements for α = 45, 80 and 90 degree. The measurements were carried out with large density ratios, small slot lip thickness to height ratio and Mach numbers mainly greater than 0.5. The investigation significant decrease in slot film effectiveness as α

increased. Goldstein et al. [40] conducted an experimental study of film cooling effects produced by injection of helium and air secondary flow through porous section into a turbulence boundary layer of air flowing over a flat plate. Nicoll and Whitelaw [41] measured the effectiveness of a two-dimensional wall jet by injecting helium through a slot into an air mainstream for a range of slot to free stream mass velocity ratios. A comparison was made between the experimental data and their predicted results as well. Rastogi and Whitelaw [42] and Patankar et al. [43] reported experimental results for the adiabatic wall effectiveness down stream of three-dimensional slots made up of discrete holes discharging parallel to the mainstream. Paxson and Mayle [44] performed theoretical and experimental investigations on the influence of the mainstream thermal boundary on film effectiveness. Nina et al. [45] and Taslim [46] investigated adiabatic film cooling effectiveness of different slot geometries. Taslim [46] showed that the film effectiveness is strongly sensitive to the exit slot thickness to height ratio in the range from 0.5 to 1.25. Rastogi et al. [42] studied the impervious wall effectiveness of three dimensional slot geometries. They concluded an increase of lip thickness and pitch to diameter ratio lead to a decrease in film effectiveness. Sturgess [47,48] focused on combustor slots with a circular inlet followed by a lip overhang acting as a mixing chamber. Martini et al. [49] extended to the use of a rib array near the trailing edge. They showed this type of cooling configuration is not desirable for film cooling on the trailing edge cutback. However, there is no investigation of the combined effects with jet impingement inside on the trailing edge film cooling and the turning flow effect on the trailing edge heat transfer.

INSTRUMENTATION

Blade Heat Transfer and Pressure Coefficient

The experiment was performed in a low speed wind tunnel as shown in Figure 2(a) and (b). The wind tunnel consisted of two screens, a contraction nozzle, a wake generator, a five-blade linear cascade, and a blower. The wind tunnel was of the suction type so as to reduce unexpected turbulence intensity in the main stream flow. The 4.5:1 contraction nozzle produced uniform flow entering the test channel. The test channel was 25.4 cm high, 75.0 cm wide in cross section, and had a 107.49° turn to fit the turning of the five-blade cascade.

Twenty-six pressure taps were instrumented in the mid-span of a test blade to measure the pressure and velocity distributions around the blade (Zhang and Han [16]). There was one pressure tap at the leading edge (stagnation point), 11 on the pressure side and 14 on the suction side of the blade. The pressure taps were connected to micro manometer to measure the blade surface static pressure. The micro manometer had an accuracy of 0.00025 inches of water. A pitot-probe also measured mainstream flow velocity at the inlet and exit of the cascade. Figure 3 shows a test blade instrumented with thin foil heaters to provide constant heat flux on the blade surface and thermocouples to measure the surface heat transfer coefficients. Twenty-six stainless steel strips were vertically cemented on the outer surface of the instrumented blade (Zhang and Han [16]). Each foil strip was 25.4 cm long, 1.75 cm wide, and 0.038 mm thick. All the thin foils were connected in series by copper bus bars. The thin foil strips

produce a constant heat flux condition on the blade surface by maintaining a constant voltage in the circuit. A T-type thermocouple was soldered at 3 different locations in mid-span portion of each foil. All thermocouple output data were analyzed by a Fluke data logger and a PC and were averaged at each x/C location.

Figure 4 shows two types of turbulence grids used to create different levels of turbulence intensity. The coarse grid, shown in Figure 4(a), was designed to generate higher turbulence intensities. It was made of steel square tubes with a width of 1.3 cm and a pitch of 4.8 cm. The fine grid, shown in Figure 4(b), was designed to generate lower turbulence intensities. It was made of steel square bars with a width of 0.5 cm and a pitch of 1.9 cm. The grids were placed upstream of and parallel to the leading edge plane of the blade cascade. Two grid locations were selected in this study, i.e., 21 cm and 60 cm from the cascade leading edge. Figure 5 shows the four different *s/d* locations and their corresponding turbulence intensities measured at the cascade inlet for each of the four Reynolds numbers.

The wake simulation was achieved by means of the rotating spoked wheel shown in Fig. 6. The wake Strouhal number (S) is used to simulate the unsteady wake flow characteristics of modern gas turbines (O'Brien and Capp[23]) and is defined as

$$S = \frac{2\pi N d n}{60 V}$$

where N is the rotational rod speed (RPM.), d is the rod diameter (m), n is the number of rods, and V is the mainstream flow velocity at the inlet cascade (m/s). Diverse Strouhal numbers can be tested by varying the rotational speed, rod diameter, rod number, and flow inlet velocity. Zhang and Han [16] showed that the heat transfer

coefficient is the same at the same Strouhal number even though rotating speed, rod diameter, and rod number are different. Fig. 7 shows the conceptual view of the effect of the unsteady wake on the blade. Mainstream, disturbed by rotating rod, not only increases turbulence intensity but also changes flow direction. Zhang and Han [16] presented the turbulence, measured by an ensemble average technique, is enhanced by the wake, but the peak value does not change regardless of the Strouhal number at a given Reynolds number. This study focuses on the flow deflection by the wake, which changes the angle of attack on the leading edge of the blade. In this study, Strouhal number ranges from 0.0 to 2.96 by changing the rotating rod speed as shown Fig. 8.

Trailing Edge Heat Transfer and Film Effectiveness

Figure 9 shows a schematic of the trailing edge film cooling model. The external model, scaled up by 5 times, is mounted in a low speed suction type wind tunnel up to a maximum velocity of 34 m/s. The 2.3:1 contraction nozzle produces uniform flow at the entrance of the test section. The test channel was 15.56 cm high and 30.5 cm in the cross section. A central air-conditioning system maintained mainstream temperature at 28°C. Figure 10 shows a detail inside view of the model. The ¼" square ribs and two jet impingements are inserted to increase internal heat transfer. Total seven different trailing edge models were tested; those are (1) staggered exit slot, (2) inline exit slot and (3) rib entrance for design 1, shown in Figures 11, and (4) straight entrance, (5) tapered entrance, (6) rib entrance and (7) rib entrance with turbulence grid for design 2, shown in Figure 12 and Table 1. The main difference of two designs are (1) the land slope at the exit in the film cooling and (2) entrance effect between the slot and second chamber in

the internal cooling. The jet impingement of both designs is arranged in a staggered series to increase internal heat transfer. Two different liquid crystals are used to determine the internal heat transfer coefficient, such as R34C20W in the inlet chamber and R29C5W in the first and second chamber since the heat transfer coefficient in the inlet chamber is much lower than in the other chambers. The thermal conductivity and diffusivity of the model are 0.1812 and $1.073*10^{-7}$, respectively.

Table 1. Conceptual Design Characteristic

Design number	Geometry		Turbulence grid
	Inlet	Exit	
1	Straight	Staggered	x
	Straight	Inline	x
	Rib	Staggered	x
2	Straight	Staggered	x
	Tapered	Staggered	x
	Rib	Staggered	x
	Rib	Staggered	o

In Figure 13, 17 thermocouples or 15 pressure taps are instrumented to measure either coolant temperature or pressure distribution. Five thermocouples (or pressure

taps) at each chamber are instrumented in the staggered series for the internal cooling case and 2 thermocouples are instrumented before the coolant exit region for the film cooling case. Those thermocouples (pressure taps) are connected to data logger (micro manometer).

For the heat transfer coefficient calculation case, the transient hue value detection technique is used. The test surface is heated uniformly using the removable heater. After the surface is heated to desired temperature (110 F), the heater is removed, the wind tunnel is started, coolant air is ejected, and the image processing system is triggered simultaneously. The time required for the hue value to reach 50 at each pixel location is measured by the image processing system. On the other hand, the steady hue value detection technique is used for the film effectiveness case. The coolant air is heated by pipe heaters, while the mainstream flow is not heated. When it reaches in steady state, the image processing system captures the image of the liquid crystal color. In this study, four velocity ratios ($M=V_c/V_m$) range from 0.3 to 1.8 by changing coolant air velocity. Corresponding Reynolds number ranges from 5,000 to 30,000. The Reynolds numbers is defined as

$$\mathrm{Re}_t = \frac{V_c D}{\nu}$$

where V_c is the averaged coolant velocity, and D is hydraulic diameter of exit slot.

MEASUREMENT THEORY

Blade Heat Transfer and Pressure Coefficients

Pressure measurements were expressed as the pressure coefficient:

$$C_p = \frac{P_t - P_s}{0.5\rho V_1^2} = \frac{(P_t - P_{s1}) - (P_s - P_{s1})}{P_t - P_{s1}}$$

where P_t is the total pressure of the mainstream flow at the cascade inlet. P_{s1} and P_s are the static pressure at cascade inlet and local static pressure on blade surface. The total pressure is different at each location due to pressure loss along the blade surface. The numerator of the above equation equals to the sum of the dynamic pressure at the cascade inlet and the pressure loss of a point on the blade surface. At a given Reynolds number, a higher pressure coefficient indicates higher pressure loss. The local heat transfer coefficient is calculated as

$$h = \frac{q''}{T_w - T_\infty} = \frac{q''_{tot} - q''_{loss}}{T_w - T_{aw}}$$

where q'' is the local convective heat flux from the foil surface, q''_{tot} is the total heat flux from the foil heater, and q''_{loss}, affected by conduction, natural convection and radiation, is local the heat loss, which is a function of the difference between the wall temperature (T_w) and the adiabatic wall temperature (T_{aw}). The local adiabatic wall temperature (T_{aw}) was measured at the same Reynolds number condition but without any heat input. T_w was in the 40-50°C range while T_{aw} was about 25°C. The local heat

transfer coefficient was converted into the local Nusselt number ($Nu = hC / k$), where C is the blade chord length and k is air thermal conductivity. Heat loss tests were conducted for the test blade at no-flow condition. Heat losses were calibrated by supplying power to the test blade until steady state. Several different power inputs were tested to obtain the correlation between the total heat loss and the individual foil temperature. Heat loss through the tiny thermocouple wires was less than 0.1%, and axial and lateral conduction through the thin foil was found to be negligible.

Trailing Edge Heat Transfer and Film Effectiveness

A hue detection based transient liquid crystal technique is used to measure heat transfer coefficient on the trailing edge and internally. The local heat transfer coefficient over the liquid crystal coated surface can be obtained using the one dimensional semi-infinite solid assumption for the surface. The 1-D transient conduction equation, the initial condition and the boundary condition are:

$$k\frac{\partial^2 T}{\partial x^2} = \rho c_p \frac{\partial T}{\partial t}$$

$$at \quad t = 0, \quad T = T_i$$

$$at \quad x = 0, \quad -k\frac{\partial T}{\partial X} = h(T_w - T_m); \quad as \quad x \to \infty, \quad T = T_i$$

The solution to the above equation at the convective boundary surface (x=0) is the following:

$$\frac{T_w - T_i}{T_m - T_i} = 1 - \exp\left(\frac{h^2 \alpha t}{k^2}\right) erfc\left(\frac{h\sqrt{\alpha t}}{k}\right)$$

By knowing the initial temperature (T_i) of the surface, the mainstream temperature (T_m) in the wind tunnel, the color change temperature (T_w) and the color change time (t), the local heat transfer coefficient (h) can be calculated from above equation.

For the internal cooling case, the mainstream temperature, initially hot by heated test section, is decreasing continuously during the experiment. Using Duhamel's superposition theorem (kwak et al [50]), equation can be written as;

$$T_w - T_i = \left(T_{m,0} - T_i\right) \times F\left(\frac{h\sqrt{\alpha t}}{k}\right) + \sum_{i=1}^{n}\left[F\left(\frac{h\sqrt{\alpha\left(t-\tau_i\right)}}{k}\right)\Delta T_{m,i}\right]$$

where, $F(x) = 1 - \exp(x^2) erfc(x)$

ΔT_m : step change in the mainstream of τ_i

For the film cooling test, the mainstream temperature in equation is replaced the by local film temperature (T_f), which is a mixture of the coolant temperature (T_c) and mainstream temperature. The film temperature is defined in terms of the film cooling effectiveness (η);

$$\eta = \frac{T_f - T_m}{T_c - T_m} \quad or \quad T_f = \eta T_c + (1-\eta) T_m$$

Two different tests can be run to obtain the heat transfer coefficient (h) and the film effectiveness (η). In the first test, the surface of the test model is not heated while

the coolant air is hot (up to 100F). When it reaches to steady state, the film temperature (T_f) can be replaced by adiabatic wall temperature (T_{aw}), which is determined by the color of the liquid crystal and defined as;

$$\eta = \frac{T_{aw} - T_m}{T_c - T_m}$$

In the second test, the test surface is heated while the coolant temperature (T_c) is not heated but the temperature varies from the mainstream temperature (T_m). Above two equations are solved at each pixel to obtain the detailed heat transfer coefficients and film cooling effectiveness.

UNCERTAINTY ANALYSIS

Table 2 gives the maximum uncertainties for Nusselt numbers and pressure coefficients under different test conditions. For the four Reynolds numbers tested in this study, the maximum uncertainty for Nusselt number is between 8.23% and 9.8% for the leading edge and is less than 3.92% for areas other than the leading edge. The uncertainties of velocity and pressure measurement for trailing edge test are shown in table 3. Generally, uncertainty decreases as increase Reynolds number due to pressure transeducer.

Table 2. Maximum Uncertainties for Nusselt Number and Pressure Coefficient Measurements for Blade Heat Transfer

Re	Nu(%)		C_p(%)		
	Leading edge only (x/c = 0.077)	Except leading edge	Pressure side	Suction side	Leading edge
105,000	9.8	3.92	3.54	3.54	3.54
52,000	9.4	3.03	3.75	3.54	4
31,400	8.23	3.5	6.54	3.56	8.7
15,700	9.1	3.6	31.4	4.2	62.6

Table 3. Maximum Uncertainties in Velocity and Pressure Coefficient Measurements for Trailing Edge Transfer

Re	Velocity (%)	pressure (%)
105,000	1.8	2
52,000	3.03	2.8
31,400	6.3	5.3
15,700	10.2	13.8

RESULTS AND DISCUSSION

Pressure Coefficient on the Blade

The periodicity of the velocity profiles between adjacent flow paths and the velocity profiles in the radial direction at the inlet and outlet of the central flow path and at the inlet and outlet of an adjacent flow path have been obtained (Zhang and Han [19]). The results indicated that the periodicity of velocity profile between adjacent flow paths was excellent and the flow direction at the inlet and outlet of both flow paths was uniform. Also, the inlet and outlet velocity profile was essentially uniform between a 25 and 75 percent span.

Effects of Reynolds Number: In Figure 14(a), the local pressure coefficients (C_p) for four Reynolds numbers without grid turbulence are presented to show the effect of Reynolds number on local pressure coefficient. The local pressure coefficient is presented as a function of the normalized distance (x/C) from the leading edge along the blade surface to a local position. On the suction surface, the local pressure coefficient increases along the stream-wise direction until x/C ≅ 0.7, indicating flow acceleration at the upstream portion of the suction surface. The peak at x/C ≅ 0.7 corresponds to the highest velocity on the suction surface. The local pressure coefficient slightly decreases after the peak, until x/C ≅ 1, at which point the flow begins to separate. At a given location on the suction surface, the local pressure coefficient increases as Reynolds number decreases. The difference between the two pressure coefficient curves, each corresponding to a different Reynolds number, increases as x/C increases. The effect of

Reynolds number on local pressure coefficient becomes negligible when the Reynolds number is reduced to 30,000. On the pressure surface, there is a region of low-velocity flow near the leading edge. The local pressure coefficient remains low and quite stable in the upstream portion ($x/C < 0.4$), and slightly increases as the mainstream flows downstream and starts to accelerate. The local pressure coefficient on the pressure surface decreases with decreasing Reynolds number from 105,000 to 52,000. However, the reverse is true for $x/C > 0.6$. The effect of Reynolds number on local pressure coefficient on the pressure surface is small when Reynolds number is lower than 52,000.

Figures 14(b) through 14(e) present the local pressure coefficient at different Reynolds numbers for the four grid cases, i.e., fine and coarse grids at position #1 (21 cm upstream) and position #2 (60 cm upstream). The effect of Reynolds number on local pressure coefficient for all four grid cases is similar to that for the no-grid case. There is, at a given location on the suction surface, the lower the Reynolds number, the higher the local pressure coefficient. For the two cases with comparatively low turbulence intensity (fine and coarse grids at position #2), the effect of Reynolds number on local pressure coefficient becomes negligible when the Reynolds number is reduced to 30,000. However, on the pressure surface, local pressure coefficient trends to increase with decreasing Reynolds number.

Effects of Turbulence Intensity: Figures 15(a) through 15(d) show the effects of turbulence intensity on the local pressure coefficient at a given Reynolds number. In the Re=105,000 case shown in figure 15(a), the local pressure coefficient on the suction surface increases as turbulence intensity increases, indicating that higher turbulence

intensity results in higher pressure loss. Interestingly, for intensities of about the same value, the coarse grid-generated turbulence intensity (5.34%) has a stronger effect on the local pressure coefficient than does the fine grid-generated turbulence intensity (6.67%). This suggests that turbulence length scale might affect pressure loss. Also, the turbulence intensity effect tends to level off when the turbulence intensity reaches certain high values as shown in Fig. 15(a). On the pressure side, the local pressure coefficient decreases as turbulence intensity increases because higher turbulence intensity impedes flow separation near the leading edge. Figure 15(b), 15(c), and 15(d) show the effects of turbulence intensity on local pressure coefficient at Re = 52,000, 31,400, and 15,700, respectively. The same trend is observed from both figures 15(b), 15(c) and 15(d) as from 15(a), but the effect of turbulence intensity on local pressure coefficient decreases as Reynolds number decreases.

*Effects of Unsteady Wake***:** The periodicity of the velocity profiles between adjacent flow paths has been measured and confirmed. The velocity profiles in the radial direction for four Reynolds numbers (Re = 105,000, 52,000, 31,400, and 15,700) at the inlet and outlet of the central flow path and at the inlet and outlet of an adjacent flow path have been obtained. The results indicate that the inlet and outlet velocity profile is essentially uniform between a 25 and 75 percent span (Zhang and Han[21]) . Thus, the Nusselt numbers are free from the top and bottom wall boundary layer effects. The periodicity of velocity profile between adjacent flow paths is excellent. Also, the flow direction at the inlet and outlet of both flow paths is uniform.

The pressure tap blade provides the static pressure distribution at the blade surface and pitot-probe presents the total pressure near the leading edge which was used to calculate the pressure coefficient. Figures 16(a) through 16(d) show the effect of Strouhal number on the local pressure coefficient at a given Reynolds number. The local pressure coefficient is presented as a function of the normalized distance (x/C) from leading edge along the blade surface to a local position. In the Re = 105,000 case shown in figure 16(a), the local pressure coefficient increases along the streamwise direction until $x/C \cong 0.7$, indicating flow acceleration at the upstream portion of the suction surface. The peak at $x/C \cong 0.7$ corresponds to the highest velocity on the suction surface. The local pressure coefficient slightly decreases after the peak. At the given location, the local pressure coefficient on the suction surface decreases as Strouhal number increases until $x/C \cong 0.2$ and reverses after that. Near the leading edge ($x/C < 0.2$), higher Strouhal number gives the lower pressure coefficient, indicating to increase the static pressure more due to change of the angle of attack on the leading edge. However, higher Strouhal number provides higher pressure coefficient, indicating more pressure loss due to increased turbulence intensity, at a given location. On the pressure side, the local pressure coefficient decreases as Strouhal number increases because higher turbulence intensity impedes a flow separation near the pressure side leading edge. Figure 16(b), 16(c), and 16(d) show the effect of Strouhal number on the local pressure coefficient at Re = 52,000, 31,400, and 15,700, respectively. The same trends are observed from both figures 16(b), 16(c) and 16(d) as from figure 16(a). The reverse

gradient at the x/C < 0.2 is also observed for high Strouhal number (S > 1), i.e. pressure coefficient on the suction surface is higher than on the suction surface at given location.

*Combined Effect of Reynolds Number and Strouhal number***:** Figure 17(a), the local pressure coefficients (C_p) for four Reynolds numbers at 0 RPM condition, presents the effect of Reynolds number on local pressure coefficient. At a given location on the suction surface, the local pressure coefficient increases as Reynolds number decreases. The difference between the two pressure coefficient curves, each corresponding to different Reynolds number, increases as x/C increases up to x/C ≅ 0.7 and does not increase after x/C ≅ 0.7. The effect of Reynolds number on local pressure coefficient becomes negligible when the Reynolds number is reduced to 30,000. On the pressure surface, there is a region of low-velocity flow near the leading edge. The local pressure coefficient remains low and quite stable in the upstream portion (x/C < 0.4), and slightly increases as the mainstream flows downstream and starts to accelerate. The local pressure coefficient on the pressure surface decrease as Reynolds number decreases from 105,000 to 52,000. However, the reverse is true for x/C > 0.6. The effect of Reynolds number on local pressure coefficient on the pressure surface is small when Reynolds number is lower than 52,000.

Figures 17(b), 17(c), and 17(d) present the combined effect of Reynolds number and Strouhal number for the three different rotating rod cases (50, 100, and 150 RPM respectively). Compared with figure 17(a), increasing Strouhal number increases the pressure coefficient at a given location due to pressure loss, except near leading edge suction surface region (x/C < 0.2). Near the leading edge region on the suction surface

(x/C < 0.2), decreasing Reynolds number and increasing Strouhal number decrease local pressure coefficient: indicating Strouhal number effect is more dominate than Reynolds number effect.

Heat Transfer Coefficient on the Blade

Effects of Reynolds Number: Figure 18(a) presents the effect of Reynolds number on local Nusselt number distribution for the case without a turbulence grid. The positive and negative abscissa (x/C) indicates the streamwise distance along suction surface and pressure surface, respectively. On the suction surface, the Nusselt number decreases monotonically with increasing streamwise distance due to laminar boundary layer growth. At a given location, the Nusselt number increases as Reynolds number increases. Increasing Reynolds number tends to suppress flow separation on the suction surface. For the low Reynolds number case (Re = 31,400 and 15,700), a small drop in Nusselt number is observed at x/C ≅ 0.17 due to the flow separation, while Nusselt number decreases monotonically with increasing streamwise distance for (Re = 52,000 and 105,000). Increasing Reynolds number also promotes boundary layer transition on the suction surface: in the case of high Reynolds number (Re = 105,000), the Nusselt number increases sharply at x/C ≅ 1.0 due to laminar-to-turbulence transition. On the pressure surface, the Nusselt number decreases sharply with increasing streamwise distance from the leading edge due to laminar boundary layer growth, with lower velocity, with further decrease near x/C ≅ -0.25 due to a strong flow separation in that region. However, it gradually increases from x/C <-0.25 as the flow reattaches and

accelerates to impede the laminar boundary layer growth. The Nusselt number on the pressure surface increases as Reynolds number increases.

Figure 18(b) through 18(e) respectively present the effect of Reynolds number on the surface distribution of the local Nusselt number for the fine grid case at position #2 (60 cm upstream), the fine grid case at position #1 (21 cm upstream), the coarse grid case at position #2 (60 cm upstream), and the coarse grid case at position #1 (21 cm upstream). For all the four grid (turbulence) arrangements, the local Nusselt number at a given location increases with increasing Reynolds number.

For low Reynolds numbers (Re = 31,400 and 15,700), a small drop in Nusselt number due to the flow separation is observed near the suction leading edge for the low *Tu* cases shown in Figures 18(c) through 18(e), indicating that low Reynolds number and low turbulence intensity enhance flow separation near the leading edge. For the high Reynolds number cases (Re = 52,000 and 105,000), and in all the four grid arrangements, Nusselt number increases sharply downstream on the suction surface due to boundary layer transition. In addition, as shown in Figure 18(e), boundary layer transition occurs at $x/C \cong 0.5$ for Re = 105,000, at $x/C \cong 0.8$ for Re = 52,000. No transition was observed for Re = 15,700. These observations suggest that high Reynolds numbers promote boundary layer transition. On the pressure surface, for the low Reynolds numbers ($15{,}700 \leq Re \leq 52{,}000$), Nusselt number decreases sharply due to lower velocity and a strong flow separation upstream at the leading edge, but starts to gradually increase as the flow reattaches and accelerates. Flow separation on the upstream pressure surface is

greatly diminished for the cases with higher Reynolds number (Re = 105,000) and higher *Tu* (> 5%).

*Effect of Turbulence Intensity***:** Figures 19(a) through 19(d) show the effects of free stream turbulence intensity on blade heat transfer for Re = 105,000, 52,000, 31,400, and 15,700. Overall, at a given Reynolds number, the local Nusselt number increases with increasing turbulence intensity on both the suction and pressure surface.

On the suction surface, an increase in turbulence intensity results in higher heat transfer coefficients. Three explanations can be advanced. Firstly, increasing turbulence intensity promotes earlier boundary layer transition and causes broader boundary layer transition region. For example, for Re = 105,000, boundary layer transition starts at $x/C \cong 1$ when Tu=0.71%, but it starts at $x/C \cong 0.5$ when Tu=15.31% (Figure 19(a)). Secondly, an increase in turbulence intensity retards flow separation (low Nusselt number) near the leading edge for low Reynolds number cases (Re = 31,400 and 15,700) shown in Figures 19(c) and 19(d). Thirdly, increasing turbulence intensity disturbs laminar boundary layer regions and thus enhances their heat transfer coefficients.

On the pressure surface, results clearly show that, for Re = 52,000 and 105,000, high turbulence intensity impedes flow separation near the leading edge and thus eliminates the separation (low Nusselt number) zone in the upstream portion of the pressure surface. The effect of turbulence intensity on flow separation is somewhat reduced for low Re cases such as Re = 31,400 and 15,700. In general, pressure surface heat transfer coefficients increase with the increase in freestream turbulence intensity for all Reynolds numbers studied.

*Effects of Unsteady Wake***:** Figure 20 (a) shows the effect of Strouhal number on the blade heat transfer at Re=105,000. The positive abscissa (x/C) indicates the streamwise distance along suction surface and the negative indicates pressure surface. Overall, at a given Reynolds number, the local Nusselt number increases with increasing Strouhal number on both suction surface and pressure surface. On the suction surface, the Nusselt number decreases monotonically with increasing streamwise distance due to laminar boundary layer growth and increases at $x/C \cong 1.0$ due to laminar to turbulent boundary layer transition. At a given location, the Nusselt number increases as Strouhal number increases. Increasing Strouhal number also promotes boundary layer transition in the suction surface: in the case of a high Strouhal number (S = 0.44), the local Nusselt number increases rapidly at $x/C \cong 0.8$ indicting laminar to turbulence transition.

On the pressure surface, the Nusselt number decreases sharply with increasing streamwise distance from the leading edge due to laminar boundary layer growth, with lower velocity, with further decrease near $x/C \cong -0.25$ due to a strong flow separation in that region. However, it gradually increases after $x/C \cong -0.25$ as the flow reattaches and accelerates to impede the laminar boundary layer growth. At the given location, results show clearly that increasing Strouhal number increases the heat transfer coefficient due to impeding flow separation and decreasing the separation (low Nusselt number) zone in the upstream portion of the pressure surface. Compared with the suction surface, Strouhal number effect, combined with increasing turbulence intensity and changing the attack angle, is reduced near the leading edge. It might be the Strouhal number effect, especially the effect of changing attack angle, is more dominate on the suction surface

than on the pressure surface. For example, in the case of figure 20(d) for S=0 and 2.96, Nusselt number enhancement is about 64% on the suction surface but Nusselt number increases about 15% on the pressure surface at given location ($x/C \cong 0.1$).

Figures from 20(b) through 20(d) respectively show the effect of Strouhal number on blade heat transfer at the three different Reynolds numbers (Re=52,000, 31,400, and 15,700). The same trend is presented from figure 20(b) through 20(d) as figure 20(a). General trends of wake effect are shown as an increase in Strouhal number results in higher heat transfer coefficients on the both suction and pressure surface, because: (1) Increasing Strouhal number, which means an increase in turbulence intensity, promotes earlier boundary layer transition and creates a broader boundary layer transition region on the suction surface: for example, for Re = 105,000, boundary layer transition starts at $x/C \cong 1$ when S=0, while it starts at $x/C \cong 0.8$ when S=0.44, such as shown in Figure 20(a); (2) An increase in Strouhal number also helps eliminate the flow separation zone, which decreases the local Nusselt number, near the leading edge for low Reynolds number cases on both the pressure and suction surfaces such as Re = 31,400 and 15,700 shown in Figures 20(c) and 20(d); (3) An increase in Strouhal number disturbs the laminar boundary layer region. On the suction surface, increasing Strouhal number suppresses laminar boundary layer growth near the leading edge ($x/C < 0.2$) due to changing the attack angle and disturbs laminar boundary layer regions due to unsteady effect; therefore, it enhances their heat transfer coefficients. On the pressure surface, increasing Strouhal number increases heat transfer coefficient on the leading

edge ($x/C < 0.2$), but the enhancement is small compared with suction surface, because the attack angle effect is negligible.

*Combined Effect of Reynolds Number and Strouhal Number***:** Figure 21(a) presents the effect of Reynolds number on local Nusselt number distribution. On the suction surface, the Nusselt number decreases monotonically with increasing streamwise distance due to laminar boundary layer growth. At a given location, the Nusselt number increases as Reynolds number increases. Increasing Reynolds number tends to suppress flow separation on the suction surface: in the cases of low Reynolds number of 31,400 and 15,700, a small drop in Nusselt number is observed at $x/C \cong 0.17$ due to the flow separation, while the Nusselt number decreases monotonically with increasing streamwise distance for cases of Reynolds number of 52,000 and 105,000. Increasing Reynolds number also promotes boundary layer transition on the suction surface: in the case of high Reynolds number of 105,000, the Nusselt number increases sharply at $x/C \cong 1.0$ due to laminar-to-turbulent boundary layer transition. On the pressure surface, the Nusselt number decreases sharply with increasing streamwise distance from the leading edge due to laminar boundary layer growth with lower velocity and drops further near $x/C \cong -0.25$ due to a strong flow separation in that region. But it starts to gradually increase from $x/C < -0.25$ as the flow reattaches and accelerates to impede the laminar boundary layer growth. The Nusselt number on the pressure surface increases as Reynolds number increases.

Figure 21(b), 21(c), and 21(d) present the combined effect of Reynolds number and Strouhal number on the local Nusselt number distributions for the three different

rotating rod speeds (50, 100, and 150 RPM). In the previous figures, such as figure 21(a) and figure 20, the Nusselt number increases as Reynolds number and Strouhal number increase. For all the three rotating arrangements, the local Nusselt number at a given location increases with increasing Reynolds number: indicating the Reynolds effect on the local Nusselt number distribution is more dominate than Strouhal number effect at a given rotating condition. For example, compared with Re = 31,400 and 15,700 at figure 21(d), the Nusselt number increases with increasing Reynolds number even though the Strouhal number decreases. However, enhancement of combined effect is small compared with enhancement of the Reynolds number in figure 21(a).

Pressure Coefficient and Heat Transfer Coefficient in the Internal Cooling Passage

The effect of Reynolds number on the overall pressure coefficient for four different model, such as (1) staggered exit, (2) inline exit for design 1 and (3) straight entrance, (4) tapered entrance for design 2 are shown in Figure 22. The static pressure was measured by micro – manometer in 5 locations at each chamber (Figure 13). The pressure coefficient increases with decreasing Reynolds number at given chamber and enhances more at inlet chamber than other chamber. After blockage, pressure coefficient enhancement decrease since blockage (jet impingement) generates tremendous pressure drop. Figure 23 shows the different model effect of pressure coefficient for four different Reynolds number (5,000, 10,000, 20,000 and 30,000). At given design, exit slot alignment or entrance geometry does not effect on pressure drop since the loss by blockage itself is relatively huge. However, design 2 creates much

pressure drop. Blockage hole diameter to blockage height for design 1 is about 3 times larger than for design 2. Generally, small diameter to height ratio generates strong jet causing heat transfer and pressure loss at given flow condition. For example, pressure drop from inlet to second chamber in design 2 straight entrance case is about 2.3 times larger than in design 1 staggered exit case for Re=30000.

Figure 24 and 25 present overall pressure coefficient with turbulent flow condition in inlet chamber by ribs. In figure 24, pressure coefficient increases with decreasing Reynolds number and those enhancements decrease after blockage. Generally, ribs increase not only heat transfer and pressure drop but also change flow direction. Flow attach between the ribs and then follows the rib orientation. Ribs are placed in space (P/e = 7.52), 45° tilted to increase heat transfer and make uniform flow in spanwise direction for design 1. However, ribs in design 2 are 135° tilted and placed in space (P/e = 7.8) to increase heat transfer and help the mainstream flow turn to first chamber, which creates unsymmetrical flow distribution in spanwiase direction causing enhanced pressure loss. At given flow condition in the figure 25, the existence of the rib does not increase much pressure drop in design 1 due to rib orientation but it significantly increase in design 2.

The local heat transfer coefficient distributions in the Fig. 26 and 27 are presented for staggered exit slot and inline exit slot for 4 different Reynolds number, based on hydraulic diameter of exit slot and averaged mainstream temperature measured at 5 position at each chamber shown in earlier Fig. 23, (Re = 5,000, 10,000, 20,000 and 30,000), respectively. The temperature difference in spanwise direction at given

chamber is less than 2.2°C in the inlet chamber, 1.7°C in the first and second chamber. Arrows indicate mainstream flow direction and impingement jet location in the blockage. The local heat transfer coefficient increases with increasing Reynolds number. For a given Re heat transfer coefficient decreases along the spanwise direction in the inlet chamber. In the Fig.26, the end of spanwise direction in the inlet chamber was blocked, which cause disturbance of the flow progress by increased pressure and make unsymmetrical flow ejection to the first chamber by the jet impingement. The blockage distributes unsymmetrical mainstream flow from inlet chamber uniform compare to asymmetry of the inlet chamber. Detail discussion along the streamwise direction will be mentioned in the spanwise averaged results. The local heat transfer distribution for the inline exit slot, shown in Fig. 27, is similar results with one for the staggered exit slot. The slot alignment may not affect on the upstream chamber heat transfer distribution. In design 2, shown in Fig. 28 and 29, there are no differences in local heat transfer distribution with straight entrance and tapered entrance since blocked end at spanwise direction in inlet chamber.

The streamwise heat transfer distributions, based on spanwise average, are shown in figure 30 for four different configurations, such as a) staggered exit in design 1, b) inline exit in design 1, c) straight entrance in design 2 and d) tapered entrance in design 2. The averaged heat transfer coefficient is presented as a function of the normalized distance (x/D_h) from inlet chamber. In the staggered exit in design 1 case, the local heat transfer decrease as increase the normalized distance (x/D_h) in inlet chamber. In the first chamber, local heat transfer coefficient is low after upstream of blockage instantly due to

slow moving of recirculation in high Reynolds number case (Re $\geq$ 20,000, corresponding blowing ratio M >1). Then, it increases until very high spots along the downstream due to attachment of mainstream flow. After high spot, a heat transfer coefficient decrease along down stream and increases again near the second blockage since air flow from first blockage (jet impingement) faces second blockage with staggered holes and deflected toward to top and bottom channel wall causing very high local heat transfer or flow reattachment near the blockage. Local heat transfer near the second blockage is about 10% higher than at flow attachment region. However no flow attachment appear in low Reynolds number flow (Re < 10,000). In the second chamber, total heat transfer distribution shows similar trend in the first chamber. There are no significant differences in the heat transfer distribution between the inline/staggered exit slot for design 1 except the level of heat transfer. In the design 2, two different entrance configurations, (c) straight entrance and (d) tapered entrance, show similar results since the end of radial direction in the inlet chamber is blocked causing similar effect with tapered entrance. Local heat transfer is low after first chamber and then it increase with increasing normalized distance and no flow attachments appears since small ratio of the hole diameter to blockage height creates strong jet. Strong jet faces second blockage directly and deflects toward near the holes of wall. However, in second chamber, local heat transfer increase as increase distance before slot/land region and significantly increase at entrance of slot/land since cross section .area is decreased. Decreasing Reynolds number reduces heat transfer entire area and disturbs the flow attachment in the first chamber. However, attachment locations are not move. Figure 31 shows the

overall heat transfer coefficient for four different models. Design 1 creates higher heat transfer on the wall than Design 2, since flow attachment as shown on the wall of the first and second chamber for Design 1. At the given design, inlet exit in the Design 1 and straight entrance in Design 2 generate more heat transfer.

The local heat transfer distribution in high turbulent intensity flow by ribs in the inlet chamber are shown in figure 32 for design 1 and figure 33 for design 2. In the design 1, ribs are placed to agitate flow turning causing more uniform distribution compare to straight entrance case (figure 26) and to increase turbulence intensity. At given Re, the local heat transfer between the ribs is higher than on the ribs for design 1. Heat transfer on the rib, made by copper, is calculated based on averaged temperature, including front, back and top of the rib. Generally, heat transfer coefficient on the wall is lower than top of the rib surface if rib space is large enough flow to reattach on the wall ($P/e > 10$). However, averaged heat transfer coefficient on the rib may be low since two low regions, such as front and back surface of the rib due to flow circulation, are included also. In the first chamber, flow attachment is shown and more symmetric in spanwise direction due to rib in the inlet chamber. In the design 2, ribs are placed to help to turning the air to first chamber causing asymmetry in spanwise direction and increase turbulence intensity. Figure 34 and 35 presents spanwise averaged and overall heat transfer coefficient respectively. At the inlet chamber, ribs enhanced more heat transfer in Design 1, but decrease in Design 2 due to different rib orientation. As mentioned earlier, ribs increase heat transfer and change flow direction. Local mainstream flow velocity decreases along spanwaise direction in the smooth entrance

case. Ribs in the Design 1 distribute the flow turning to the first chamber, and make velocity distribution more uniformly causing heat transfer enhancement. However, ribs in Design 2 make more unsymmetrical velocity distribution causing decreased averaged – heat transfer.

Heat Transfer Coefficient and Film Effectiveness on the External Cooling Model

Figure 36 show Stanton show the Stanton Number distribution in the straight entrance with staggered / inline exit slot for the design 1 and in the straight / tapered entrance with staggered exit slot for the design 2, respectively. Heat transfer coefficient is calculated free stream temperature which based on the land and the coolant temperature, which came from compressed air, on the slot region. Those temperature differences are about up to 2 C. The main difference configuration in two designs is the land slop. Land slop in design 1 is parallel to free stream direction but it is about 8° tilted. In the figure, white region, near the slot exit at M=0 case, indicates no data due to time limits for valid of I-D assumption on the transient liquid crystal technique. Generally, Stanton Number, defined as ($St = \frac{h}{\rho C_p V}$), increases with increasing Reynolds Number on the slot except M=0 case. Since, in the low M case (M<1), the coolant flow (mainstream flow in the internal test) is dominant on the slot and the free stream flow is dominant on the land as well. However, in the high M case (M>1), the coolant also effects on the land. In the M=0 case, near the exit region, Stanton Number is close to 0 and Stanton Number increases after certain region where the free stream

flow attaches on the slot. However, small amount of coolant flow (0<M<1) disturbs the flow attachment causing low heat transfer. Stanton Number is decreasing from the exit along the mainstream – wise (coolant) direction on the slot and it does not much change on the land at given blowing ratio (M) case. Figure 37 show Stanton Number ratio distribution where St_0 is the local Stanton Number for M=0 case. Generally, Stanton Number ration increases as M increases both on the slots and the lands. For the low M case (0<M<1), Stanton Number ratio decreases with increasing distance from the coolant exit in the slot and near the downstream region even it lower than 1, which indicates lower heat transfer coefficient than M=0 case, due to disturb flow attachment. Span - wise / overall averaged Stanton number distribution presented in figure 38 and 39. Averaged Stanton number presented in function of x/Ms, where s is height of exit slot. Increasing blowing ratio (M) increases Stanton Number on the land for M>1 case but M does not much effect in the low M case (M<1). For low M case, it may not enough amount of the coolant air to mix with free stream air on the land. However, for the high M case, large amounts of the air and momentum energy of coolant air may interact with free stream not only on the slot but also on the land. At high blowing ratio (M>1), Stanton number decreases with increasing distance due to boundary layer growth on the slot for design 1. However Stanton number decreases, until it reaches low point, and then it increases again since existence of mixture for design 2. Tapered entrance model shows similar trend with straight entrance case (c) since straight or tapered effect in the inlet chamber might be vanished after 2series of the blockage (jet impingement). In the overall Stanton number distribution (Figure 39), results show Stanton number for design

2 is lower than for design 1 and there is no effect of staggered / inline exit for design 1 and straight / tapered entrance for design 2 on the land. On the slot, result for staggered exit presents higher than for inline exit for design 1 since staggered exit increase turbulence intensity after second chamber causing high heat transfer on exit region.

Figure 40 and 41show Stanton number and Stanton number ratio distribution with rib entrance and turbulence grid. In figure 40, there are similar trends with straight entrance case in low blowing ratio (M<1), since coolant mixture with free stream and high turbulence coolant flow by jet impingement (blockage) enhance hear transfer already. Increased free stream turbulence enhances more local Stanton Number shown in Figure 40 (a). Span-wise average Stanton number is presented in Figure 42 and comparison with straight entrance (smooth entrance) is shown in Figure 43. The results show that both increased coolant turbulence intensity by ribs and increased free stream turbulence intensity by turbulent grid enhance heat transfer.

Film cooling effective distribution (Figure 44) and span-wise averaged effectiveness (Figure 45) are presented for four different blowing ratio (M) , such as 0.3, 0.6, 1.22 and 1.83. All model show pretty symmetric distribution in span-wise direction. Span-wise average is conducted in center 5 lands and 5 slots. Increasing blowing ratio decreases film effectiveness on the land and does not effect on the slot in figure 44 since the higher momentum of jet tend to lift off at the land. Generally, film effectiveness on the land increases along the downstream by interacting with coolant air and decreases on the slot by mixing with free stream flow. However, results show that averaged film effectiveness decreases as increase normalized distance (x/Ms) until it reach minimum

and then increase due to mix with hot coolant air on the land. After it reaches to maximum, it decreases again. The other hand, it is close to 1 on entire on the slot indicating perfectly covered by coolant air except m=1.83, with straight entrance for design 2 case. Interesting phenomenon is that actual maximum location is fixed for different blowing ratio condition. At given location and blowing ratio, film effectiveness for design 1 is significantly lower than design 2 since zero slope of land for design 1 obstructs the existence of mixture on the land.

Figure 46 show the film cooling effectiveness with relatively high turbulent flow, such as (a) high turbulent coolant flow by rib entrance and (b) high turbulent coolant flow by rib entrance and high turbulent free stream flow by turbulence grid. Film effectiveness on the slot does not much decrease by increased turbulence flow near the front region since it already perfectly covered by coolant air. However turbulent flow of the both free-stream and mainstream flow make strong mixture causing increased film effectiveness on the land.

Figure 47 shows the spanwise averaged film effectiveness. On the land, film effectiveness is lower with higher blowing ratio (M) near the exit, but film effectiveness is increased along the downstream. In the high blowing ratio, the coolant might be not protect the land surface and interacts with freestream flow directly. On the slot, surface is almost perfectly covered by coolant wilt all blowing ratio case. In the figure 48, smooth entrance case shows better protection because high turbulent coolant interacts with freestream flow rapidly.

CONCLUSIONS

Blade Heat Transfer and Pressure Coefficient

The influence of free stream turbulence, unsteady wake and inlet Reynolds number ($15{,}700 \leq Re \leq 105{,}000$) on turbine blade surface pressure coefficient and heat transfer has been investigated in a low speed wind tunnel. Two different grids were used to generate different turbulence intensity levels and three different rotating conditions were applied to generate different Strouhal numbers. The main conclusions are:

1. In general, local pressure coefficients on both the suction and pressure surfaces increase with decreasing Reynolds number. The effect of Reynolds number on local pressure coefficient becomes negligible when Reynolds number is reduced to 30,000. Also, local pressure coefficients increase on the suction surface and decrease on the pressure surface as the turbulence intensity increases.
2. At a given location, local pressure coefficients on the both surfaces increase as Strouhal number increases, but near the leading edge ($x/C < 0.2$) on the suction surface decrease due to deflection of the attack angle.
3. Flow separation in the leading edge region of the blade is enhanced by decreasing Reynolds number but suppressed as the turbulence intensity increases.
4. Local Nusselt number increases with increasing Reynolds number, increasing turbulence intensity and increasing Strouhal number. Also, the local Nusselt

number in the separation region near the leading edge decreases with decreasing Reynolds number, but increases as the turbulence intensity increases.

5. Increasing Reynolds number, turbulence intensity and Strouhal number tend to promote boundary layer transition and enhance local heat transfer coefficient.
6. Flow separation in the leading edge region is enhanced as Reynolds number decreases but is suppressed as Strouhal number increases.
7. The local Nusselt number in flow separation region near the leading edge decreases as Reynolds number decreases, but is suppressed by wake (Strouhal number) effect.

Trailing Edge Heat Transfer and Film Effectiveness

The influence of Blowing ratio ($0.3 \leq M \leq 1.83$), blockage and several different model on trailing edge surface pressure, heat transfer and film effectiveness has been investigated in a low speed wind tunnel. Seven different models were used in experiment, such as (1) staggerd / (2) inline exit alignment slot and (3) rib entrance for design 1 and (4) straight / (5) tapered / (6) rib entrance and (7) turbulence grid for design 2. The main conclusions are;

1. Generally, increasing Reynolds number decreases pressure coefficient and increases heat transfer for internal cooling.
2. Jet impingement by blockage enhance heat transfer on the internal wall and blockage but increases pressure loss significantly Also taper

entrance and inline exit effects are insignificant to compare with blockage.

3. Rib entrance in design 1 enhances heat transfer in inlet chamber but rib entrance in design2 enhances heat transfer in first chamber significantly.
4. Increasing Blowing ratio enhances heat transfer and decrease film effectiveness for external cooling test.
5. Land slope enhance film effectiveness on the land and small amount of coolant air (M<1) decreases heat transfer on the slot Also taper entrance and inline exit effects are insignificant to compare with rib entrance and turbulence grid.

REFERENCES

[1] R.B. Rivir, 1996, Transition on turbine blade and cascade at low Reynolds numbers, AIAA 96-2079, 27th AIAA Fluid Dynamics Conference, June 17-20, New Orleans, LA, 1996.

[2] R.J. Volino, L.S. Hultgren, Measurements in separated and transitional boundary layers under low-pressure turbine airfoil conditions, ASME Paper 2000-GT-0260, 2000.

[3] R.J. Volino, C.G. Murawski, Separated flow transition in a low-pressure turbine cascade – mean flow and turbulence spectra, ASME Paper 2003-GT-38727, 2003.

[4] K.W. Van Treuren, T. Simon, M.V. Koller, A.R. Byerley, J.W. Baughn, R. Rivir, Measurements in a turbine cascade flow under ultra low Reynolds number conditions, ASME 2001-GT-0164, ASME Turboexpo 2001, June 4-7, New Orleans, LA, 2001.

[5] Meinhard T.Schoberi, Burak Ozturk, David E.Ashpis, On the physics of flow separation along a low pressure turbine blade under unsteady flow condition, ASME Paper GT2003-38917, 2003.

[6] Meinhard T.Schoberi and Burak Ozturk, Experimental study of the effect of periodic unsteady wake flow on boundary layer development, separation, and Re-attachment along the surface of a low pressure turbine blade, ASEM Paper GT2004-53929, 2004.

[7] M.F. Blair, Influence of free-stream turbulence on turbulent boundary layer heat transfer and mean profile development, Part 1 – Experimental data, ASME J. Heat Transfer 105 (1983) 33-40.

[8] M.F. Blair, Influence of free-stream turbulence on turbulent boundary layer heat transfer and mean profile development, Part 2 – Analysis of results, ASME J. Heat Transfer 105 (1983) 41-47.

[9] J.C. Simonich, P. Bradshaw, Effect of free-stream turbulence on heat transfer through a turbulent boundary layer, ASME J. Heat Transfer 100 (1978) 671-677.

[10] P.E. Hancock, P. Bradshaw, Effect of free-stream turbulence on turbulent boundary layer, ASME J. Fluid Engineering 105 (1983) 284-289.

[11] J.E. O'Brien, G.J. VanFossen, The influence of jet-grid turbulence on heat transfer from stagnation region of a cylinder in cross flow, ASME Paper 85-HT-58, 1985.

[12] W.J. Bellow, R.E. Mayle, Heat transfer downstream of a leading edge separation bubble, ASME J. Turbomachinery 108 (1986) 131-136.

[13] A.B. Mehendale, J.C. Han, S. Ou, Influence of mainstream turbulence on leading edge heat transfer, ASME J. Heat Transfer 113 (1991) 843-850.

[14] A. Brown, B.W. Martin, Heat transfer to turbine blade, with special reference to the effects of mainstream turbulence, ASME Paper 79-GT-26, 1979.

[15] A. Brown, B.W. Martin, Flow transition phenomena and heat transfer over the pressure surfaces of gas turbine blades, ASME J. Engineering for Power, 104 (1982) 360-367.

[16] L. Zhang, J.C. Han, Influence of mainstream turbulence on heat transfer coefficients from a gas turbine blade, ASME J. Heat Transfer. 116 (1994) 896-903.

[17] J.C. Han, L. Zhang, S. Ou, Influence of unsteady wake on heat transfer coefficient from a gas turbine blade, ASME J. Heat Transfer 115 (1993) 904-911.

[18] F.E. Ames, The influence of large-scale high-intensity turbulence on vane heat transfer, ASME J. Turbomachinery 119 (1997) 23-30.

[19] M.G. Dunn, Heat flux measurements for the rotor of a full-stage turbine: part 1 – time averaged results, ASME J. Turbomachinery 108 (1986) 90-97.

[20] M.G. Dunn, W.K. George, W.J. Rae, S.H. Woodward, J.C. Moller, J.P. Seymour, Heat flux measurements for the rotor of a full-stage turbine: part 2 – description of analysis technique and typical time-resolved measurement, ASME J. Turbomachinery 108 (1986) 98-107.

[21] M.G. Dunn, J.P. Seymour, S.H. Woodward, W.K. George, R.E. Chupp, Phase-resolved heat flux measurements on the blade of a full-stage turbine, ASME J. Turbomachinery 111 (1989) 8-19.

[22] R.S. Abhari, G.R. Guenette, A.H. Epstein, M.B. Goled, Comparison of time-resolved measurements and numerical calculations, ASME J. Turbomachinery 114 (1992) 818-827.

[23] J.E. O'Brien, S.P. Capp, Two-component phase-averaged turbulence statistics downstream of a rotating spoked-wheel wake generator, ASME J. Turbomachinery 111 (1989) 475-482.

[24] X. Liu, W. Rodi, Measurement of unsteady flow over and heat transfer from a flat plate, ASME paper 89-GT-2, 1989.

[25] K. Dullenkopf, A. Schulz, S. Witting, The effect of incident wake on the mean heat transfer of an airfoil, ASME J. Turbomachinery 113 (1991) 412-418.

[26] R.E. Mayle, The role of laminar-turbulent transition in gas turbine engines, ASME J. Turbomachinery 113 (1991) 509-537.

[27] K.A. Alabi, Analysis of the effect of upstream turbulence on aircraft engine turbine blades, Ph. D. Dissertation, Department of Mechanical Engineering, SUNY Stony Brook, Stony Brook, New York, May 2003.

[28] J. C. Han, S. Dutta, S. V. Ekkad, Gas Turbine Heat Transfer and Cooling Technology, Tayler and Francis, New York, 2000.

[29] R.T. Kukreja, S.C. Lau, Distribution of local heat transfer coefficient on surface with solid and perporated ribs, J. Enhanced Heat Transfer 5 (1), (1998) 9-21.

[30] J.J. Hwang, T.Y. Lia, T.M. Liou, Effect of fence thickness on pressure drop and heat transfer in perforated fenced channel, Int. J. Heat Mass Transfer 41 (4-5), (1998) 811-816.

[31] T.M. Liou, S.H. Chen, Turbulent heat and fluid flow in a passage distributed by detached perforated ribs of different height, Int. J. Heat Mass Transfer 41 (12), (1998) 811-816.

[32] J.M. Buchlin, Convective heat transfer in a channel with perforated ribs, Int. J. Thermal Sci. 41 (2002)332-340.

[33] S.W. Moon, S.C. Lau, An experimental study of local heat transfer distribution between blockage with holes in a rectangular channel, ASME IMECE 2002-33673, 2002.

[34] S.C. Lau, J. Cervantes, J.C. Han, R.J. Rudolph, K.Flannery, Measurement of wall heat (mass) transfer for flow through blockage with round and square holes in a wide rectangular channel, Int. J. Heat and Mass Transfer 46 (2003) 3991-4001.

[35] R.J. Goldstein, Film cooling, Advances in Heat Transfer, Academic Press, New York and London 7 (1971) 321-379.

[36] K. Wieghardt, Hot-air discharge for de-icing, A.A.F. Translation F-TS-919-RE, 1946.

[37] S.C. Kacker, J.H. Whitelaw, The effect of slot height and slot turbulence intensity on the effectiveness of the uniform density, two dimensional wall jet, ASME J. of Heat Transfer 100 (1968) 469-475.

[38] S.C. Kacker, J.H. Whitelaw, An experimental investigation of the influence of slot-lip-thickness on the impervious-wall effectiveness of the uniform-density, two-dimensional wall jet, Int. J. Heat and Mass Transfer 12 (1969) 1201-1206.

[39] S.S. Papell, Effect on gaseous film cooling injection through angled slots and normal holes, NASA TN-D-299, 1960.

[40] R.J. Goldstein, R.B. Rask, E.R.G. Eckert, Film cooling with helium injection into an incompressible air flow, Int. J. Heat and Mass Transfer 9 (1966) 1341-1350.

[41] W.B. Nicoll, J.H. Whitelaw, The effectiveness of the uniform density, two-dimension wall jet, Int. J. Heat and Mass Transfer 10 (1967) 623-639.

[42] A.K. Rostogi, J.H. Whitelaw, The effectiveness of three-dimensional film cooling slots-I measurement, Int. J. Heat and Mass Transfer 16 (1973) 1665-1672.

[43] S.V. Patankar, A.K. Rostogi, J.H. Whitelaw, The effectiveness of three-dimensional film cooling slots-II. predictions, Int. J. Heat and Mass Transfer 16 (1973) 1679-1681.

[44] D.E. Paxson, R.E. Mayle, The influence of main stream thermal boundary layer on film cooling effectiveness, ASME Paper 88-GT-17, 1998.

[45] M.N.R. Nina, J.H. Whitelaw, The effectiveness of film cooling with three dimensional slot geometries, ASME paper 71-GT-11,1971.

[46] M.E. Taslim, Experimental investigation of film cooling effectiveness for slots of various exit geometries, AIAA J. Thermophysics and Heat Transfer 6 (2) (1992) 302 – 307.

[47] G.J. Sturgess, Design of combustor cooling slots for high film effectiveness: part 1 – film general development, ASME 85-GT-35, 1985.

[48] G.J. Sturgess, Design of combustor cooling slots for high film effectiveness: part 1 – film initial development, ASME 85-GT-36, 1985.

[49] P. Martini, A. Schulz, S. Wittig, Experimental and numerical investigation of trailing edge film cooling by circular wall jets ejected from a slot with internal rib arrays, ASME Paper GT2003-38157, 2003.

[50] J.S. Kwak, J.C. Han, Heat transfer coefficients and film cooling effectiveness on the squealer tip of a gas turbine blade, J. Turbomachinery 125 (2003) 648-657

APPENDIX

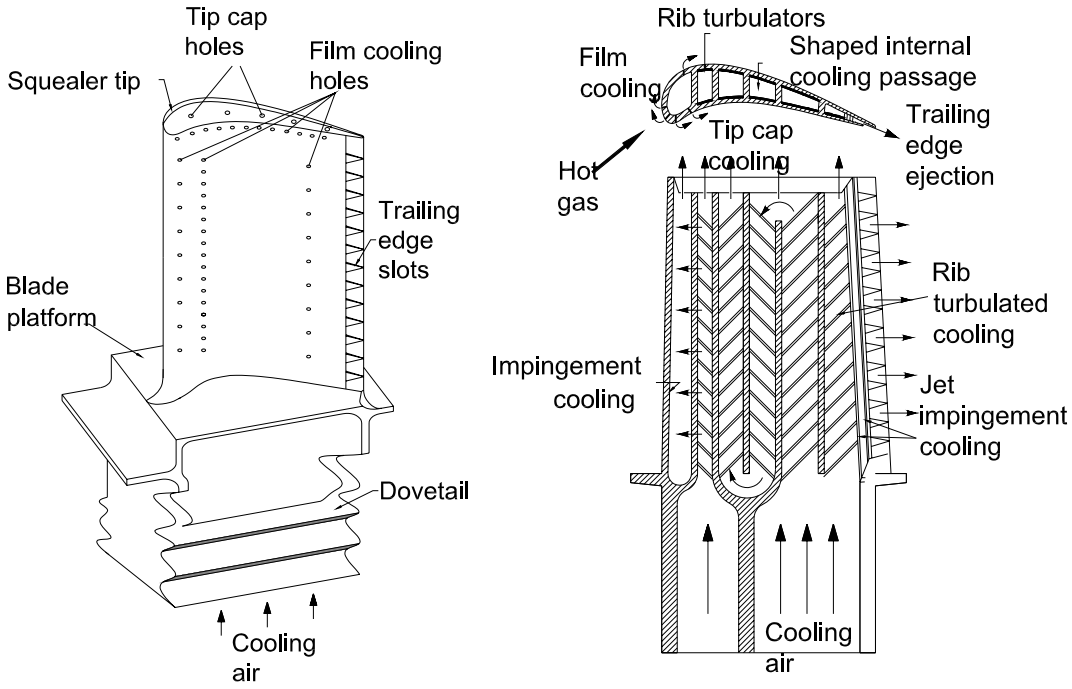

(a) External Film Cooling **(b) Internal Convective Cooling**

Fig.1 Typical Turbine Airfoil with Cooling Techniques

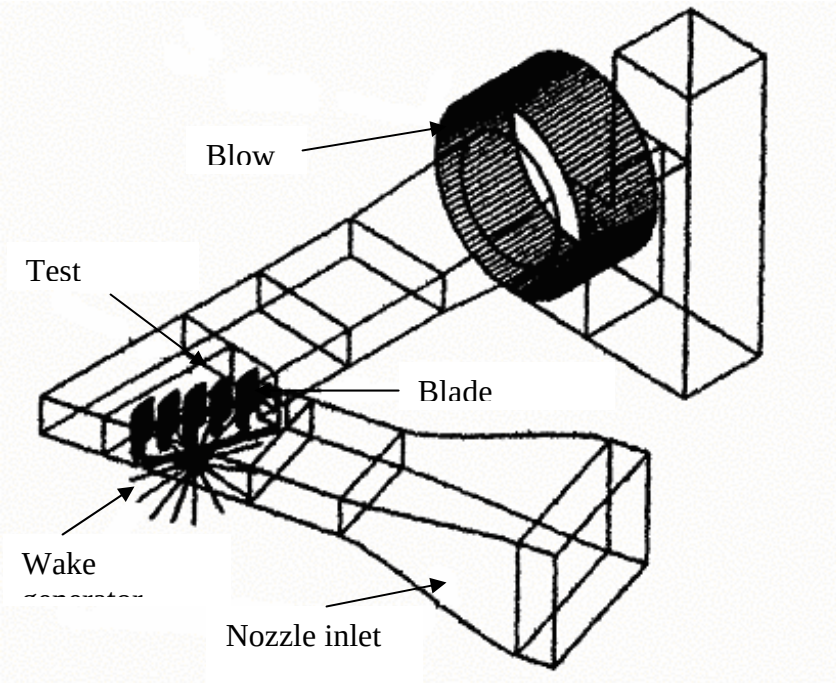

(a) Schematic of the test Section with Rotating Wake Generator

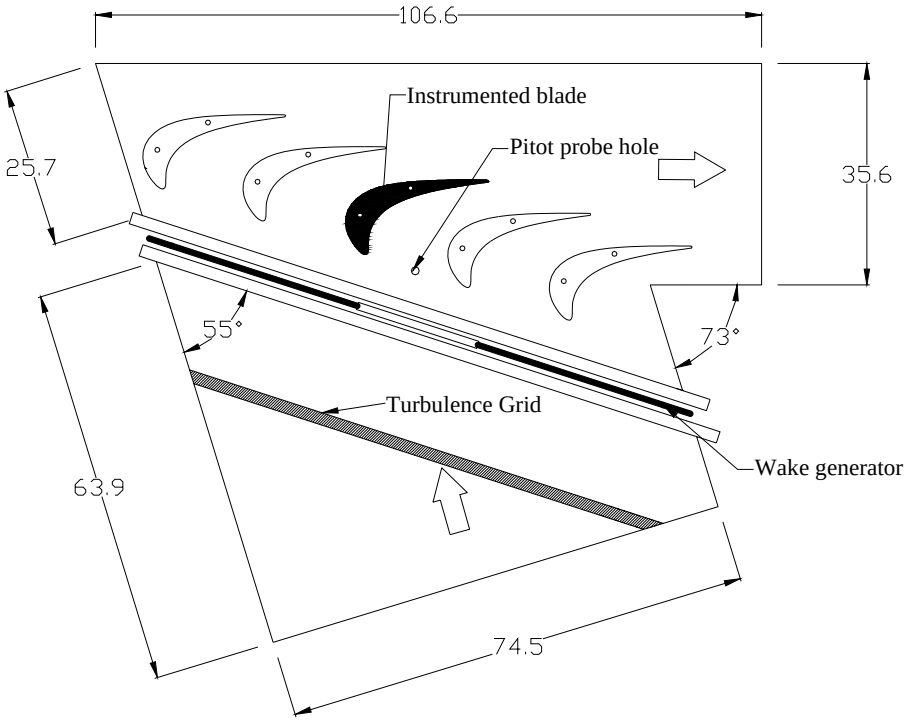

(b) Instrumentation Layout (unit : cm)

Fig. 2 Test Section and Instrumentation Layout

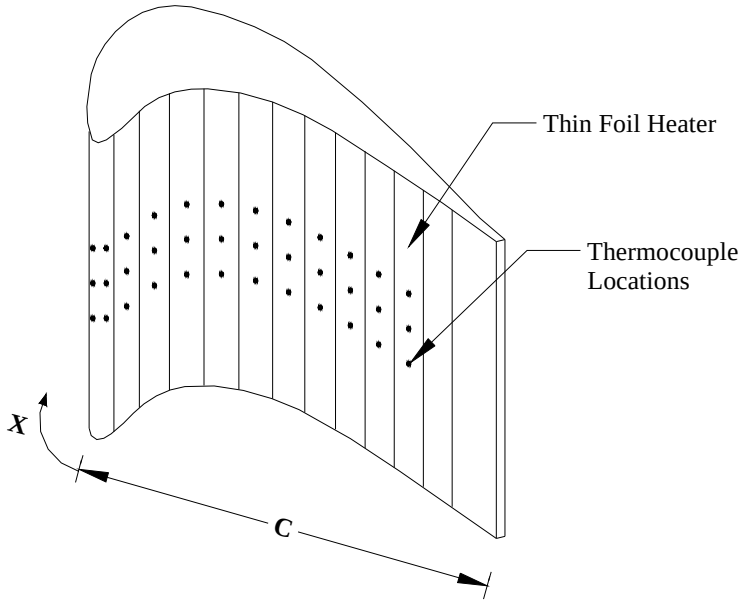

Fig.3 Heat Transfer Instrumented Blade

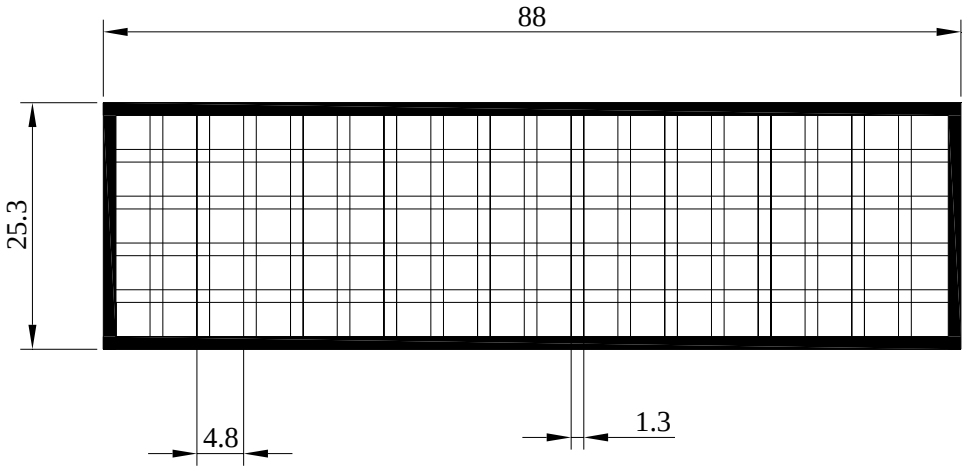

(a) Coarse Grid

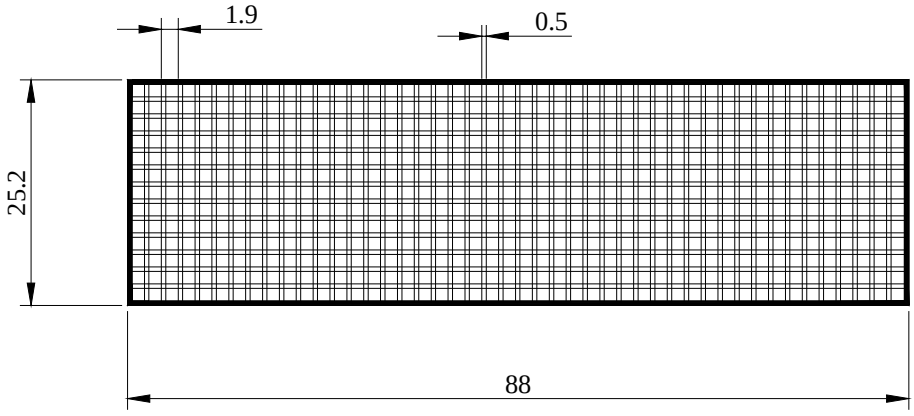

(b) Fine Grid

Fig. 4 Turbulence Grid

Grid	Location (Cm)	Tu(%)			
		Re = 105,000 V=6.94 m/s	Re = 52,000 V=3.44m/s	Re = 31,400 V=2.08 m/s	Re = 15,700 V=1.04m/s
No Grid		0.71	0.73	0.7	0.68
Grid #1	60	5.34	5.02	3.59	2.81
	21	15.31	14.33	10.07	8.65
grid #2	60	2.72	2.6	2.07	1.6
	21	6.76	5.51	4.02	3.08

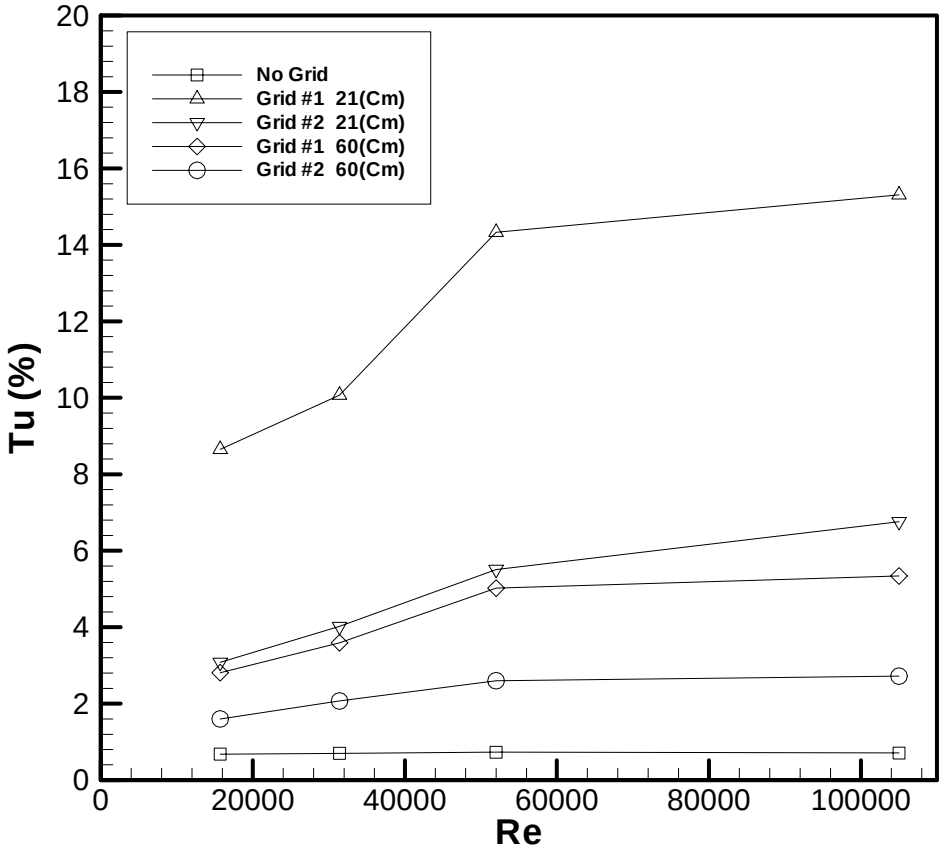

Fig. 5 Turbulence Intensity at Different Re

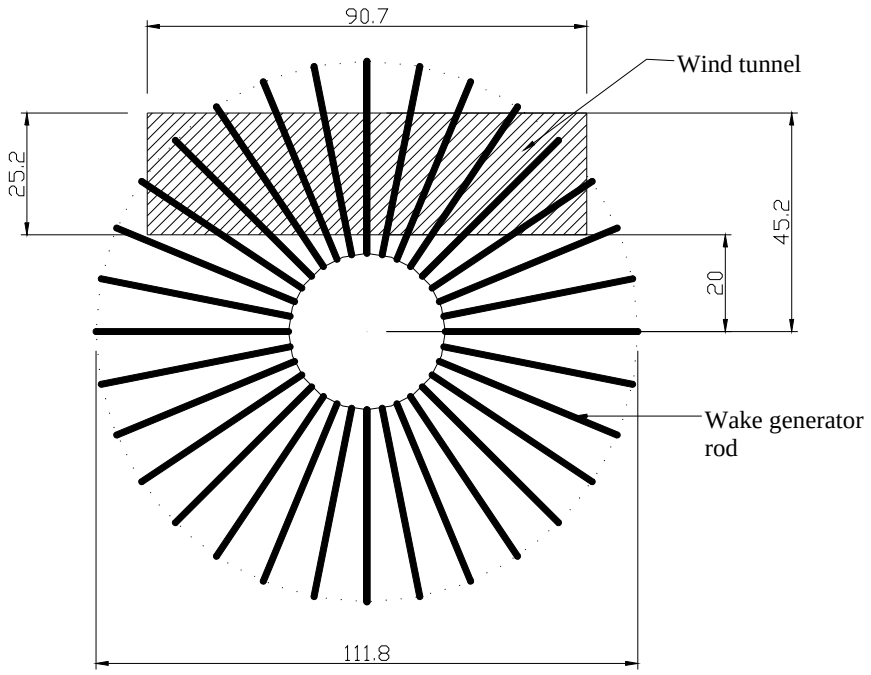

Fig. 6 Wake Flow Generator (unit : cm)

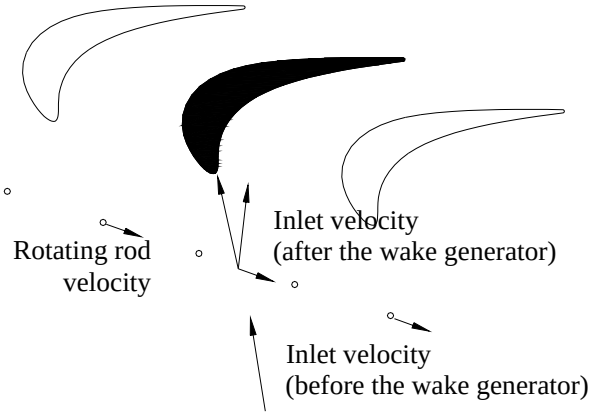

(a) Small Strouhal Number Case (S<1)

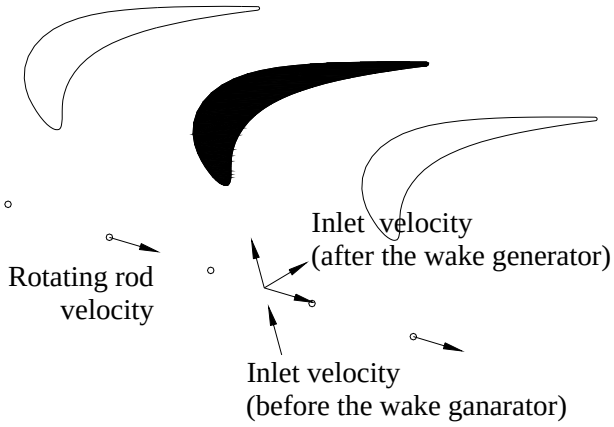

(b) Large Strouhal Number Case (S>1)

Fig. 7 Conceptual View of Effect of Unsteady Wake on Blade Model

RPM	S			
	Re=105,000	Re=52,000	Re=31,400	Re=15,700
150	0.44	0.89	1.47	2.96
100	0.29	0.59	0.98	1.97
50	0.15	0.3	0.49	0.99
No Rod	0.0	0.0	0.0	0.0

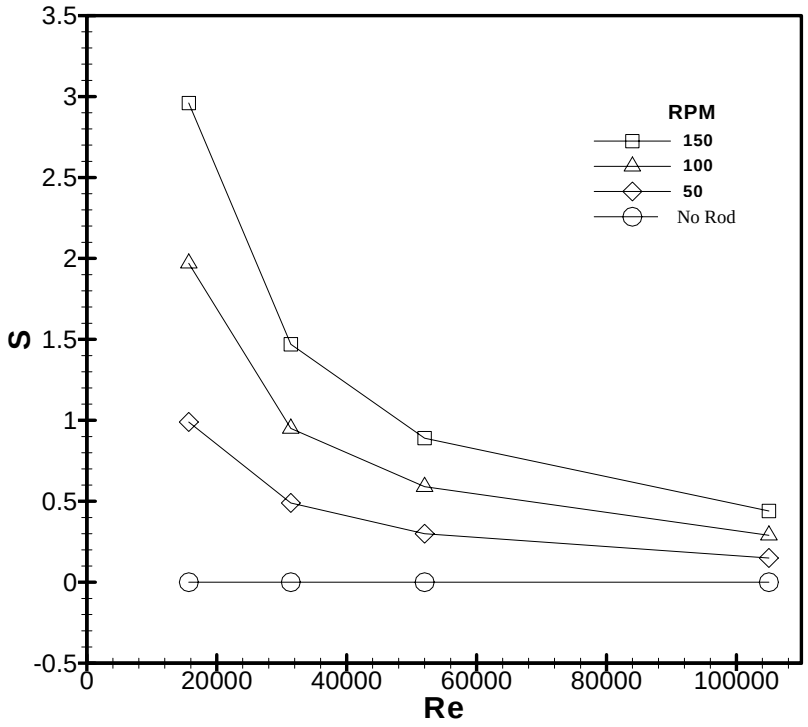

Fig. 8 Strouhal Number at Different Reynolds Number and RPM

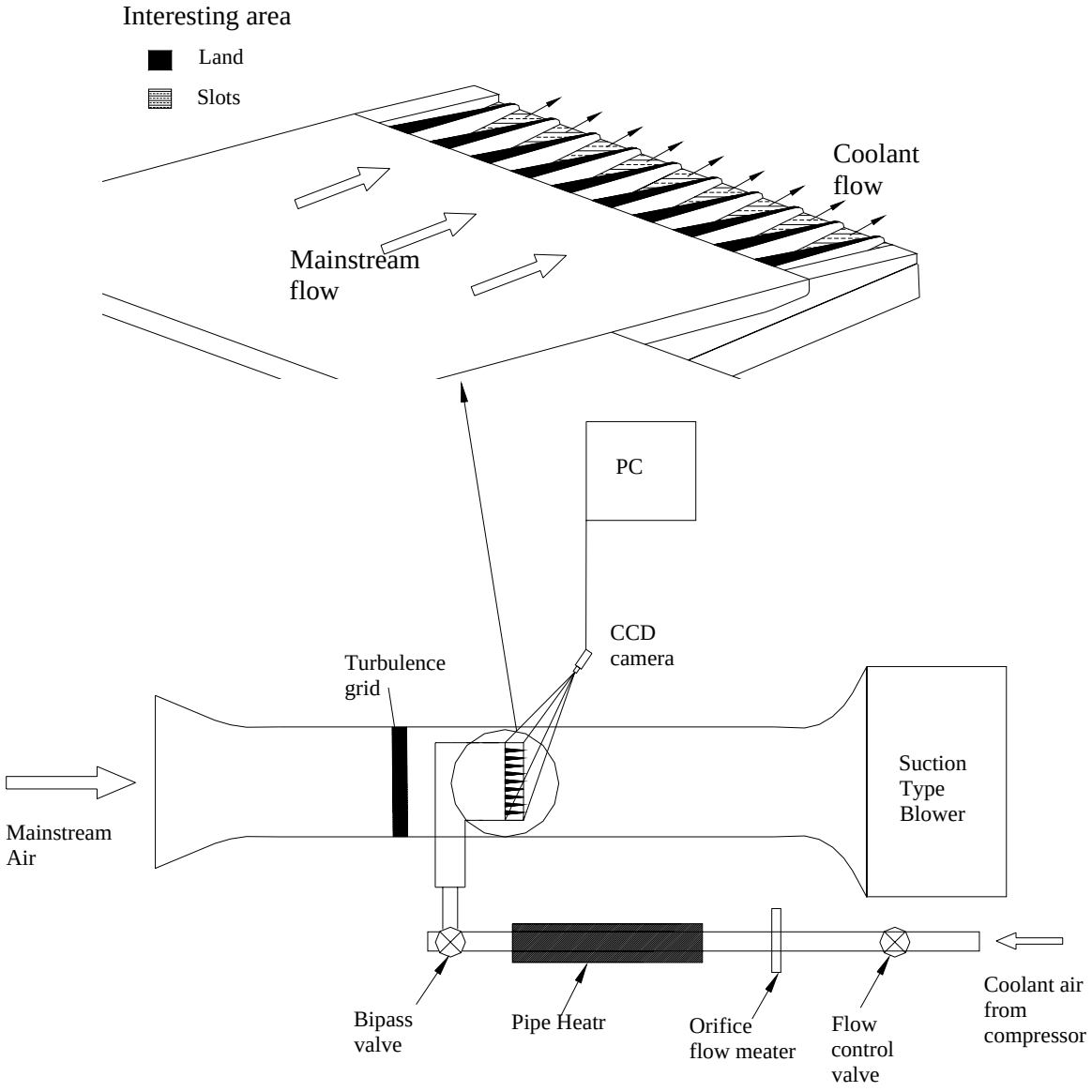

Fig. 9 Schematic of External Trailing Edge Film Cooling Model

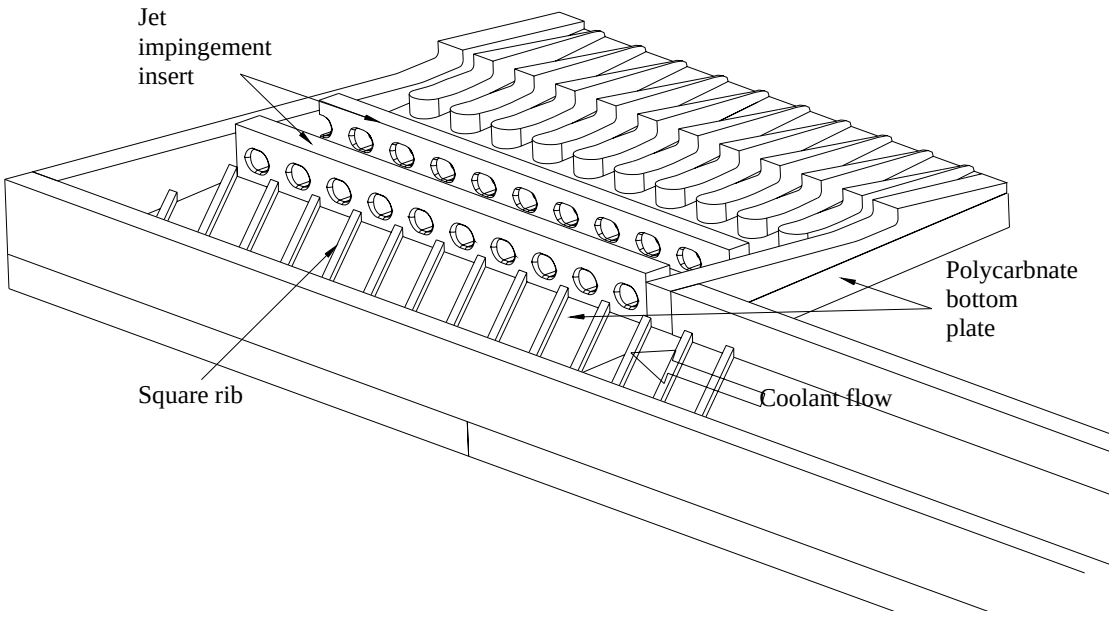

Fig. 10 Detail Drawing of Internal Cooling Model

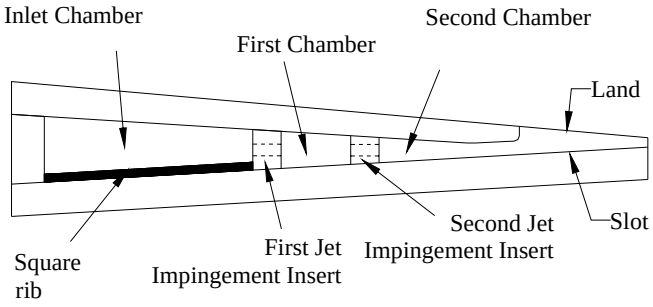

(a) Side View

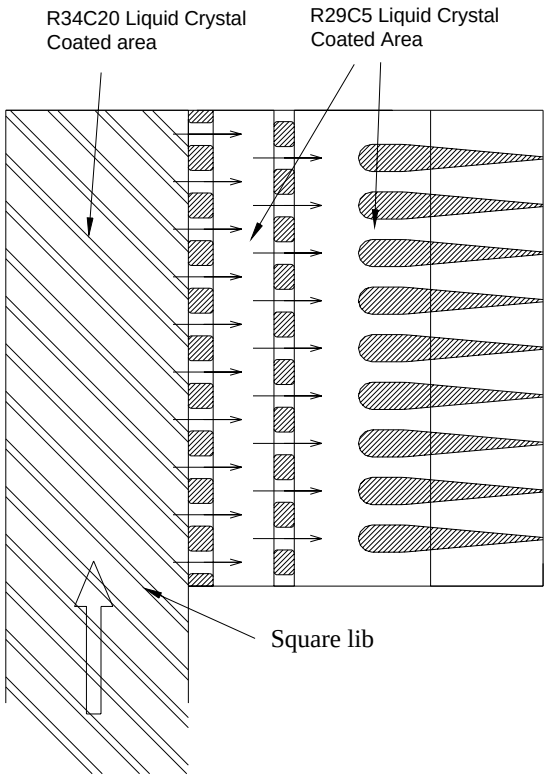

(b) Top View

Fig. 11 Schematic of Trailing Edge Internal Cooling Model (Design 1)

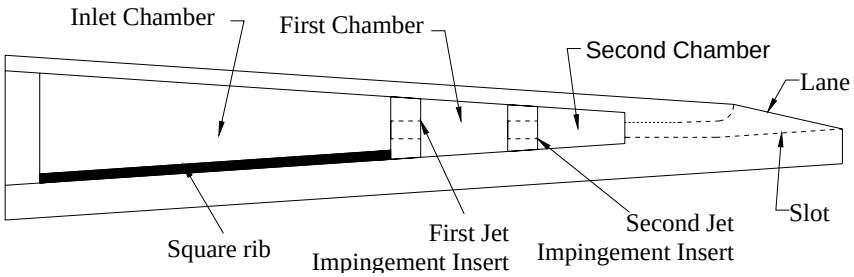

(a) Side View

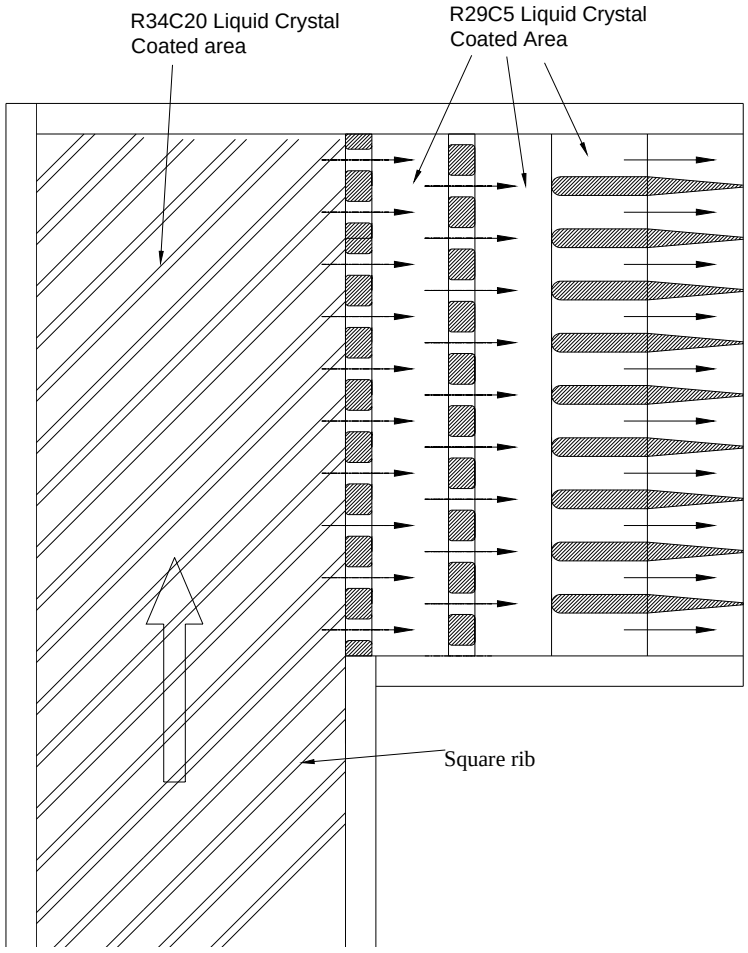

(b) Top View

Fig. 12 Schematic of Trailing Edge Internal Cooling Model (Design 2)

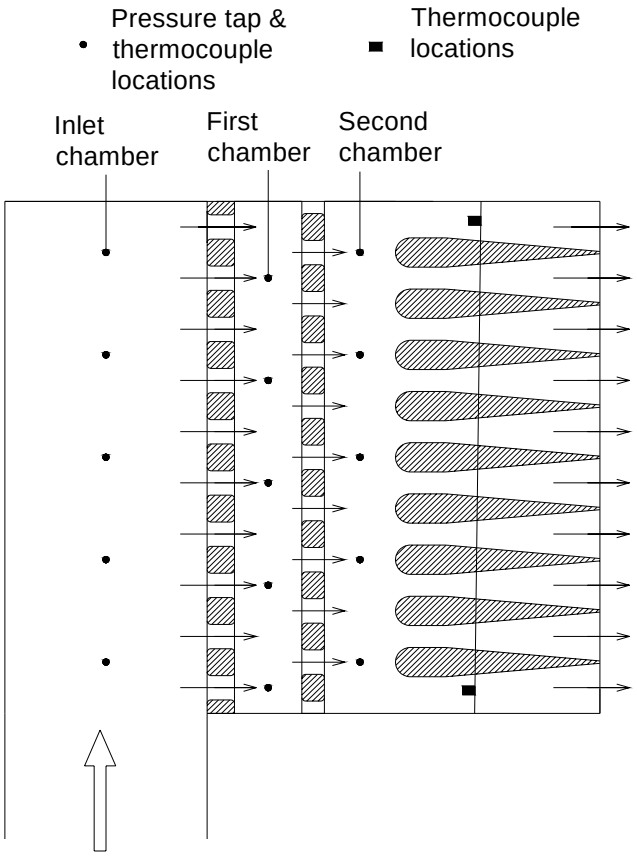

Fig. 13 Detail View of Thermocouple and Pressure Tab Location (Design 1)

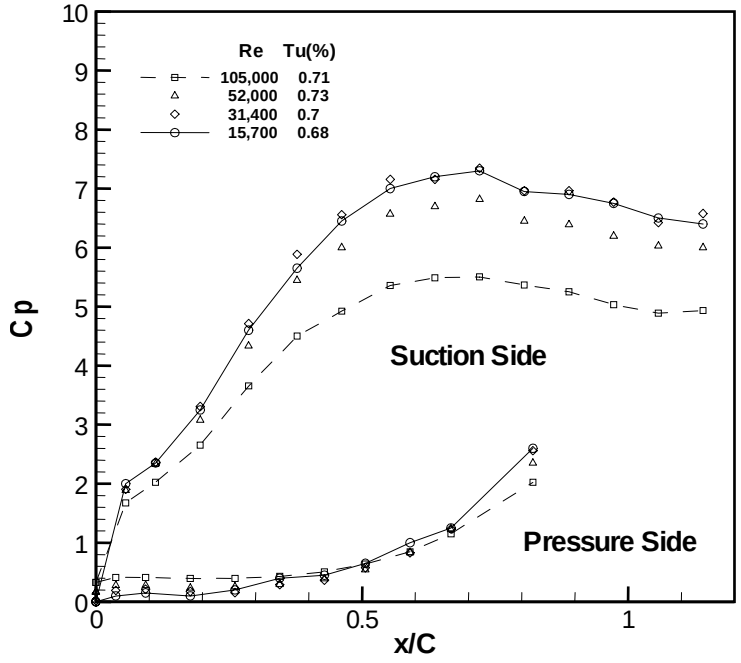

(a) The No Grid Case

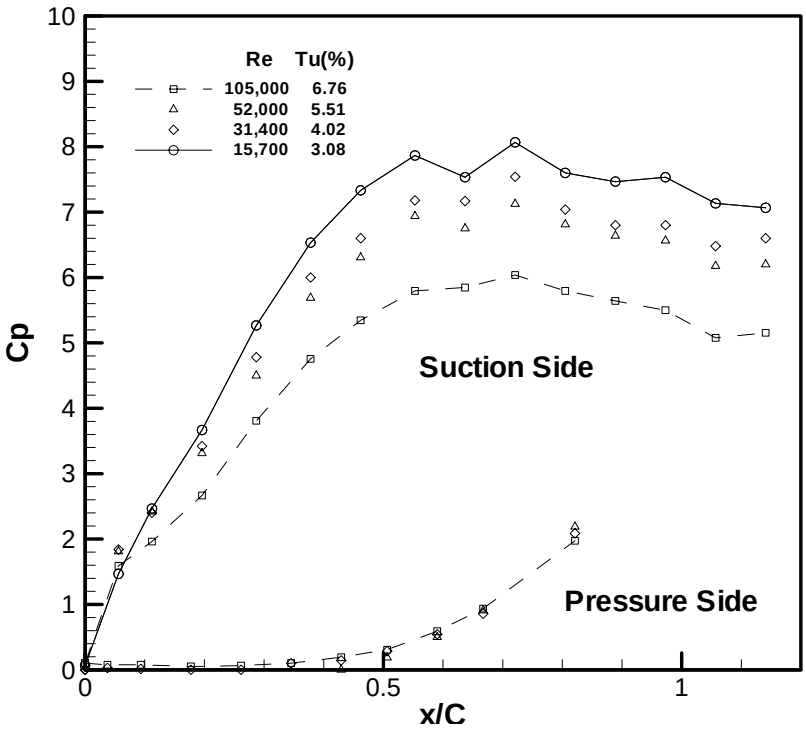

(b) The Fine Grid at Position #1

Fig. 14 Effect of Reynolds Number on Local Pressure Coefficient Distribution

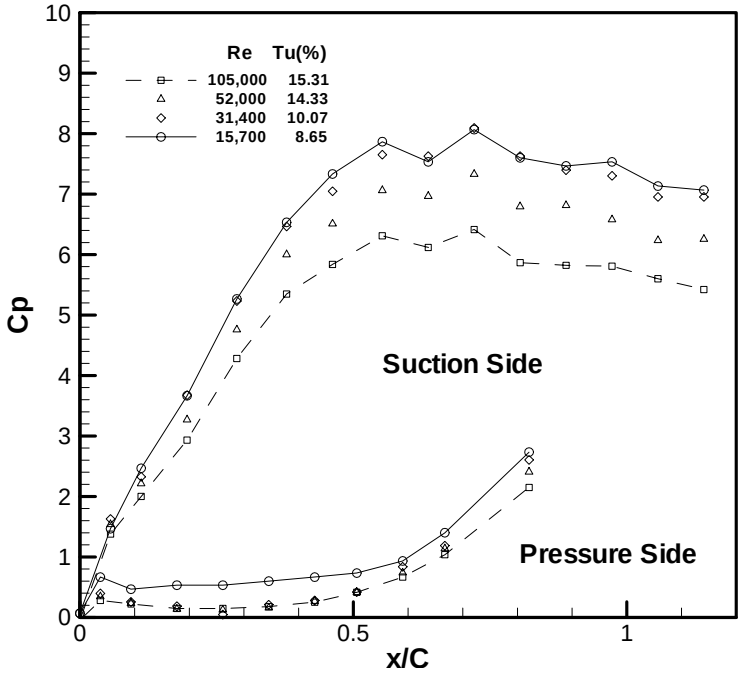

(c) the Fine Grid at Position #2

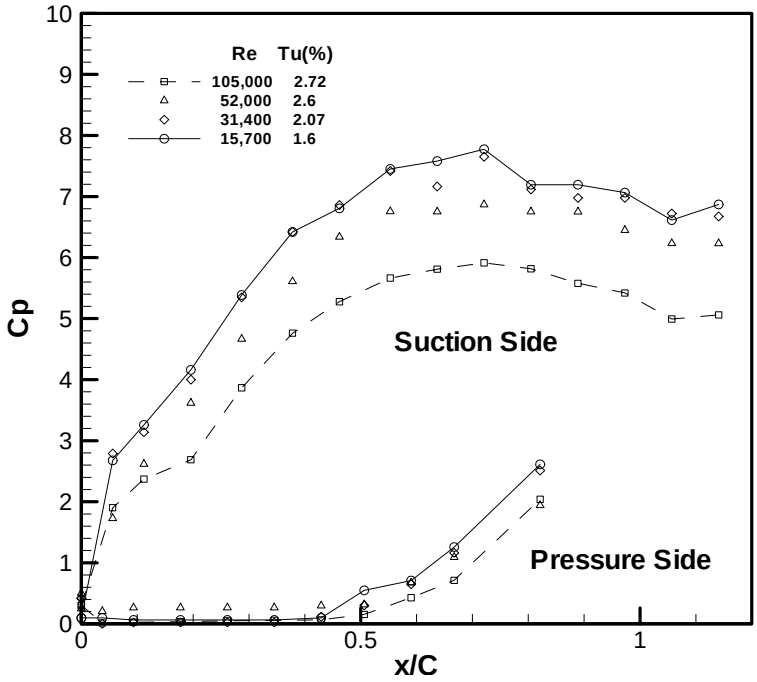

(d) The Coarse Grid at Position #1

Fig. 14 Continued

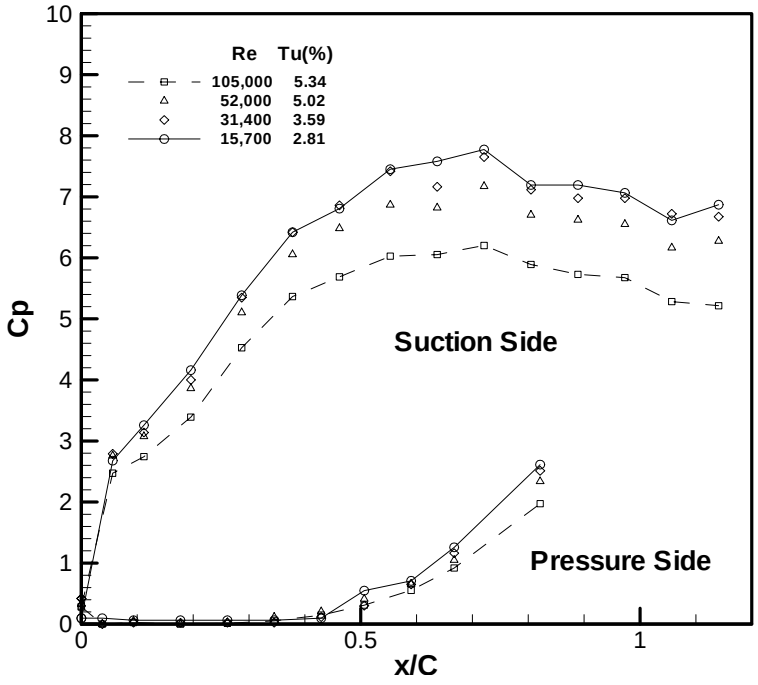

(e) The Coarse Grid at Position #2

Fig. 14 Continued

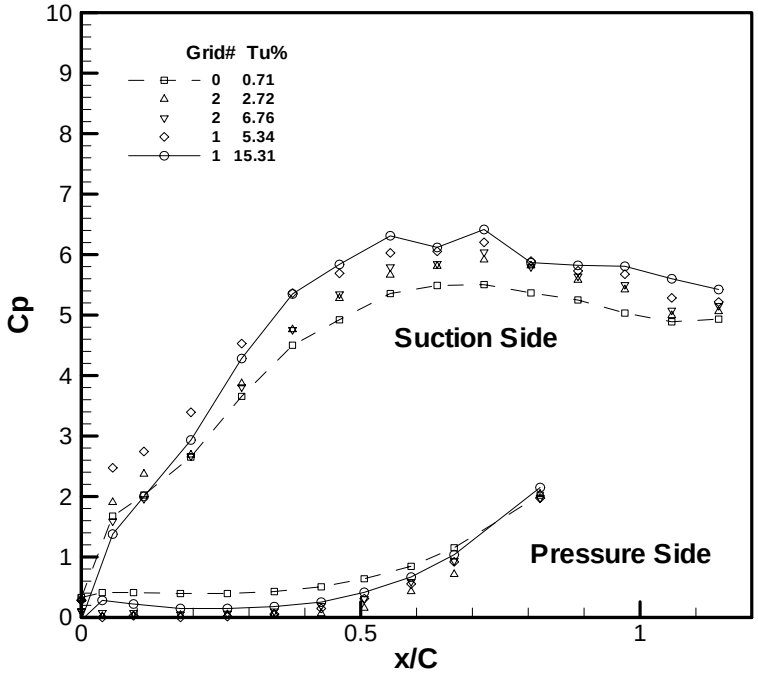

(a) Re=105,000

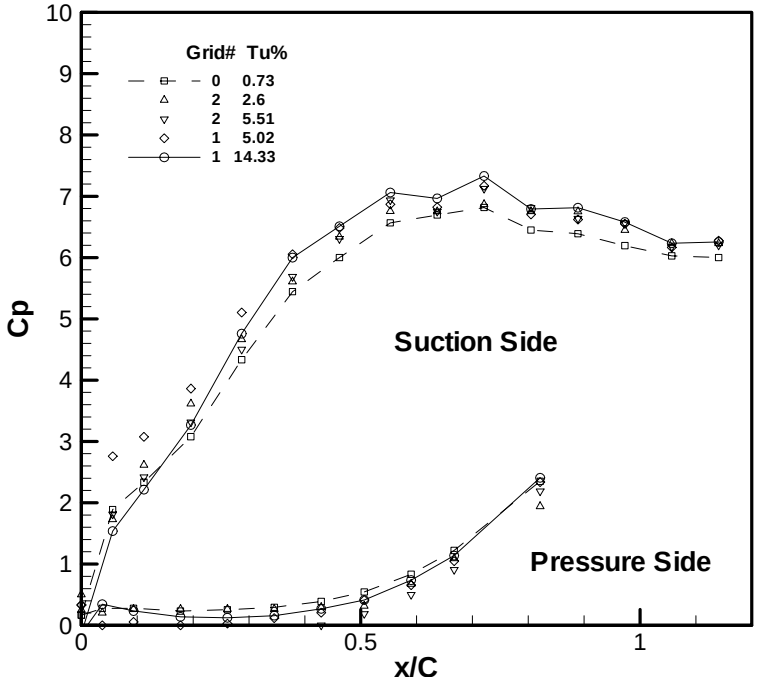

(b) Re=52,000

Fig. 15 Effect of Turbulence Intensity on Local Pressure Coefficient Distribution

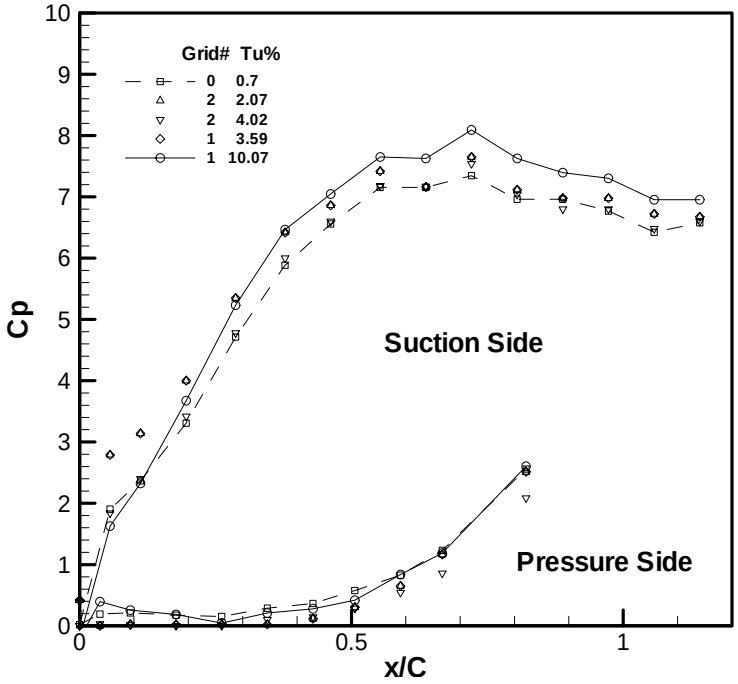

(c) Re=31,400

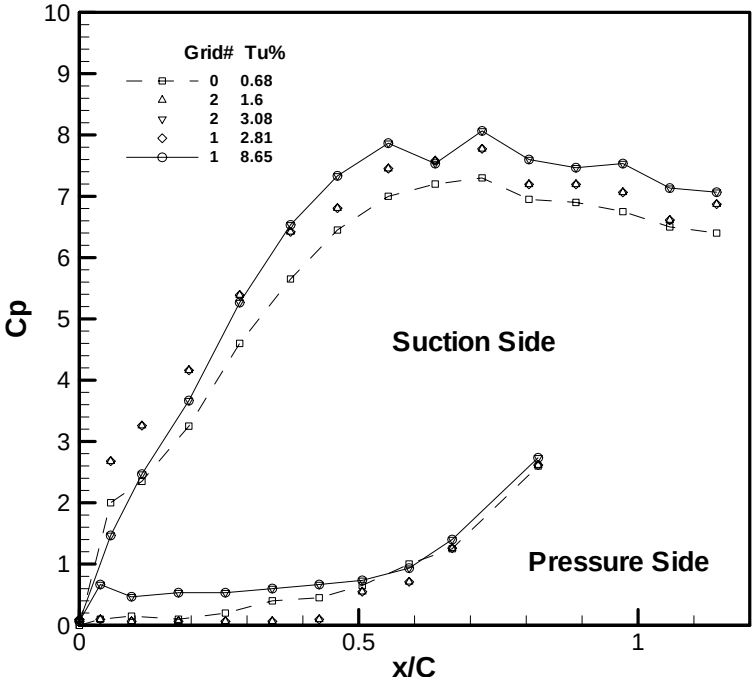

(d) Re=15,700

Fig. 15 Continued

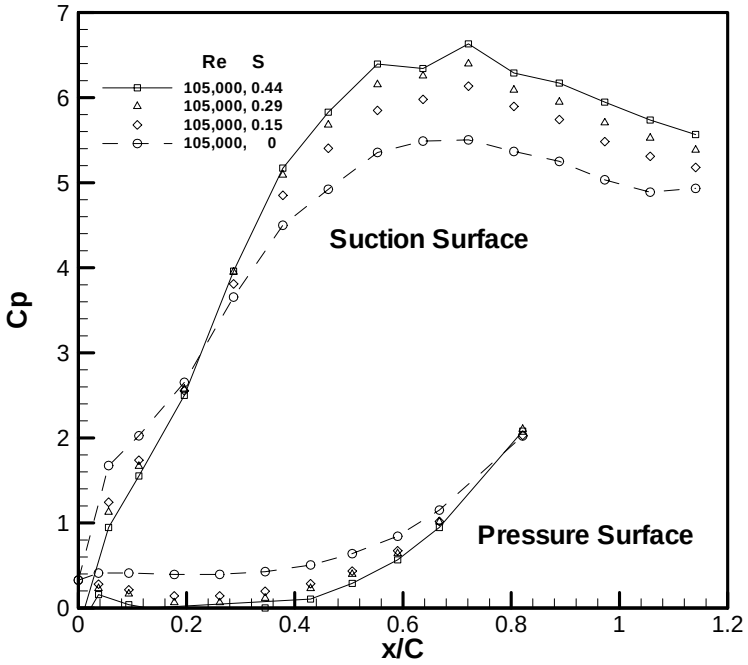

(a) Re=105,000

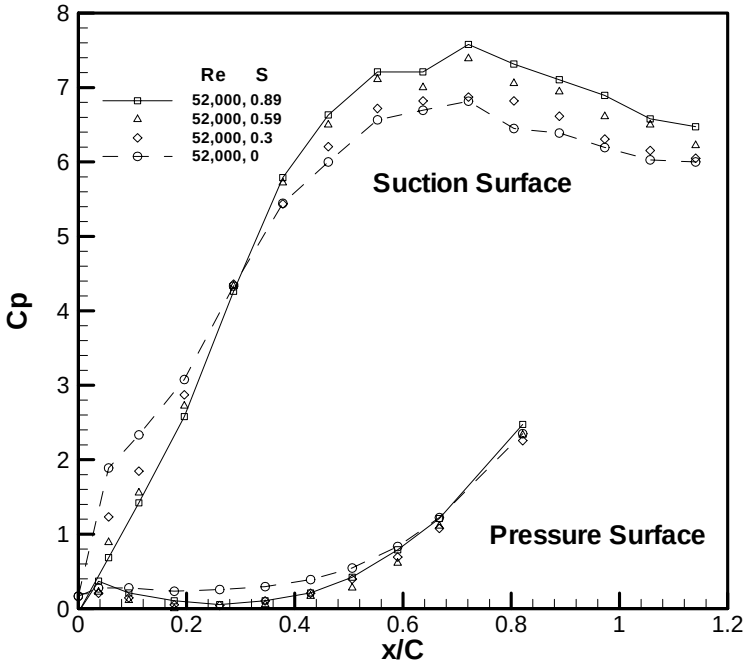

(b) Re=52,000

Fig. 16 Effect of Strouhal Number on Local Pressure Coefficient Distribution

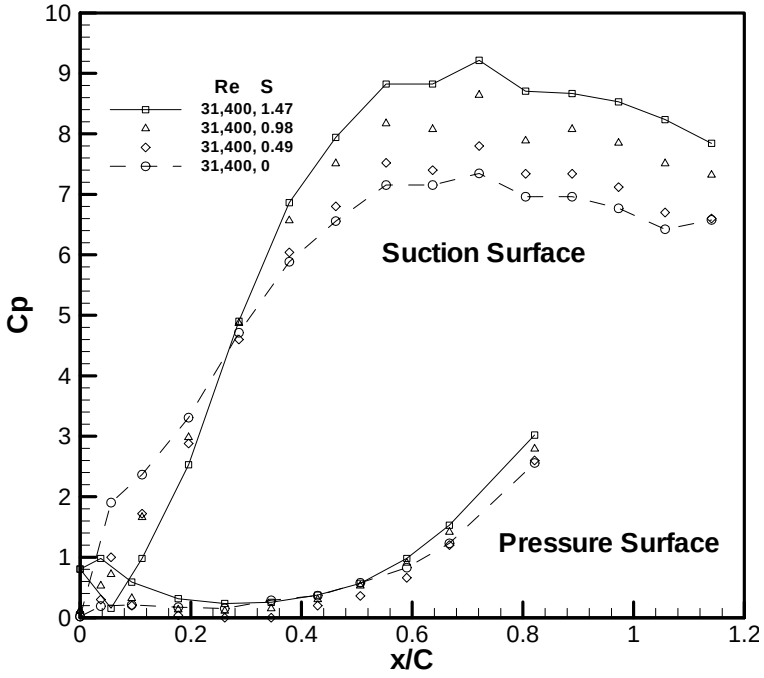

(c) Re=31,400

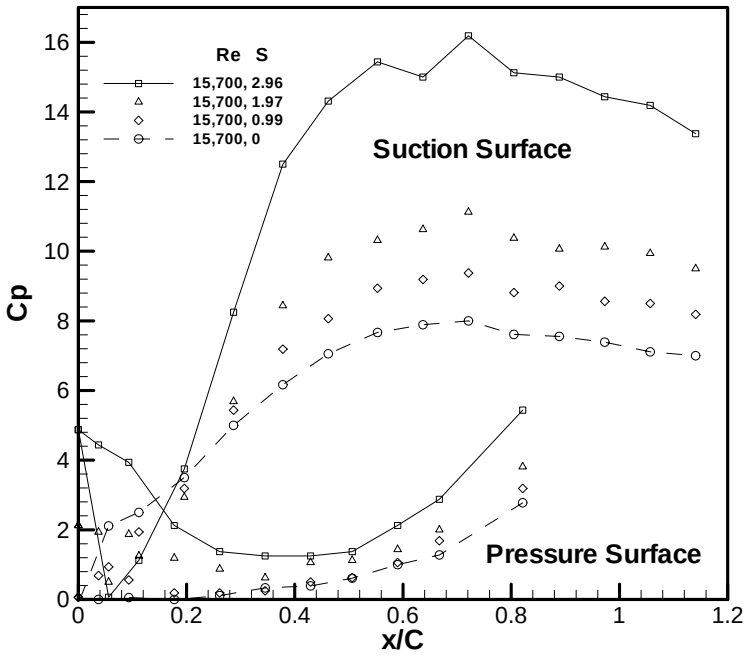

(d) Re=15,700

Fig. 16 Continued

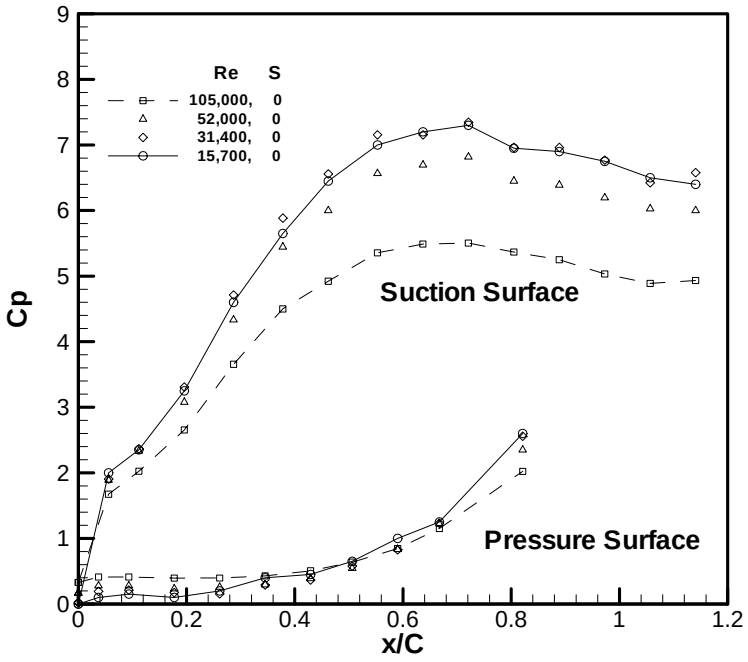

(a) 0 RPM condition

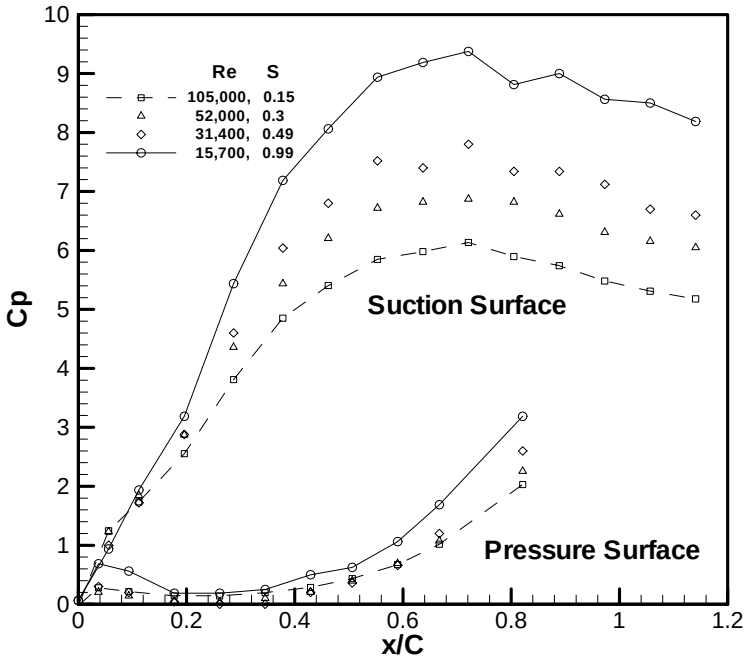

(b) 50 RPM condition

Fig. 17 Effect of Reynolds Number on Local Pressure Coefficient Distribution

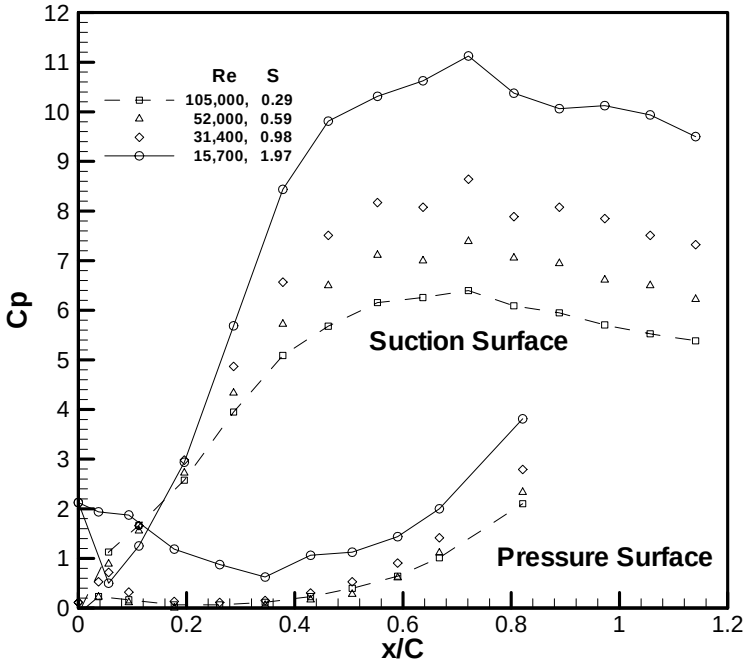

(c) 100 RPM condition

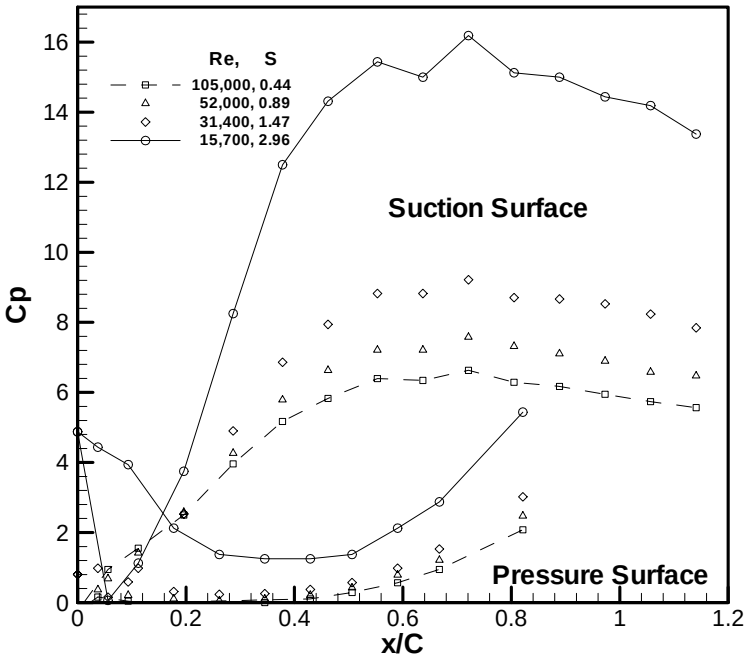

(d) 150 RPM condition

Fig. 17 Continued

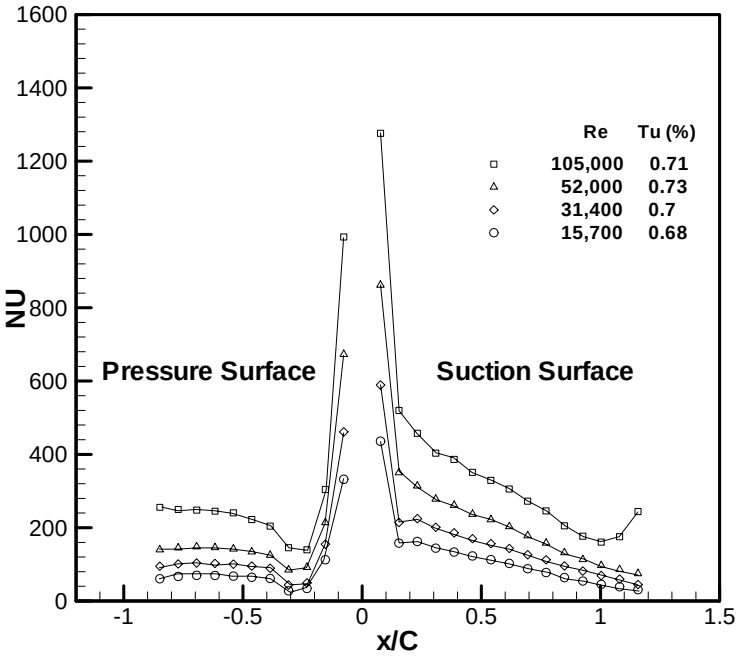

(a) The No Grid Case

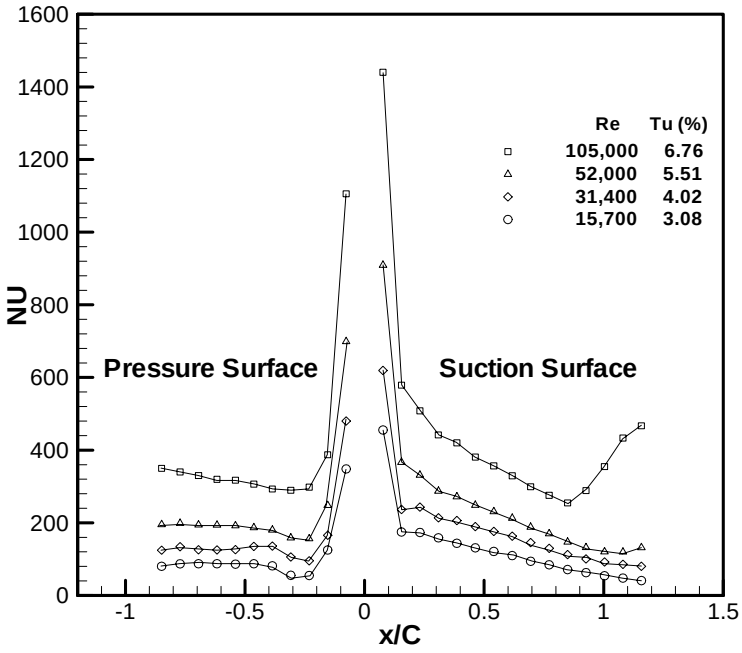

(b) The Fine Grid at Position #1 (21Cm Upstream)

Fig. 18 Effect of Reynolds Number on Local Nusselt Number Distribution

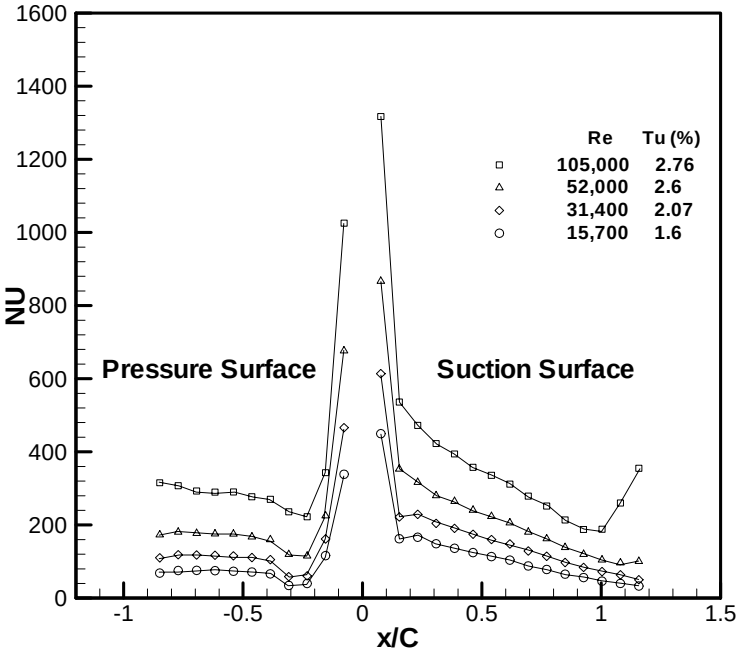

(c) The Fine Grid at Position #2 (60Cm Upstream)

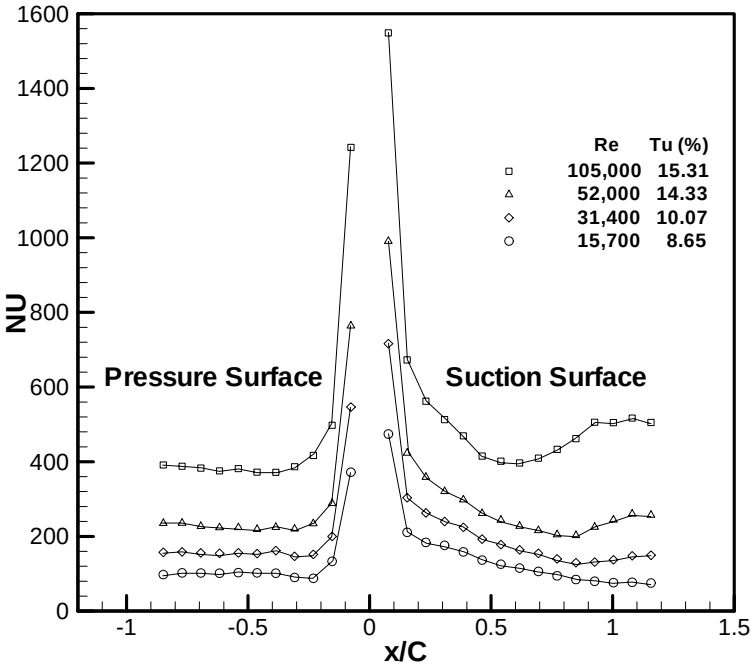

(d) Position #1 (21Cm Upstream)

Fig. 18 Continued

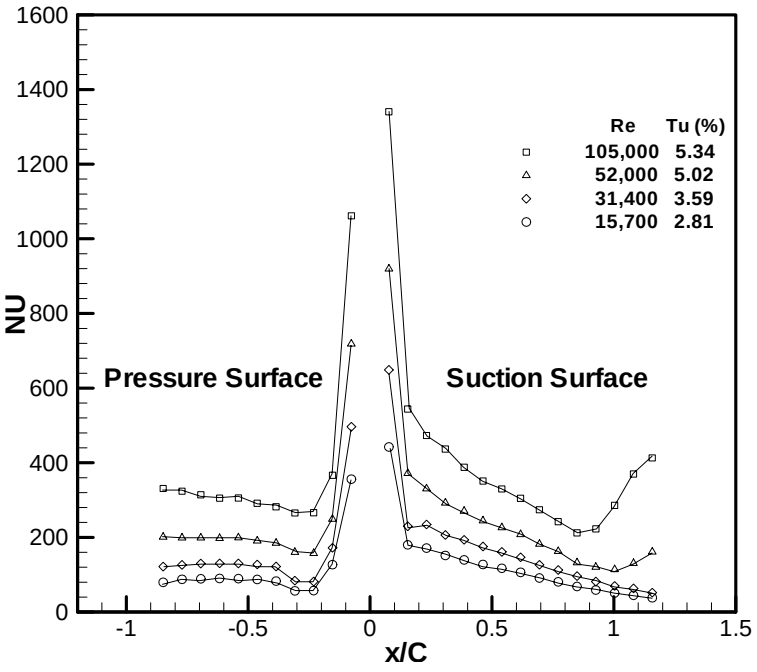

(e) Position #2 (60Cm Upstream)

Fig. 18 Continued

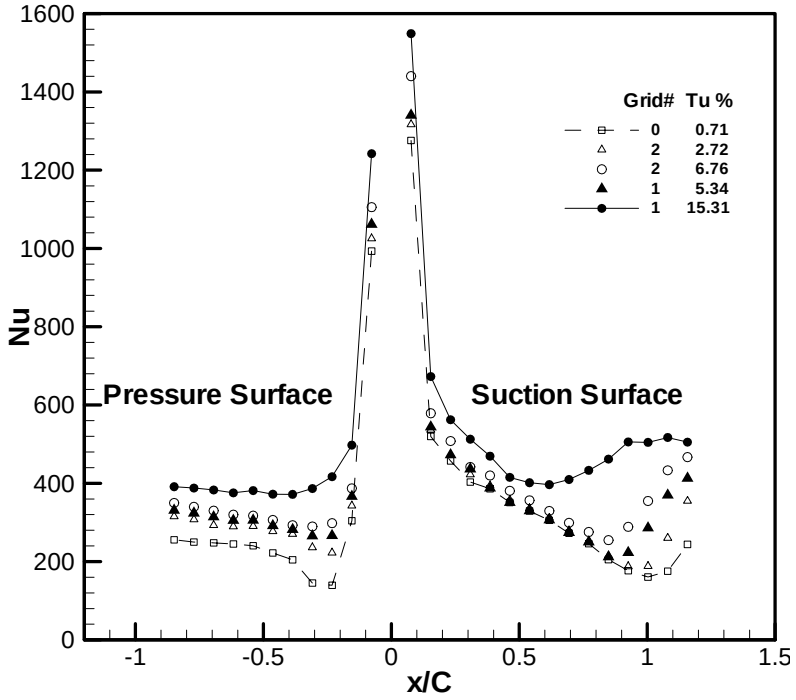

(a) Re = 105,000

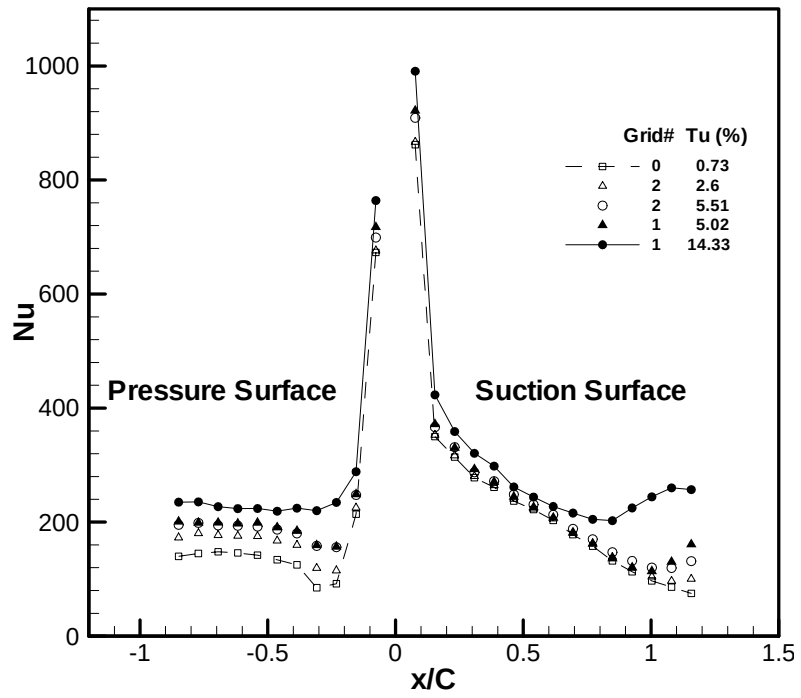

(b) Re = 52,000

Fig. 19 Effect of Turbulence Intensity on Local Nusselt Number Distribution

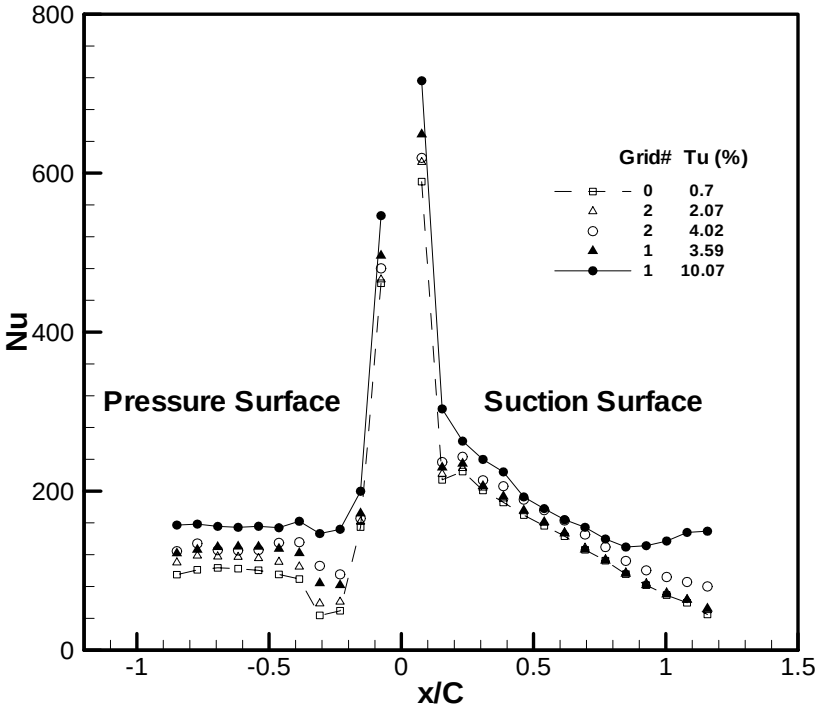

(c) Re = 31,000

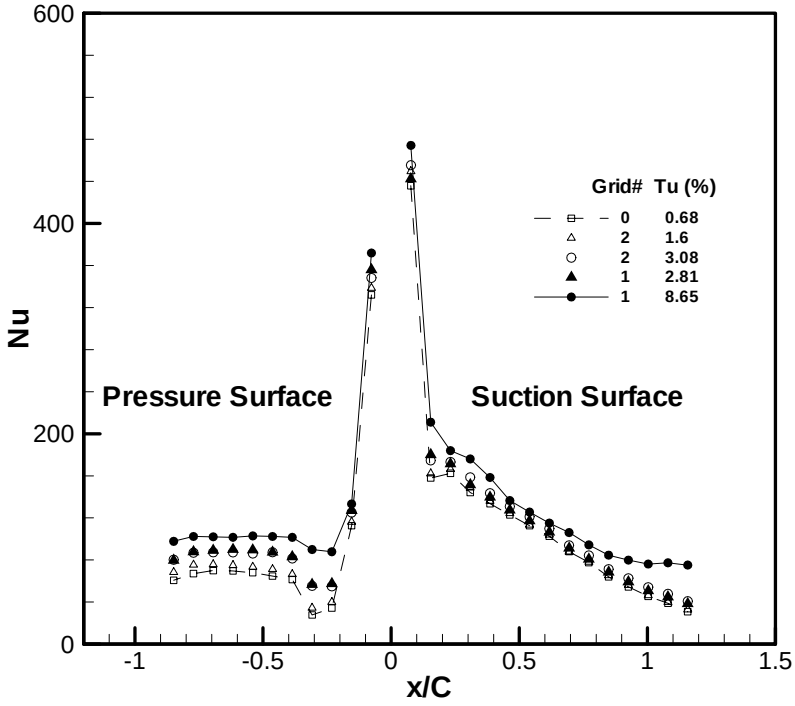

(d) Re = 15,700

Fig. 19 Continued

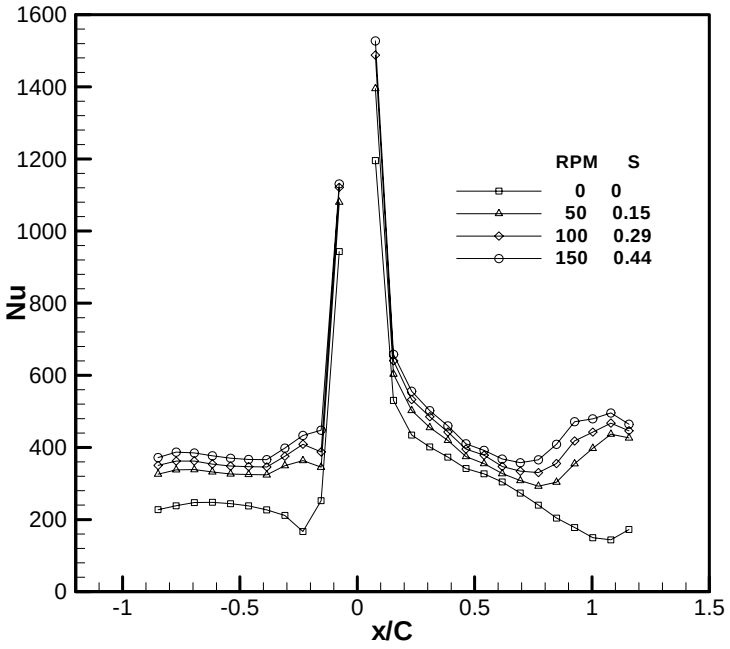

(a) Re = 105,000

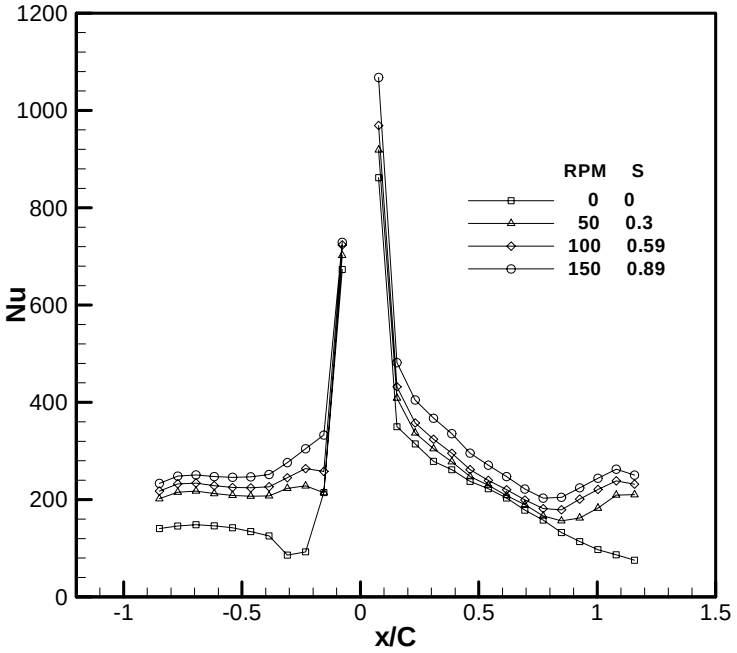

(c) Re = 52,000

Fig. 20 Effect of Strouhal Number on Local Nusselt Number Distribution

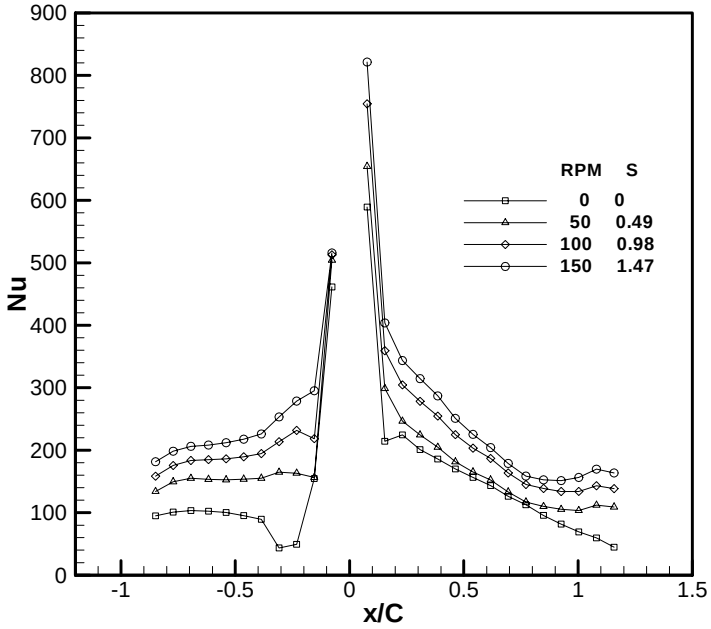

(c) Re = 31,400

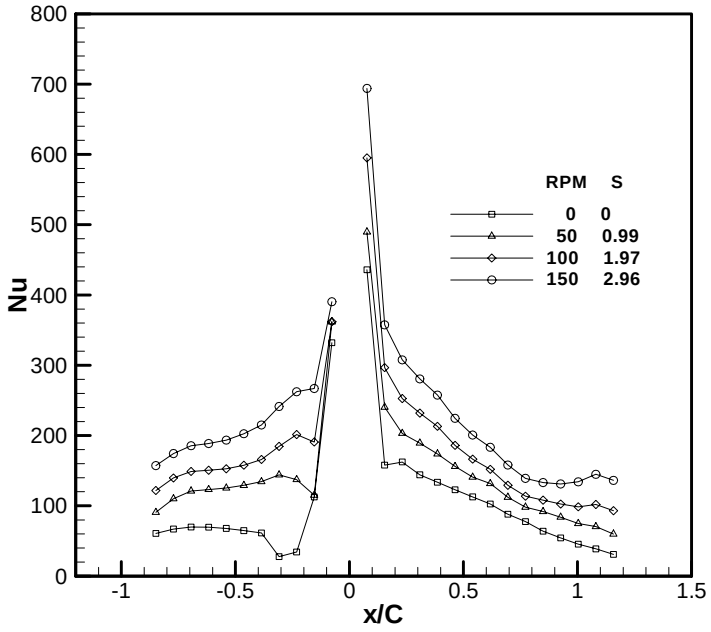

(d) Re = 15,700

Fig. 20 Continued

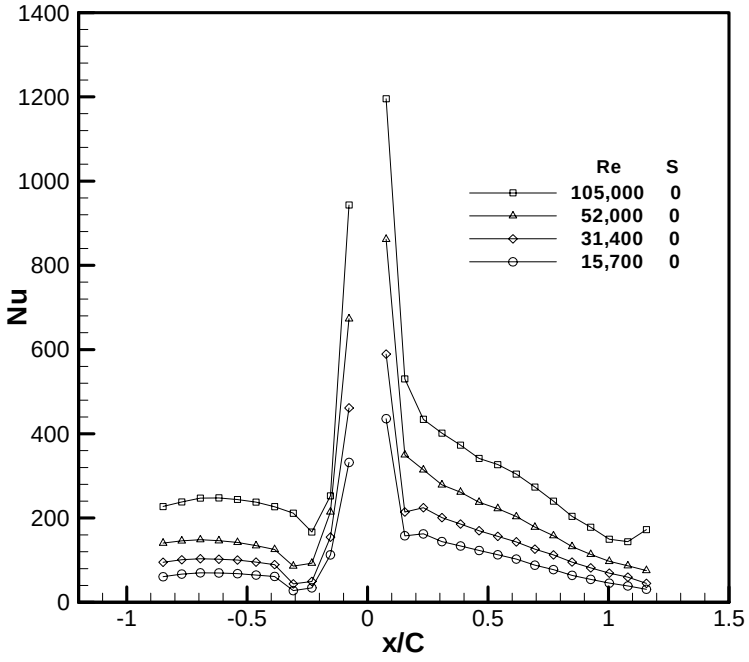

(a) 0 RPM

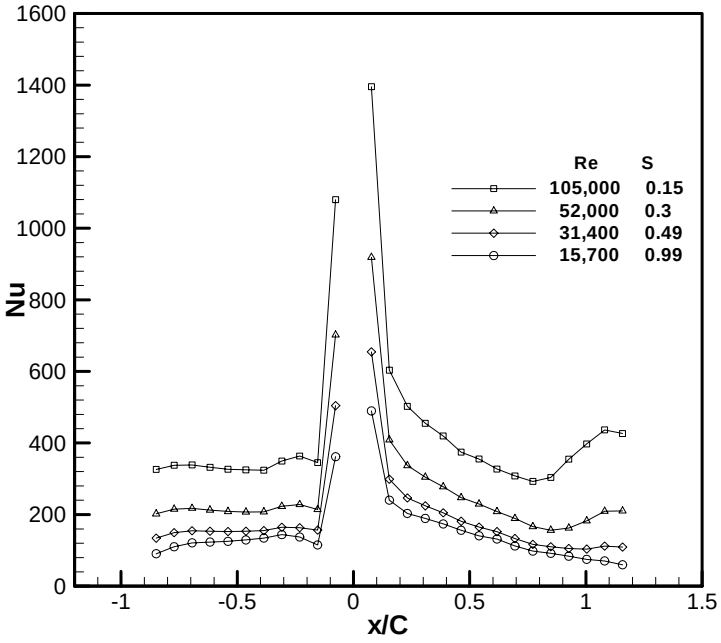

(b) 50 RPM

Fig. 21 Effect of Reynolds Number on Local Nusselt Number Distribution

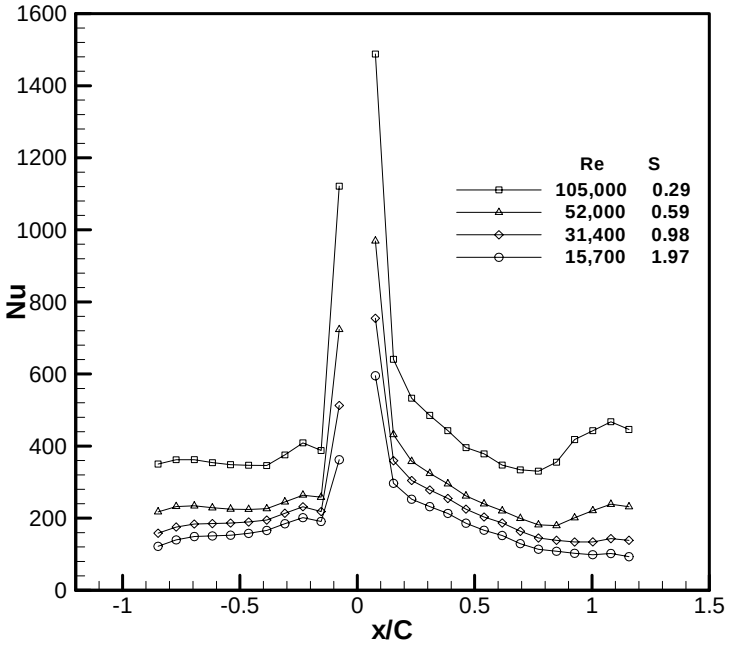

(c) 100 RPM

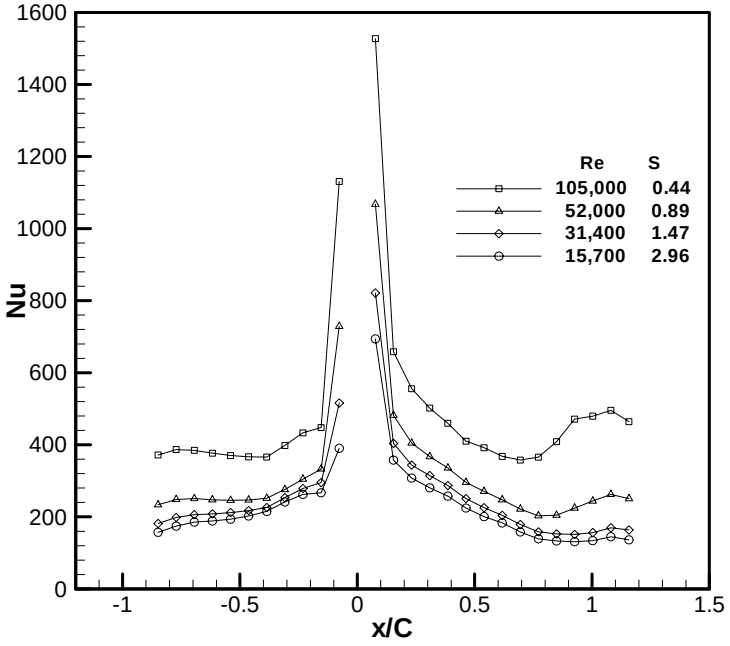

(d) 150 RPM

Fig. 21 Continued

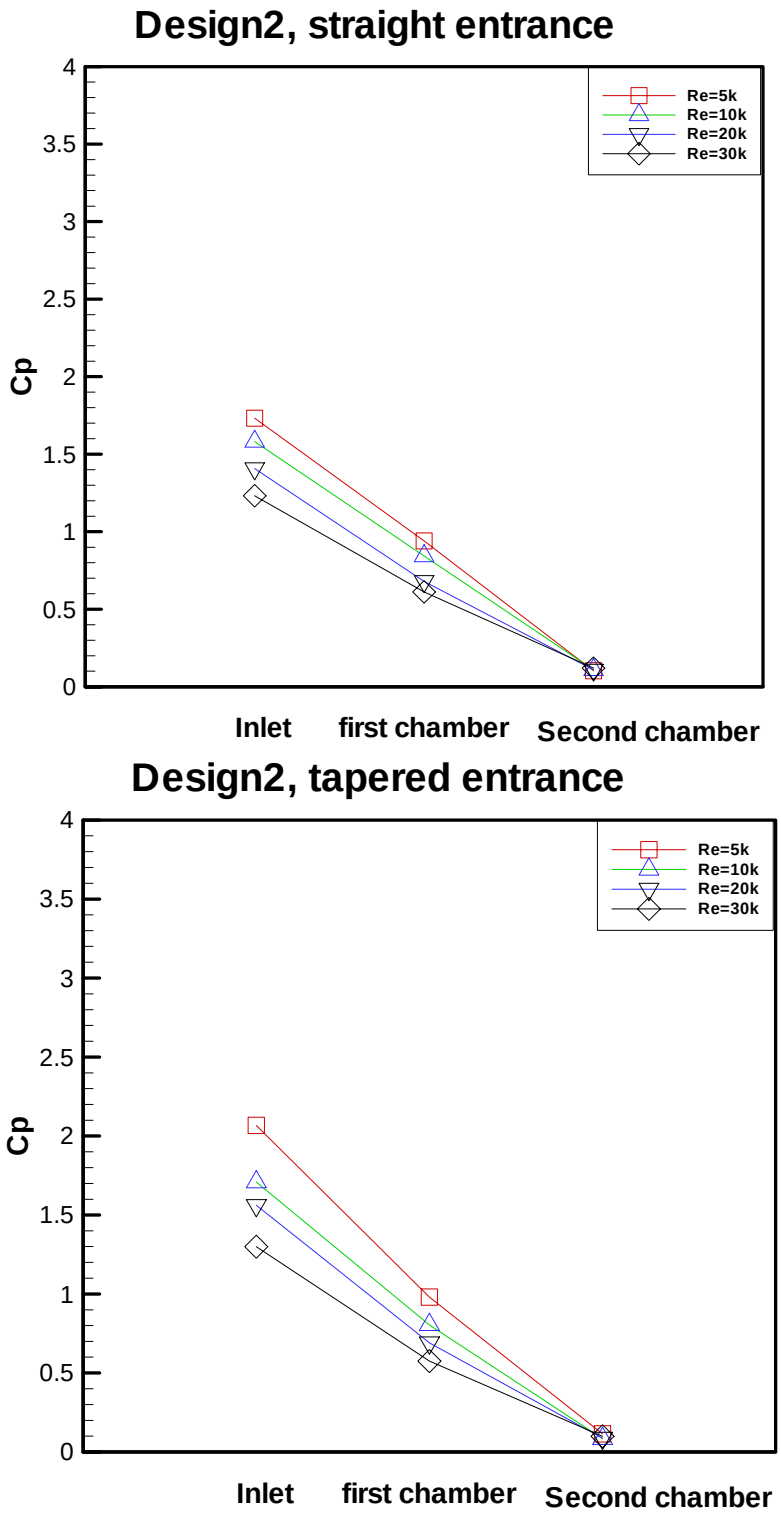

Fig. 22 Effect of Reynolds Number on the Averaged Pressure Coefficient at Each Chamber

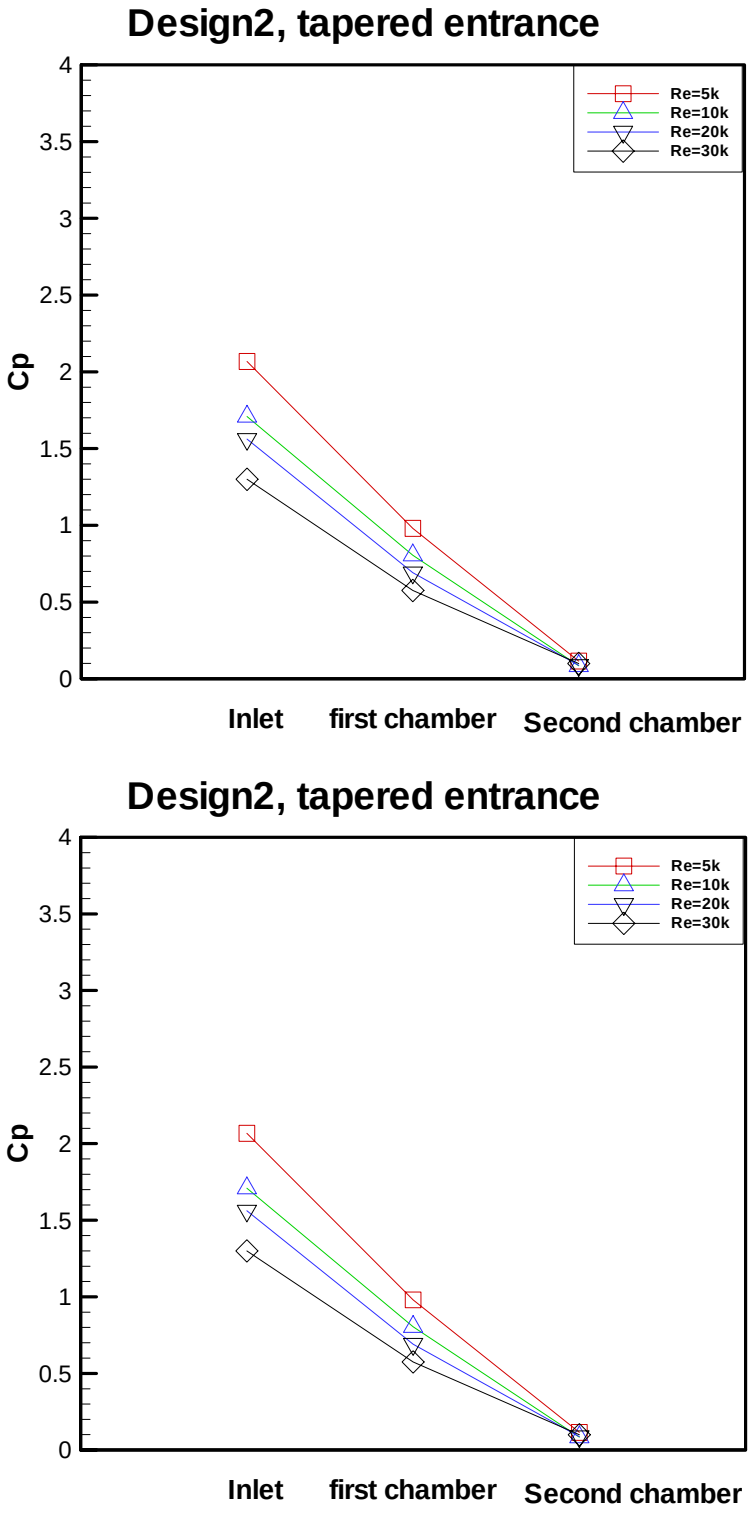

Fig. 22 Continued

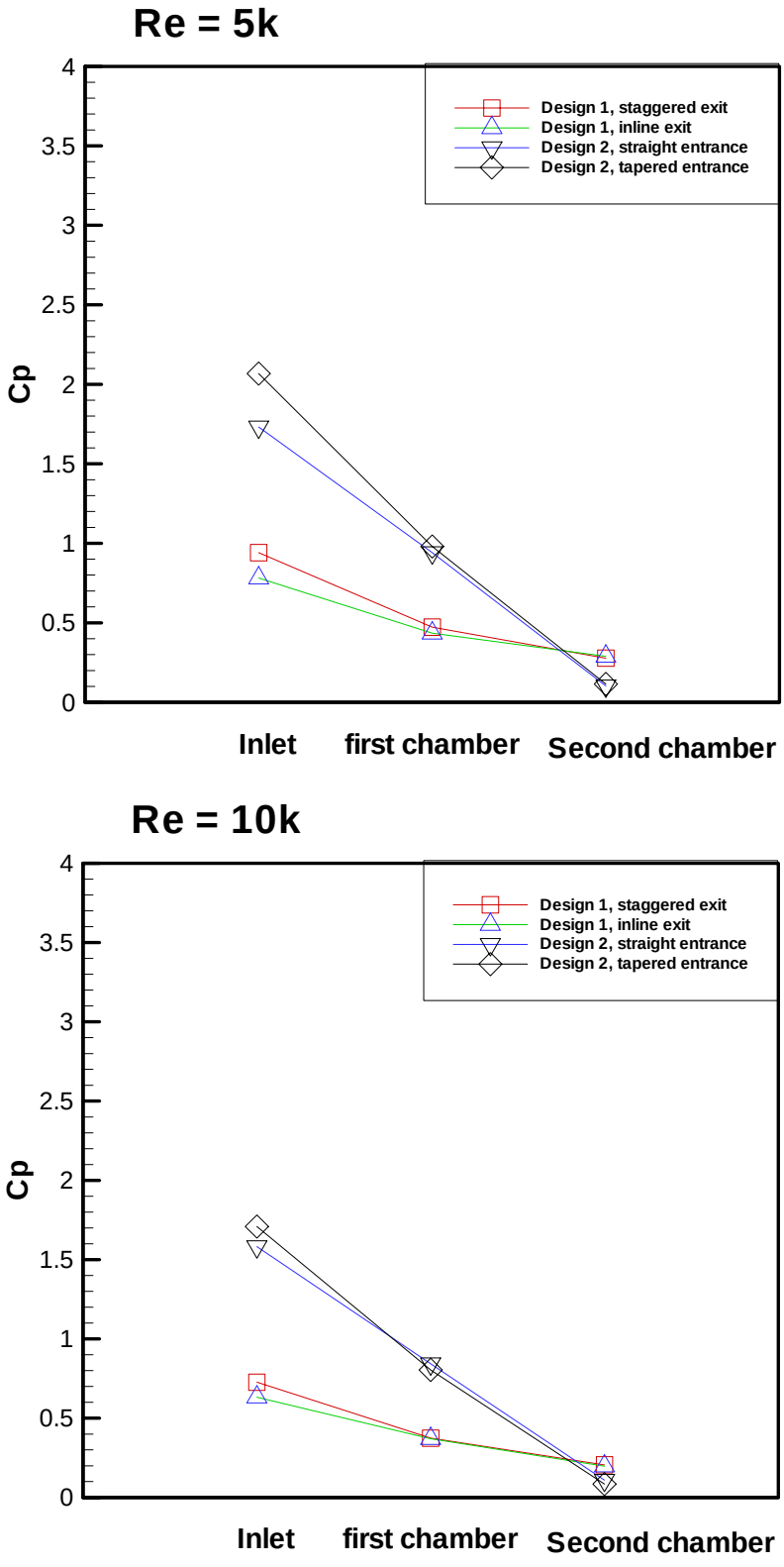

Fig. 23 Effect of the Design on Averaged Pressure Coefficient

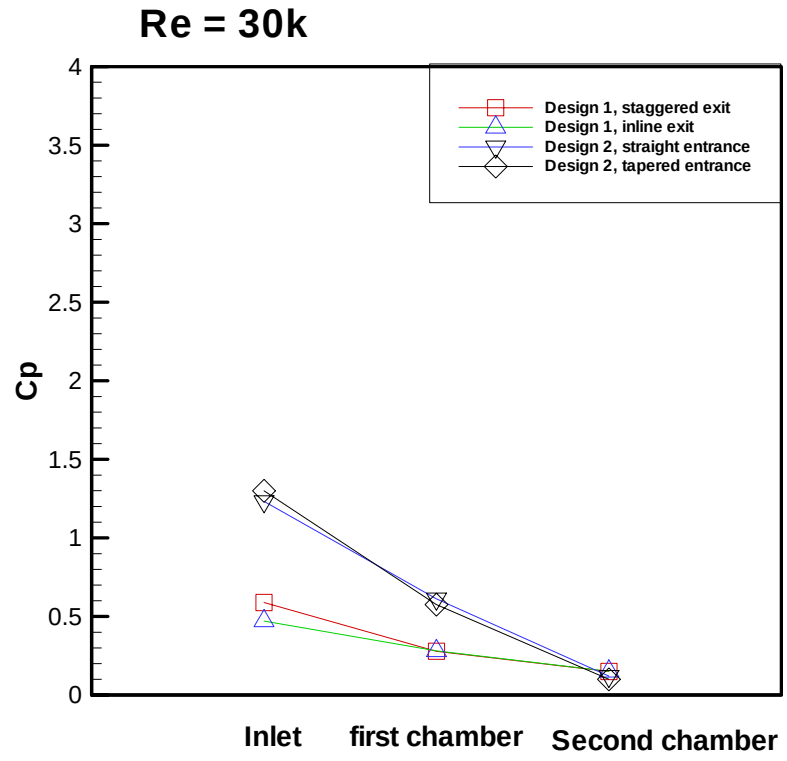

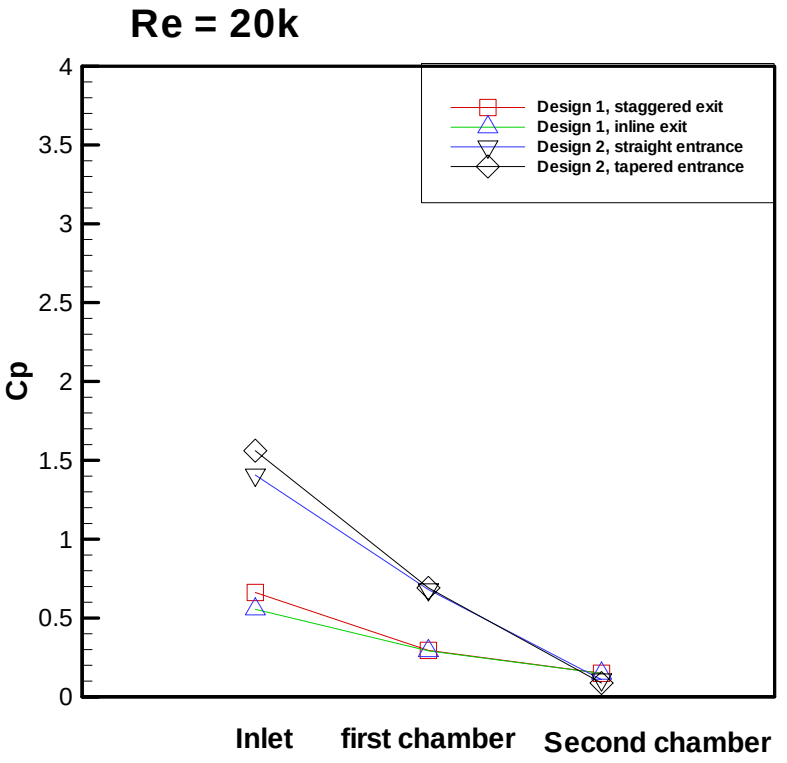

Fig. 23 Continued

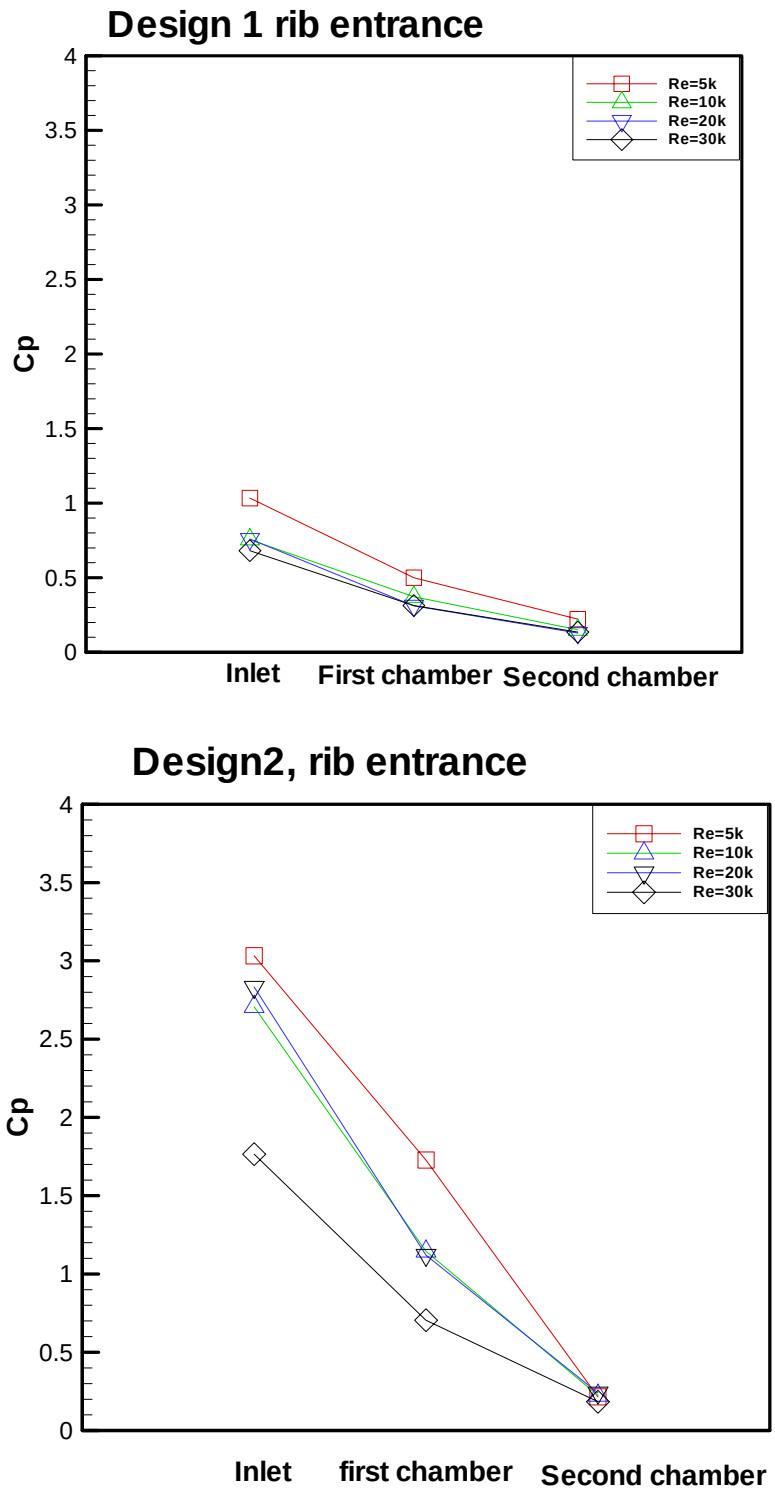

Fig. 24 Effect of Reynolds Number on the Averaged Pressure Coefficient with Ribs at Each Chamber

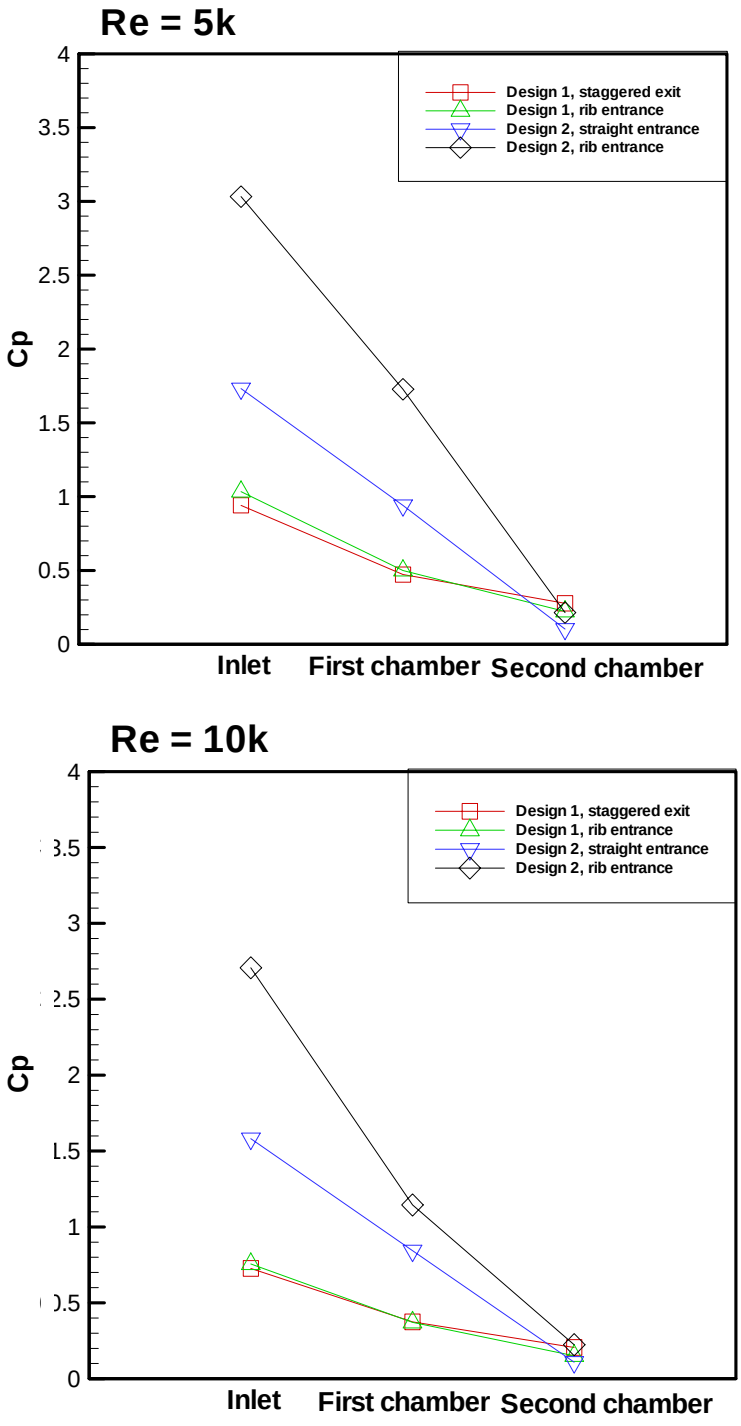

Fig. 25 Effect of the Design on Pressure Coefficient with Ribs

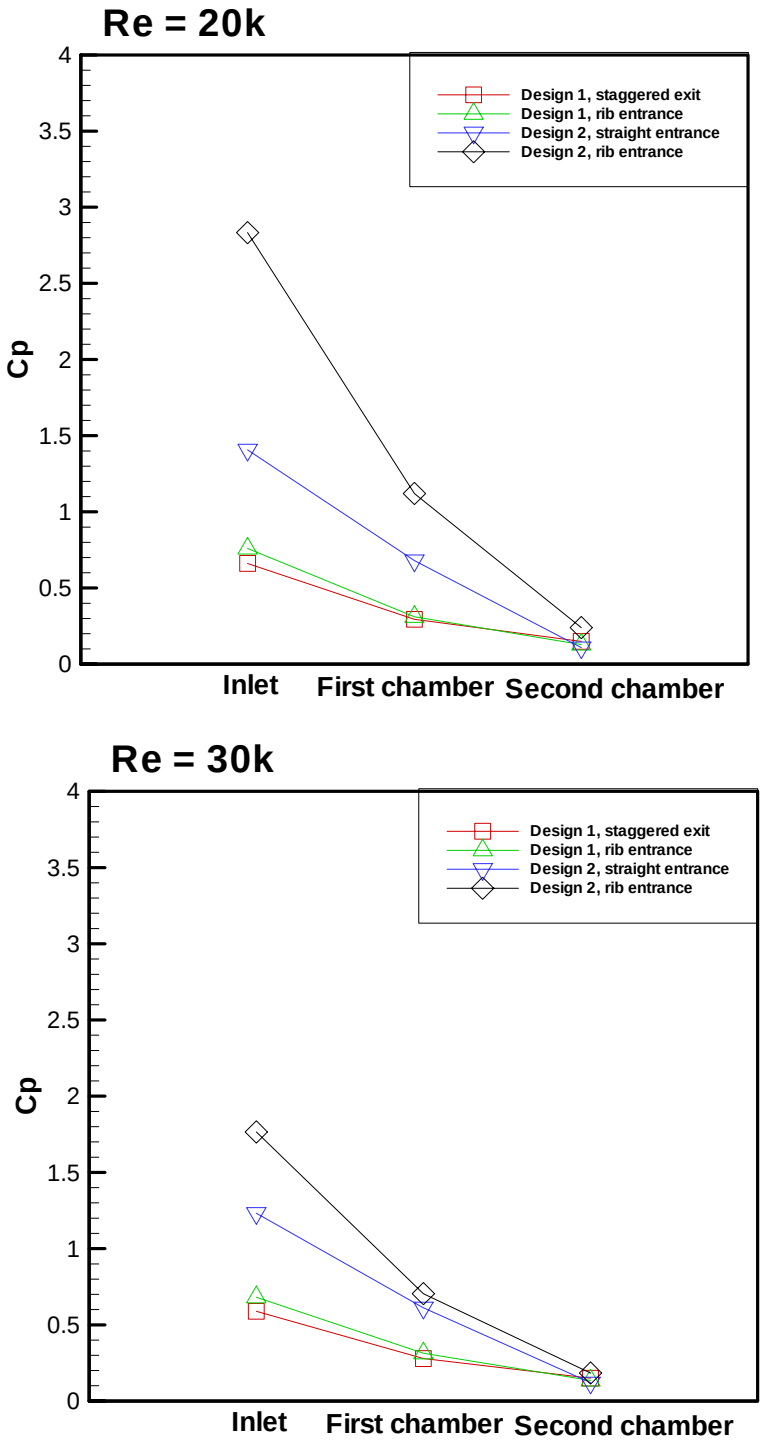

Fig. 25 Continued

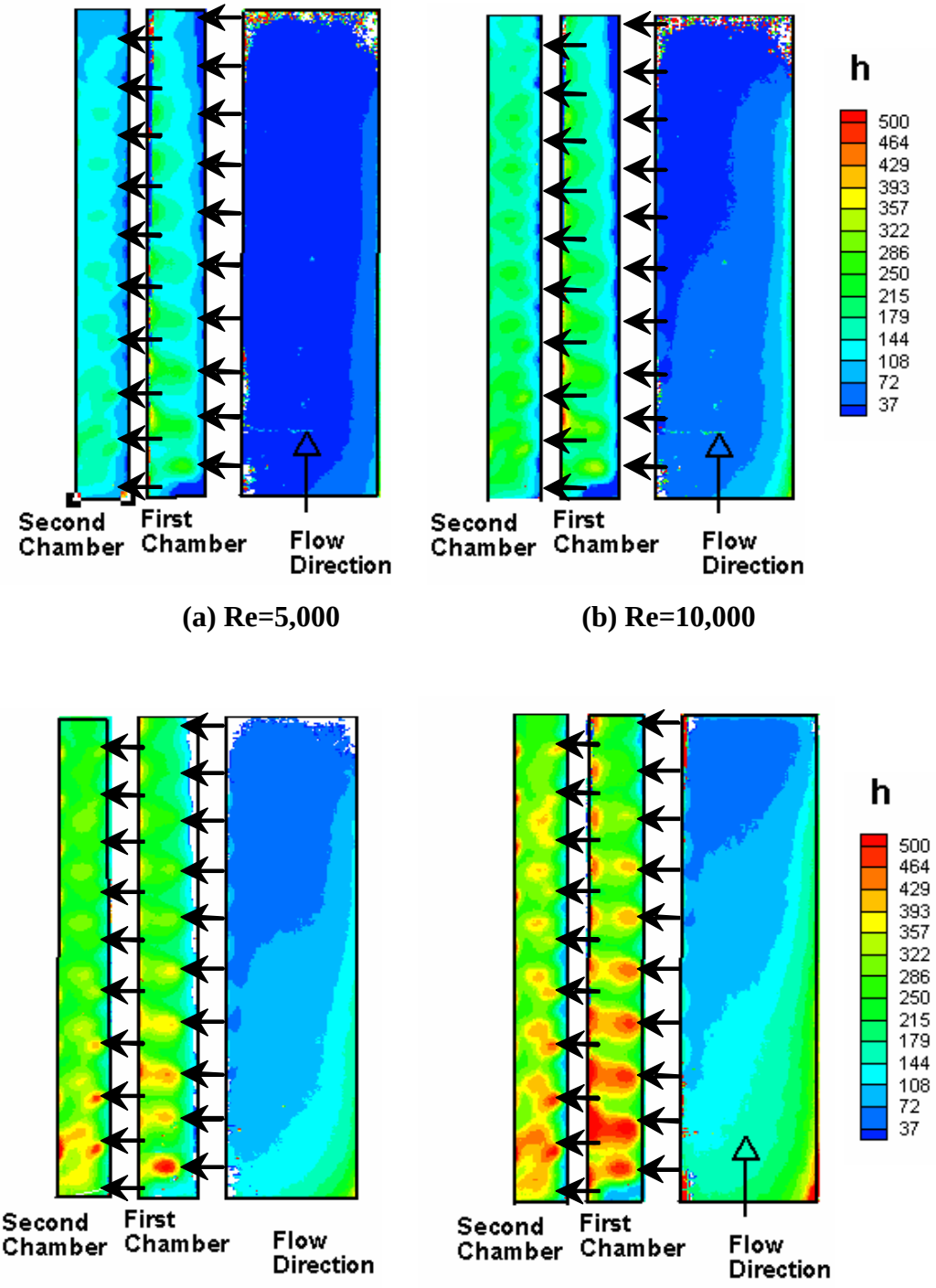

(a) Re=5,000 **(b) Re=10,000**

(c) Re=20,000 **(d) Re=30,000**

Fig. 26 Internal Heat Transfer Coefficient Distributions for Staggered Exit Slot in Design 1

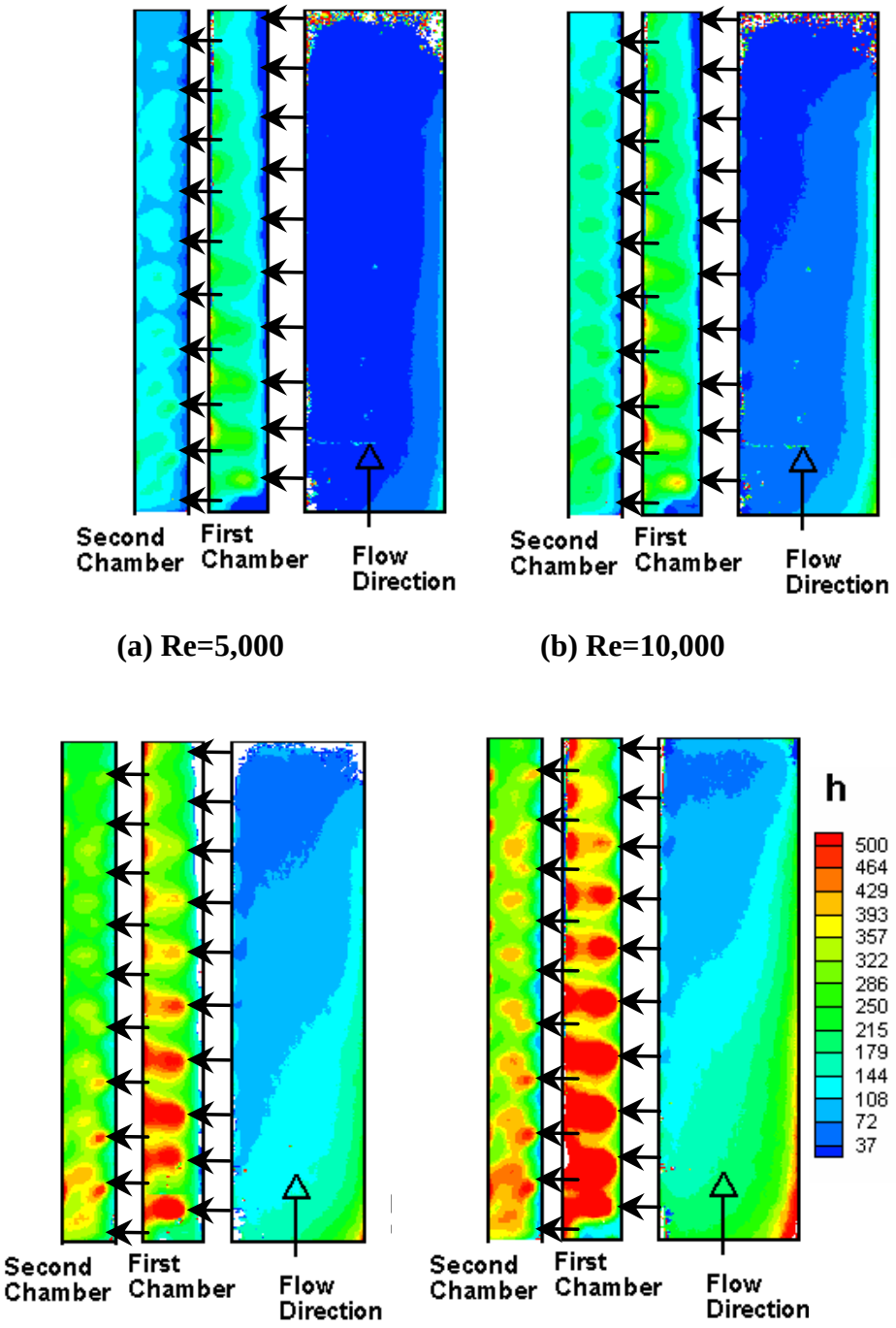

(a) Re=5,000 **(b) Re=10,000**

(c) Re=20,000 **(d) Re=30,000**

Fig. 27 Internal Heat Transfer Coefficient Distributions for Inline Exit Slot in Design 1

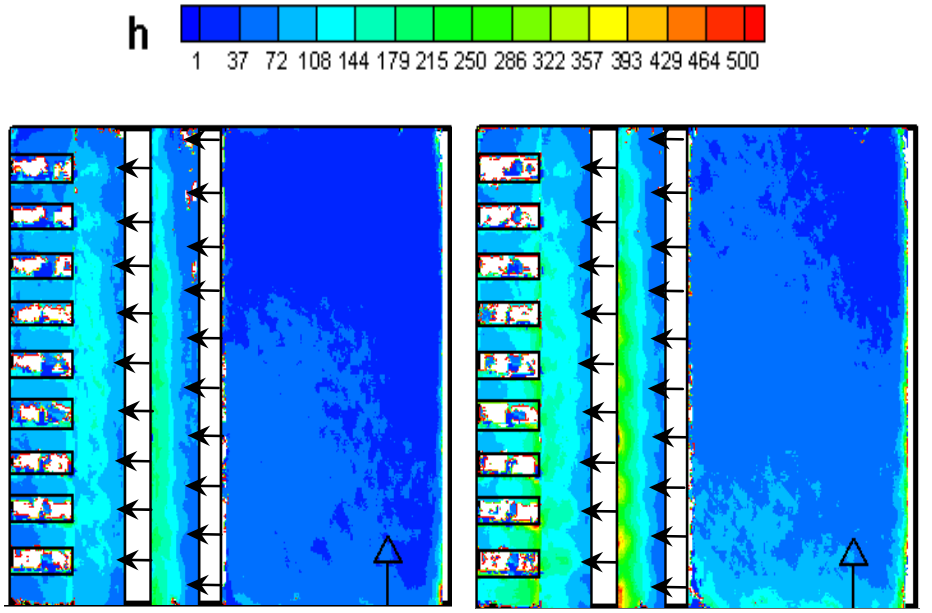

(a) Re=5,000 **(b) Re=10,000**

(c) Re=20,000 **(d) Re=30,000**

Fig. 28 Internal Heat Transfer Coefficient Distributions for the Straight Entrance in Design 2

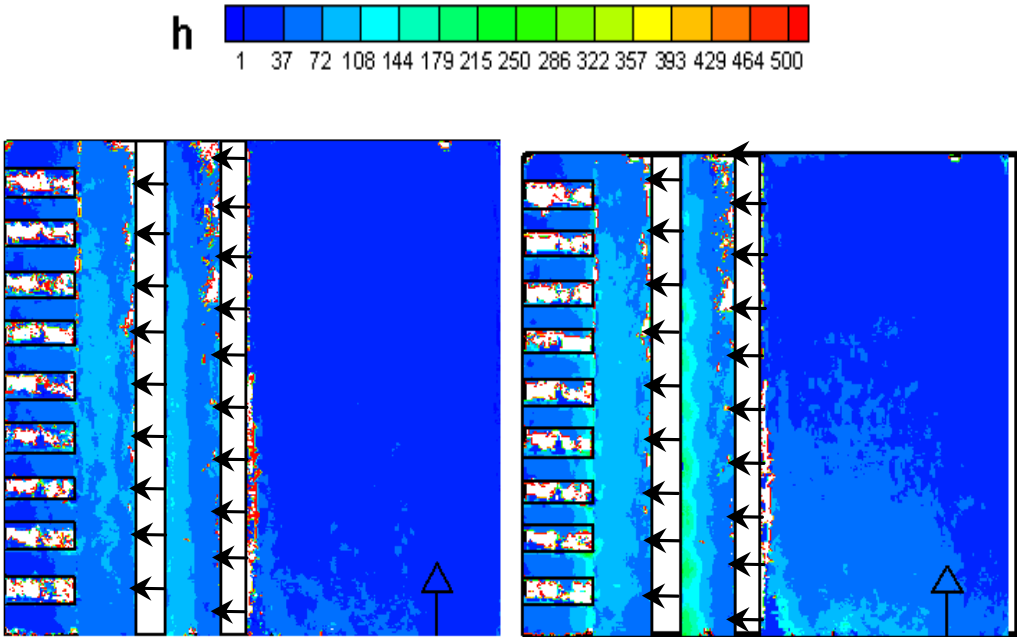

(a) Re=5,000 **(b) Re=10,000**

(c) Re=20,000 **(d) Re=30,000**

Fig. 29 Internal Heat Transfer Coefficient Distributions for Tapered Entrance in Design 2

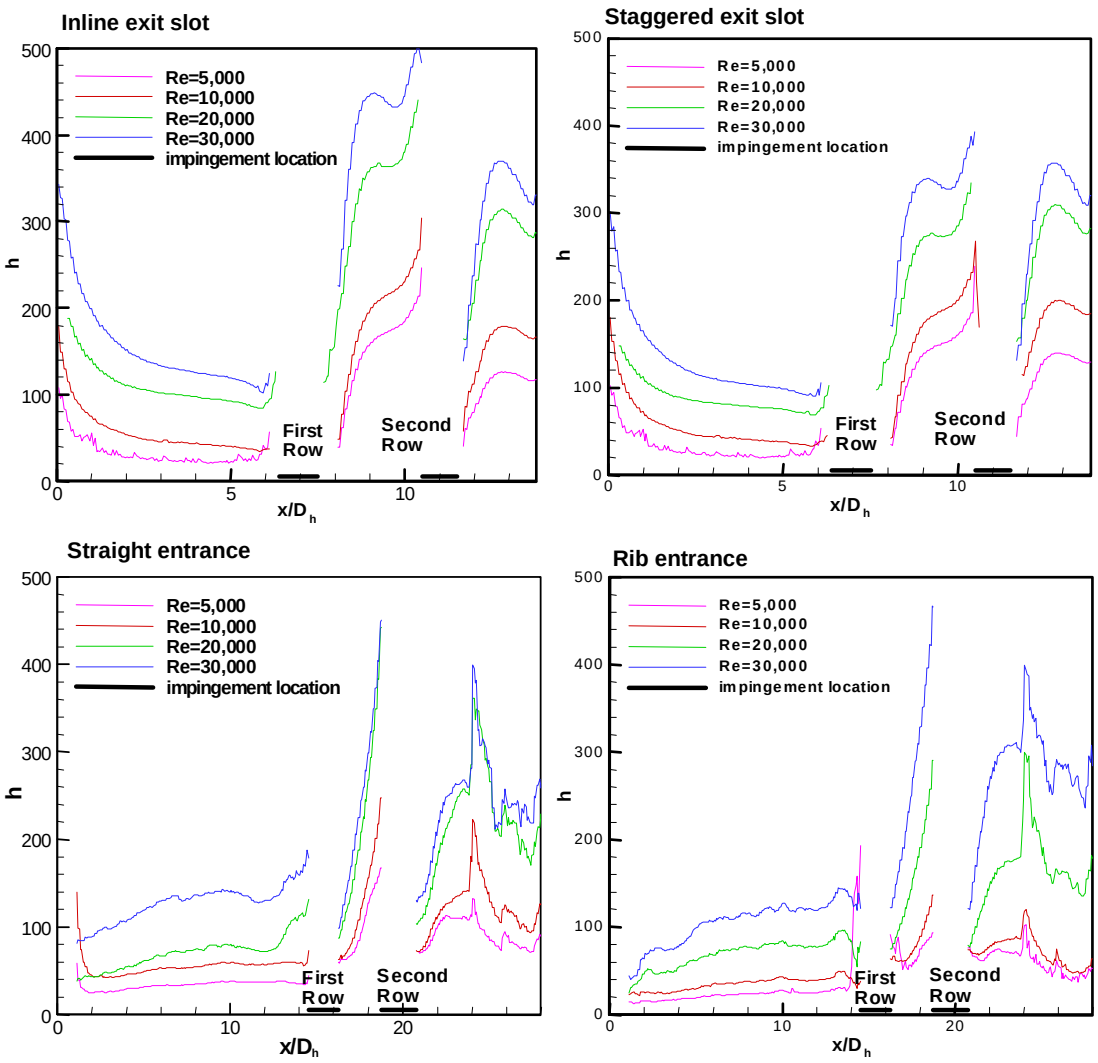

Fig. 30 Spanwise Averaged Heat Transfer Coefficient Distributions

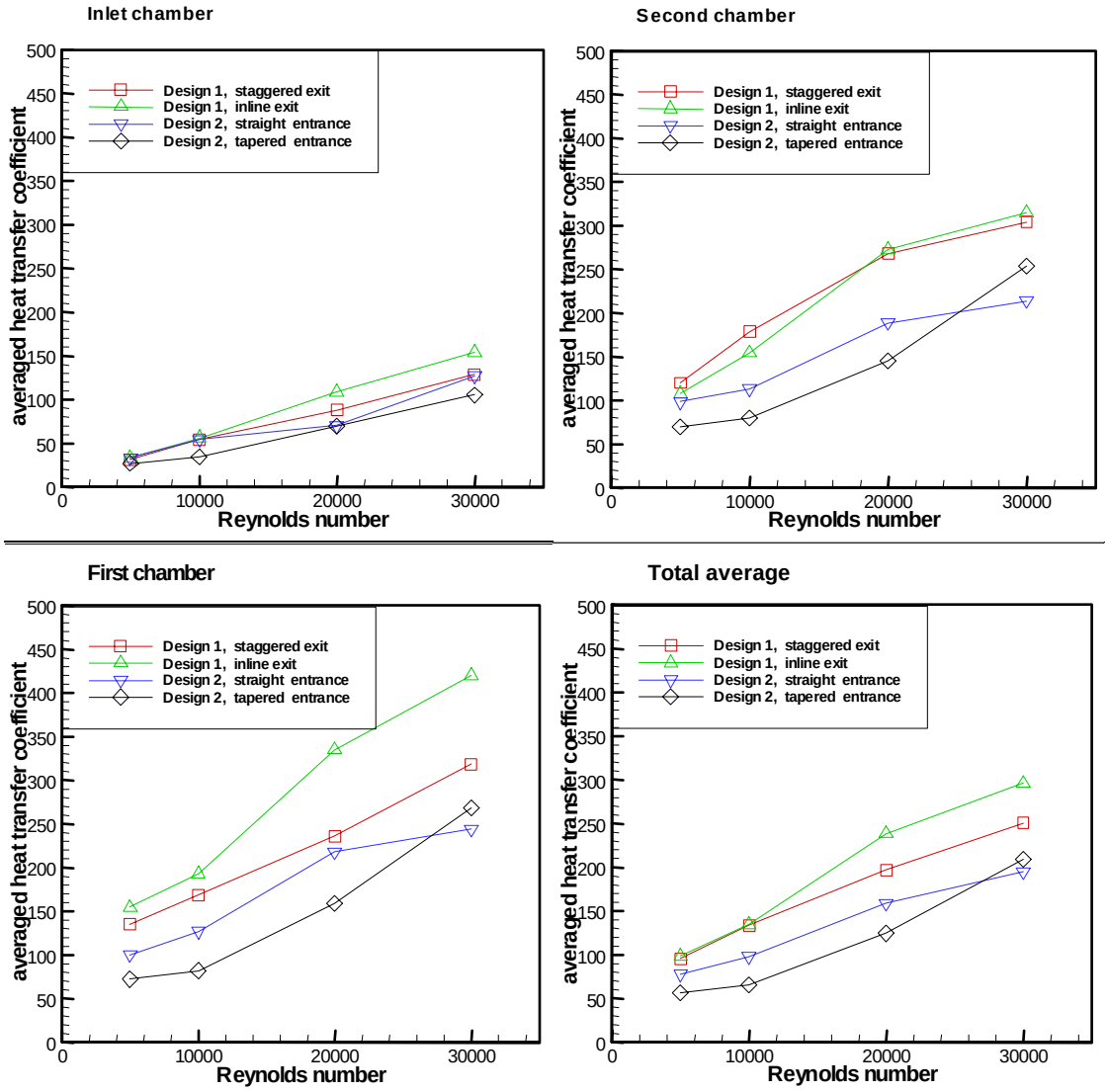

Fig. 31 Effect of the Design on Heat Transfer Coefficient

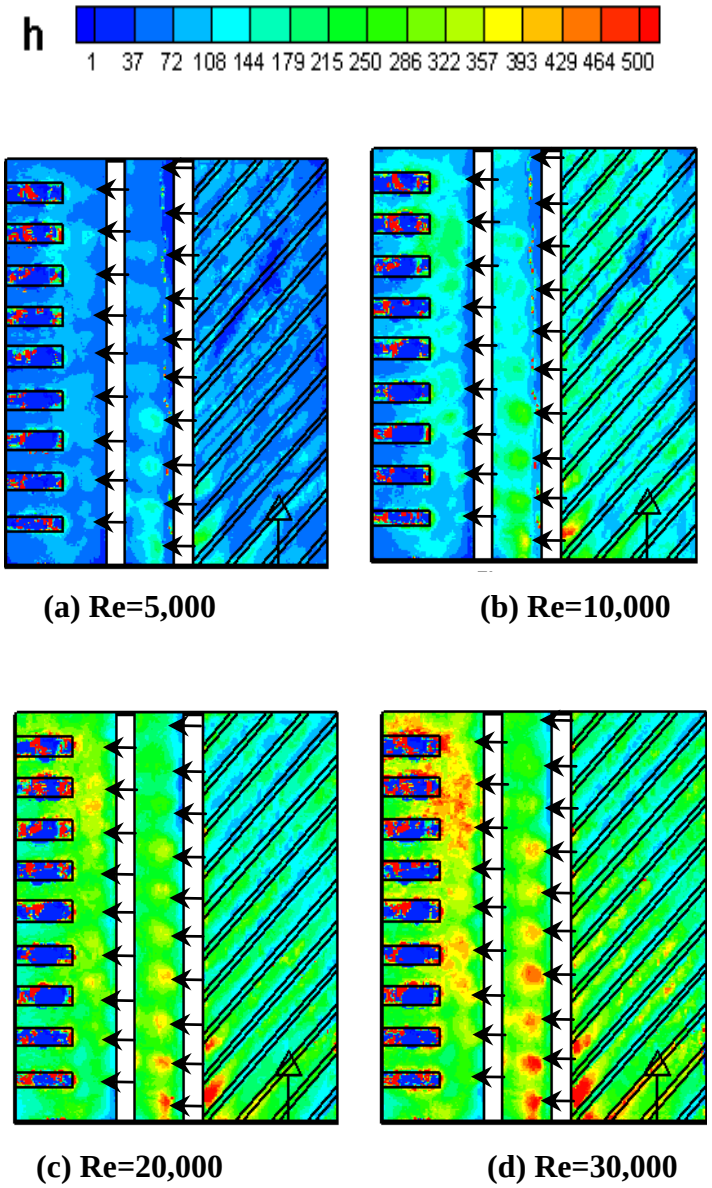

(a) Re=5,000 **(b) Re=10,000**

(c) Re=20,000 **(d) Re=30,000**

Fig. 32 Internal Heat Transfer Coefficient Distributions for Rib Entrance in Design 1

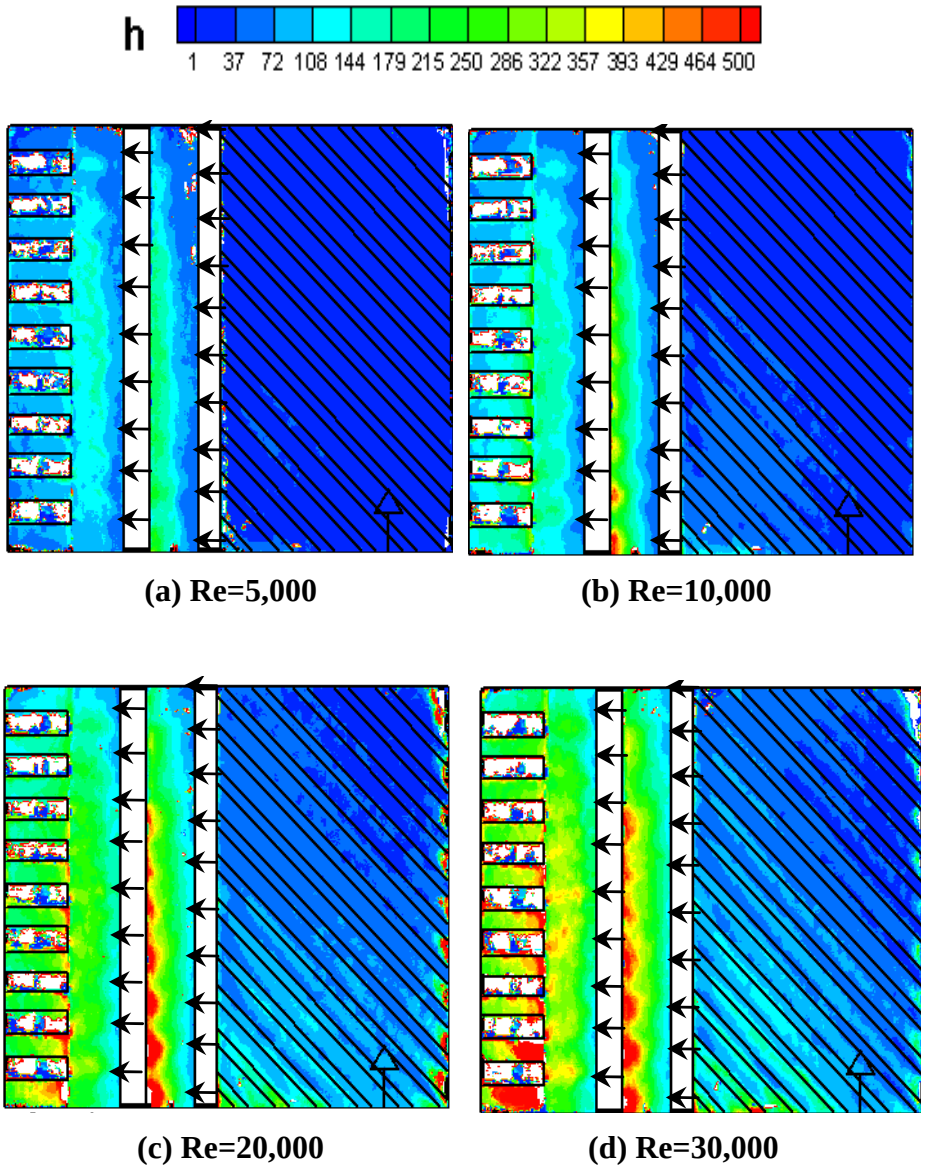

(a) Re=5,000 **(b) Re=10,000**

(c) Re=20,000 **(d) Re=30,000**

Fig. 33 Internal Heat Transfer Coefficient Distributions for Rib Entrance in Design 2

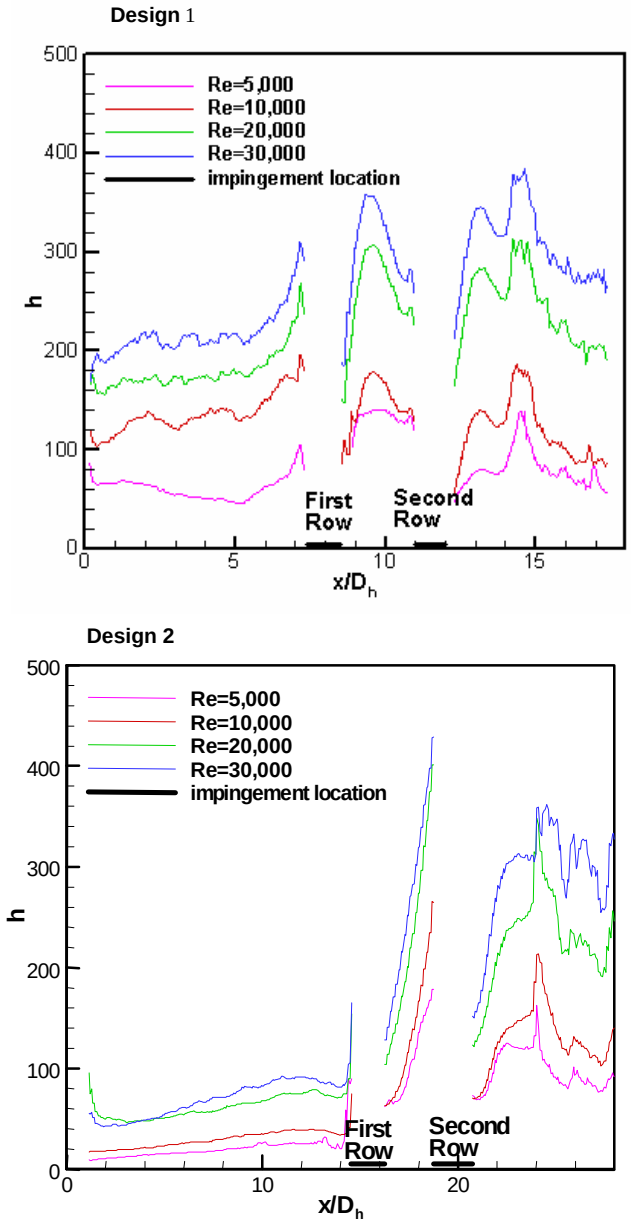

Fig. 34 Spanwise Averaged Heat Transfer Coefficient Distributions

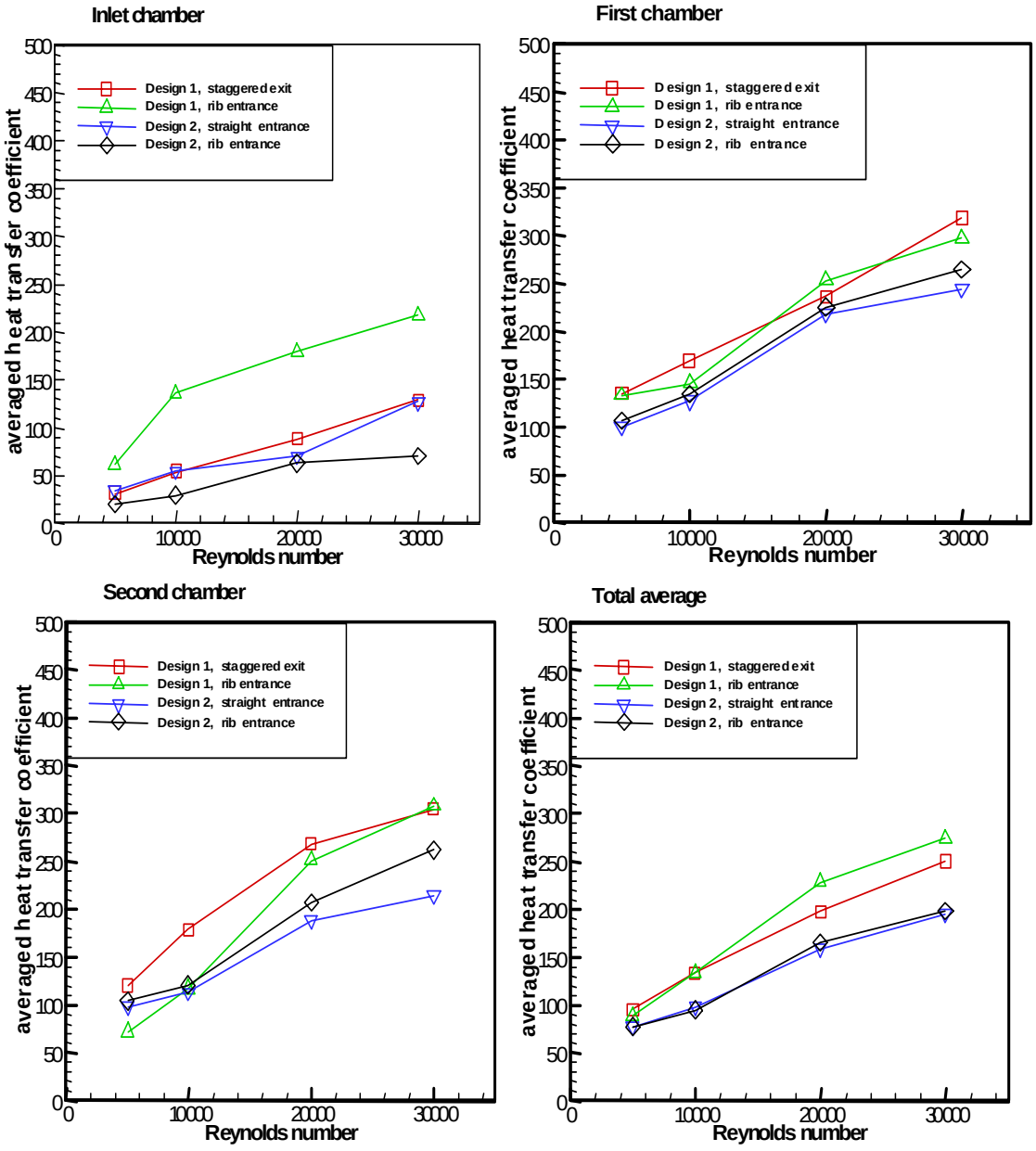

Fig. 35 Effect of the Design on Heat Transfer Coefficient at Each Chamber

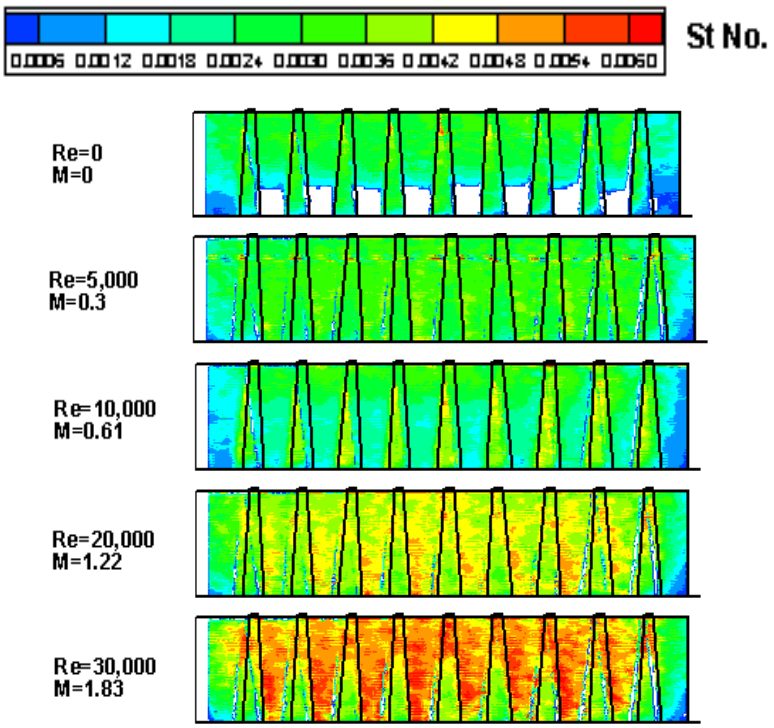

(a) Straight Entrance and Staggered Exit Slot in Design 1

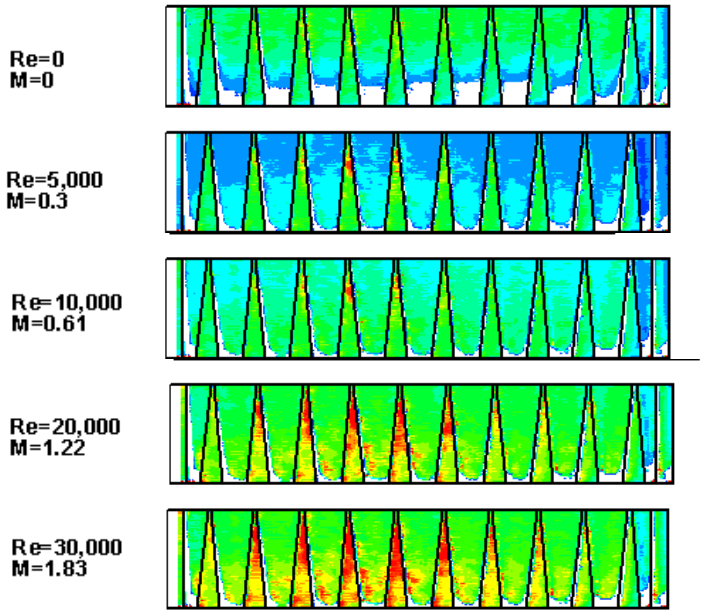

(b) Straight Entrance and Inline Exit Slot in Design 1

Fig. 36 Stanton Number Distributions with Low Turbulence Flow

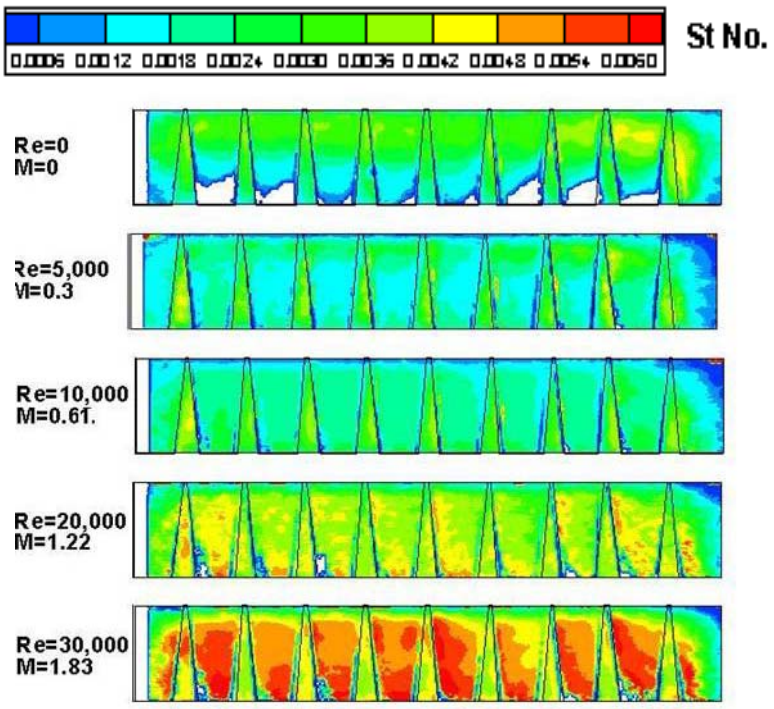

(c) Straight Entrance in Design 2

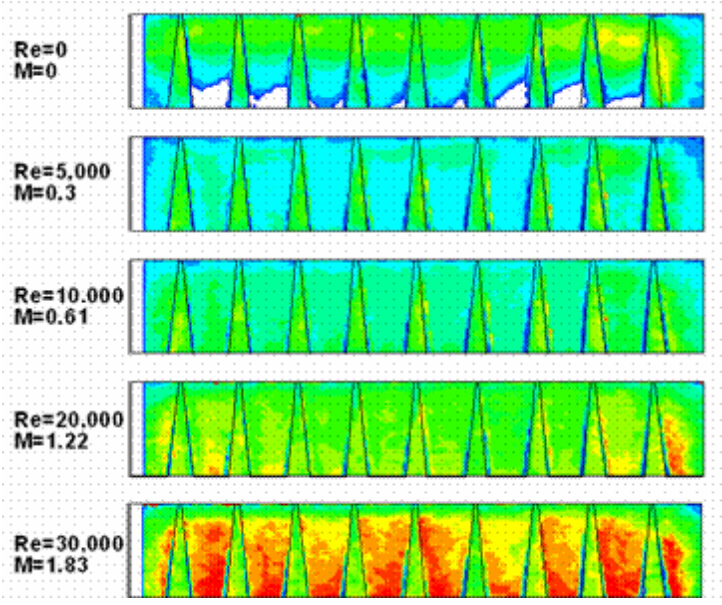

(d) Tapered Entrance Case in Design 2

Fig. 36 Continued

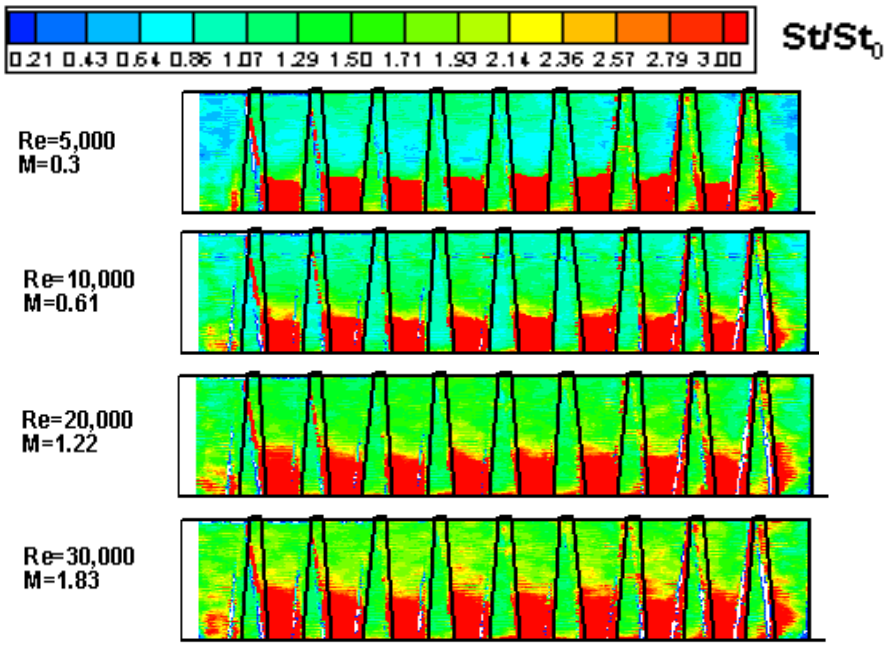

(a) Staggered Exit Slot in Design 1

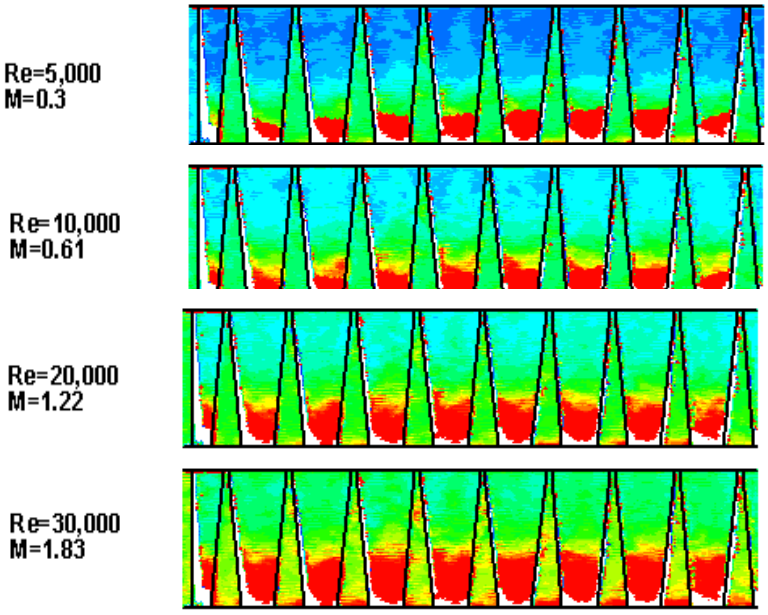

(b) Inline Exit Slot in Design 1

Fig. 37 Stanton Number Ratio Distributions with Low Turbulence Flow

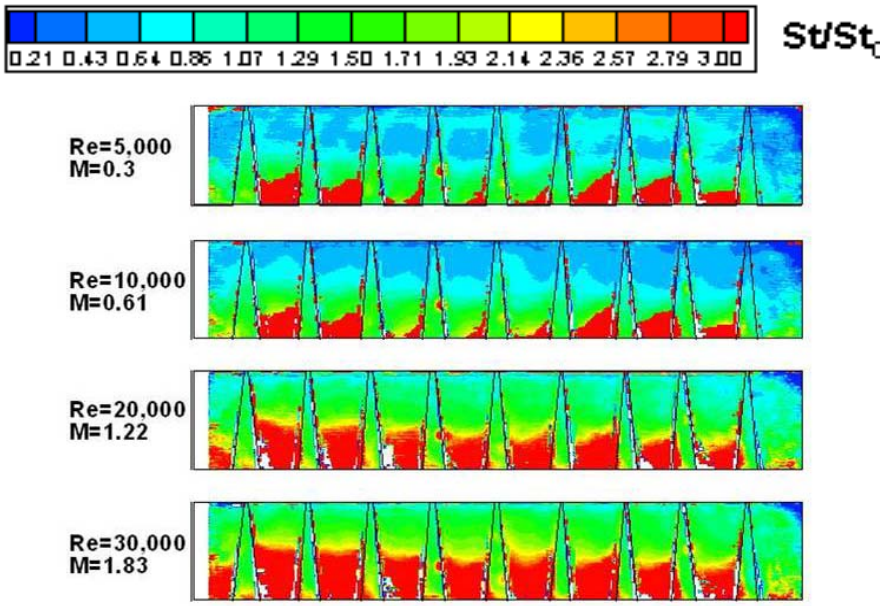

(c) Straight Entrance in Design 2

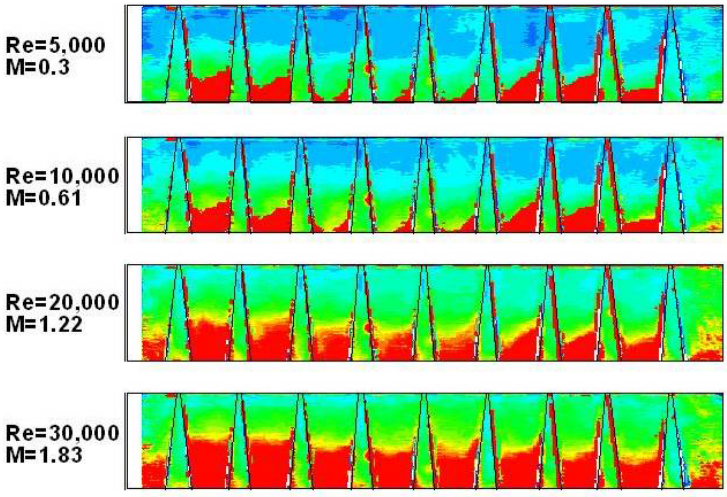

(d) Tapered Entrance in Design 2

Fig. 37 Continued

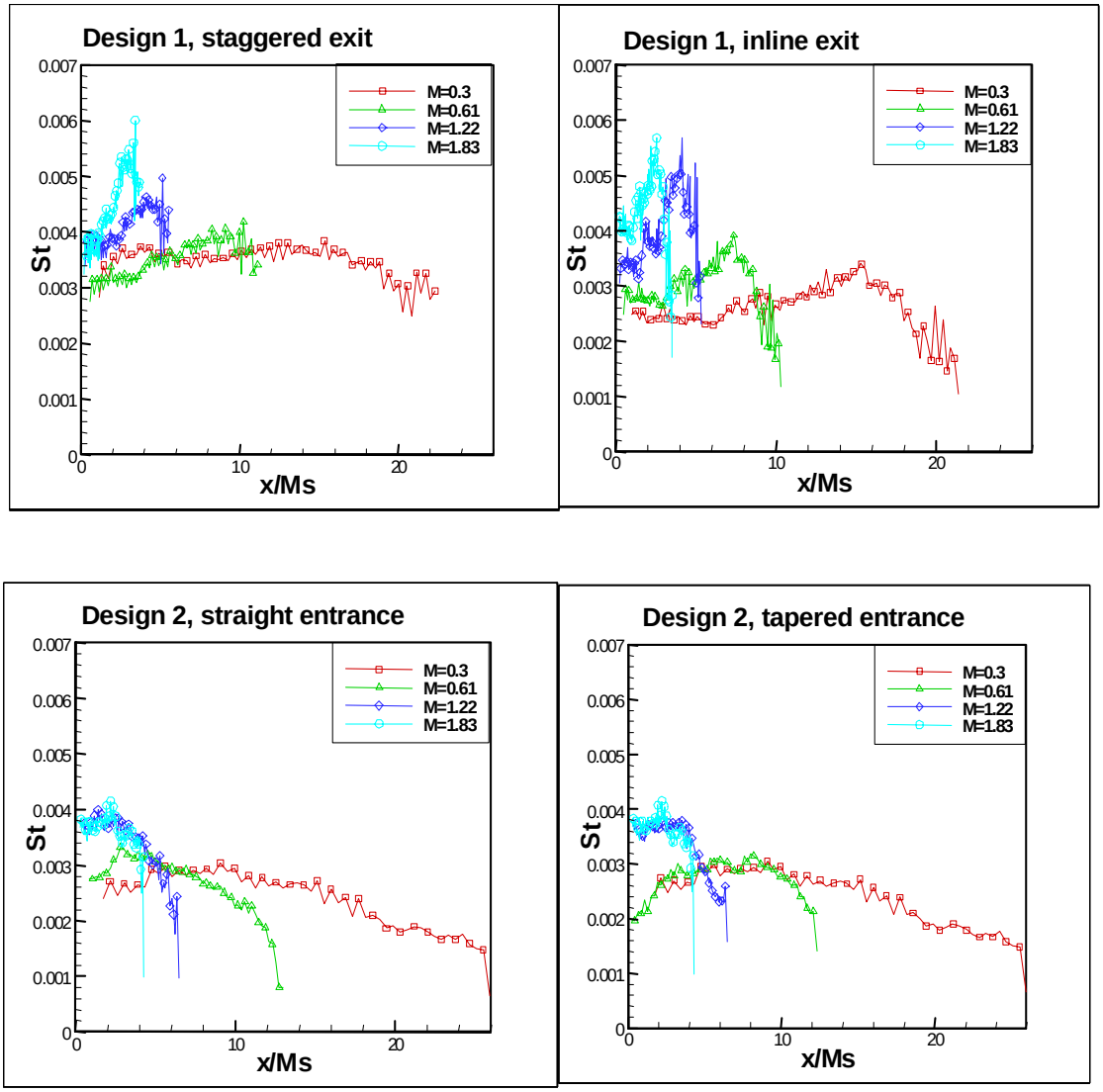

(a) Land Only

Fig. 38 Spanwise Averaged Stanton Number with Low Turbulence Flow

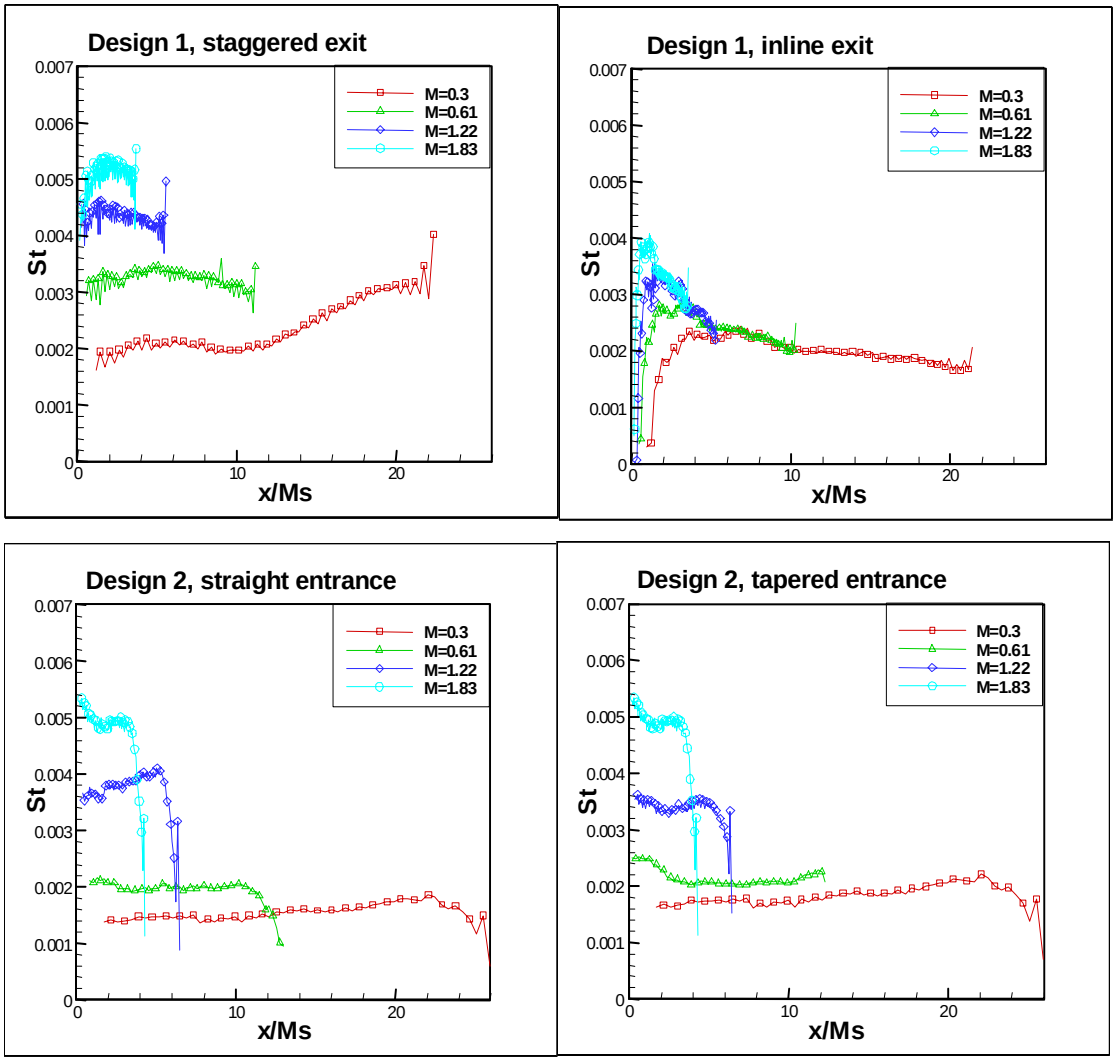

(b) Slot Only

Fig. 38 Continued

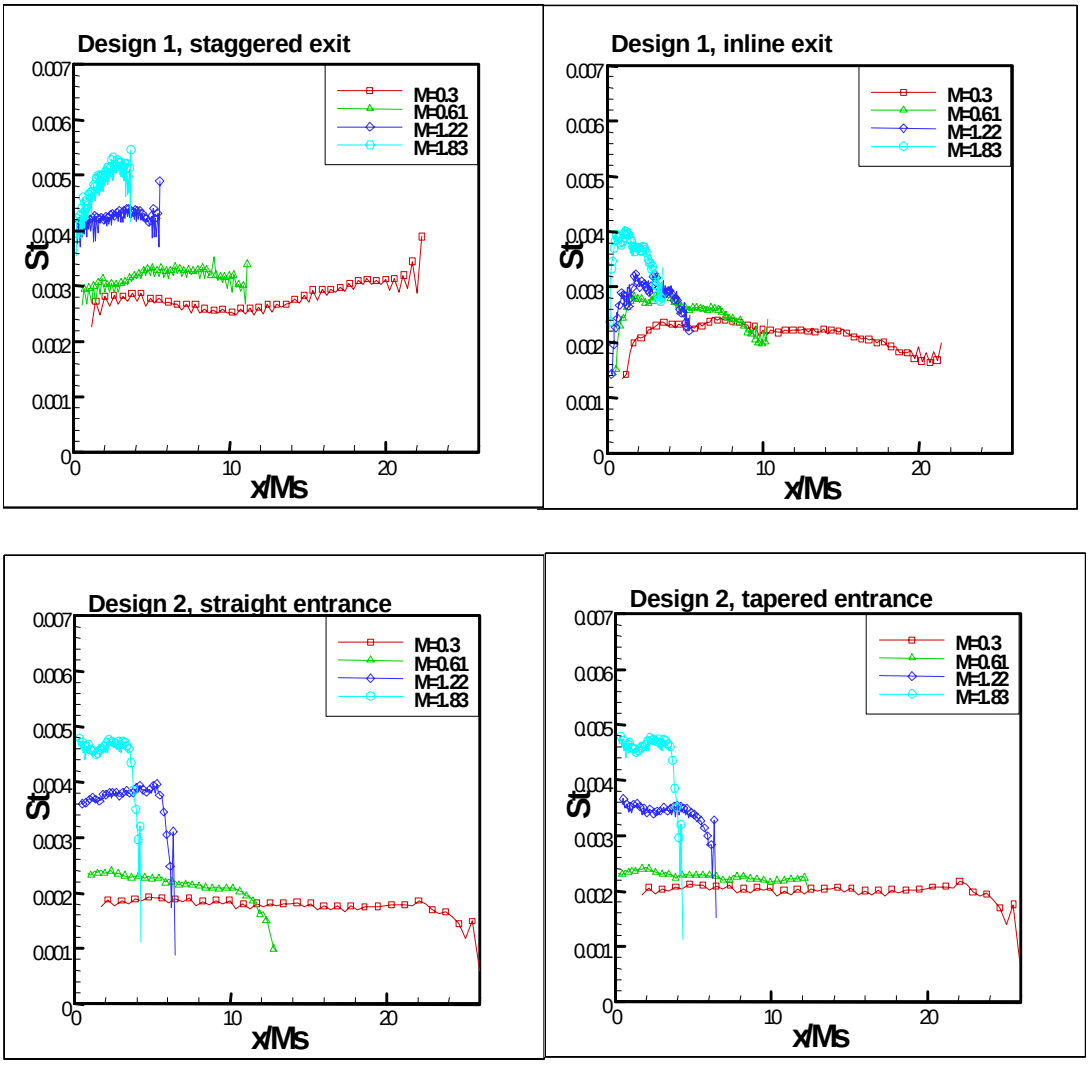

(c) Slots + Lands

Fig. 38 Continued

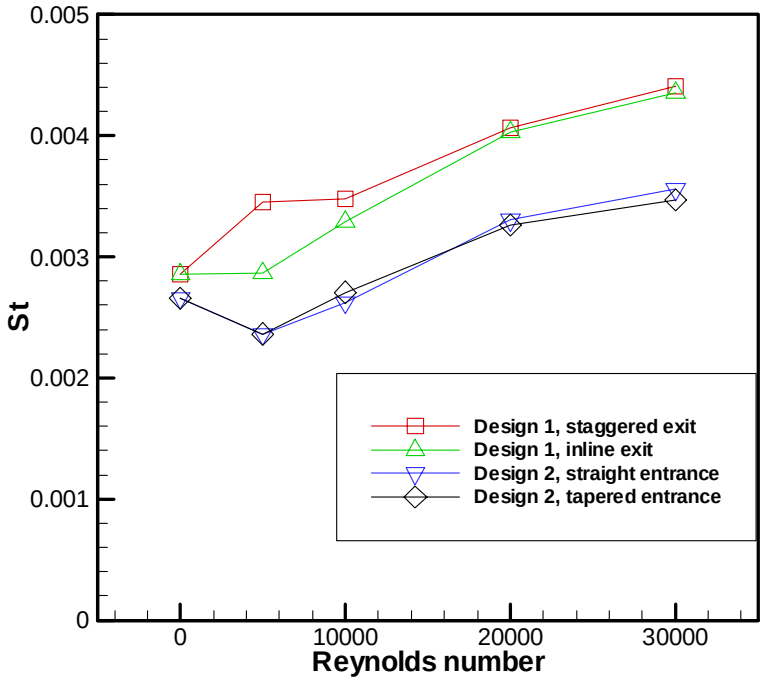

(a) Land Onlly

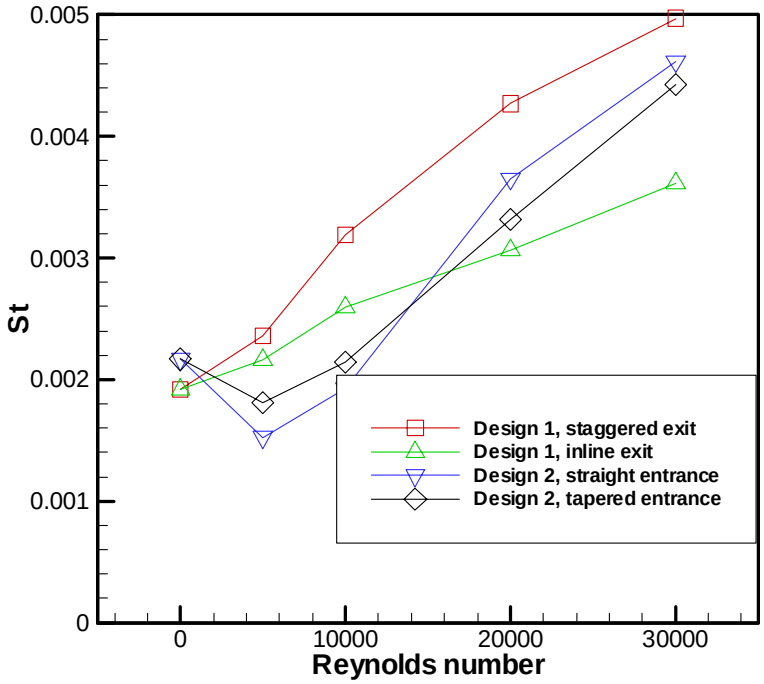

(b) Slot Only

Fig. 39 Average Stanton Number with Low Turbulence Flow

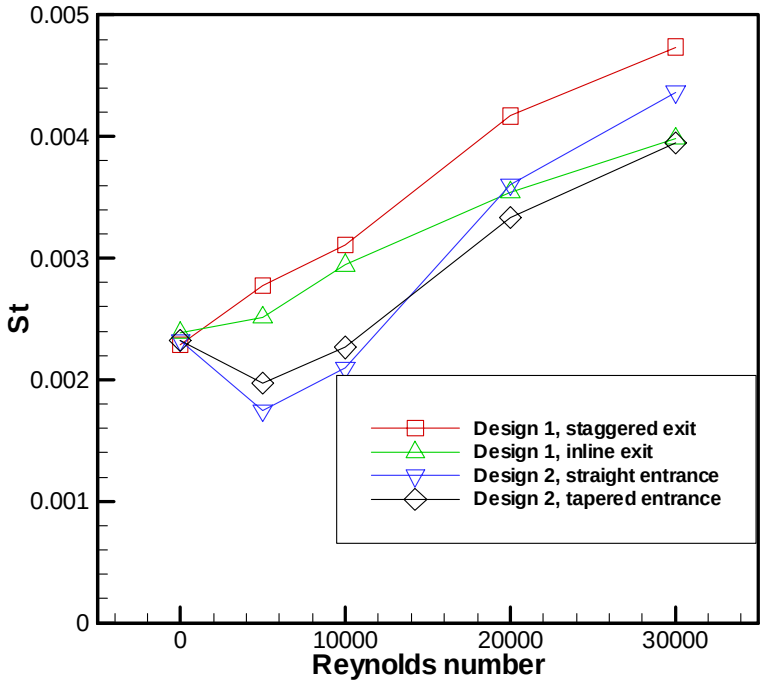

(c) Land + Slot

Fig. 39 Continued

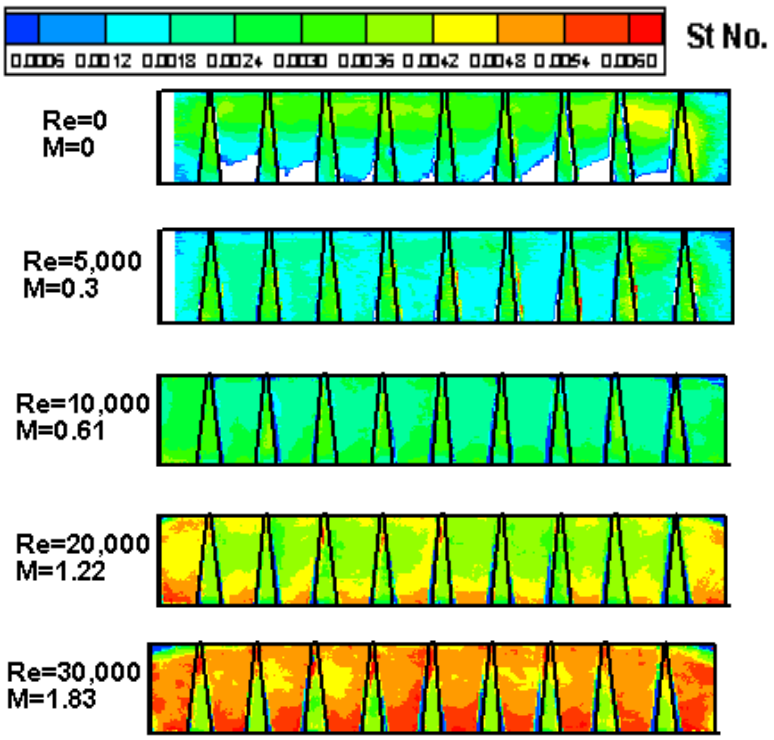

(a) Rib Entrance in Design 2

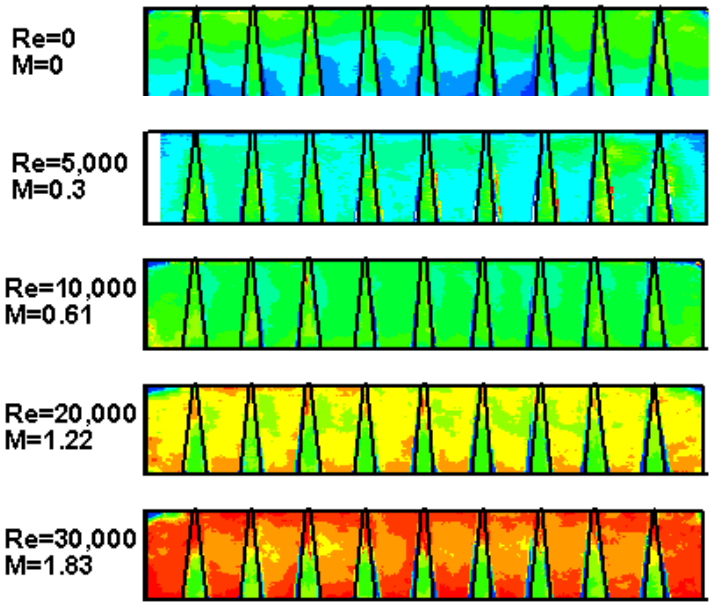

(b) Rib Entrance and turbulence grid in Design 2

Fig. 40 Stanton Number Distributions with High Turbulence Flow

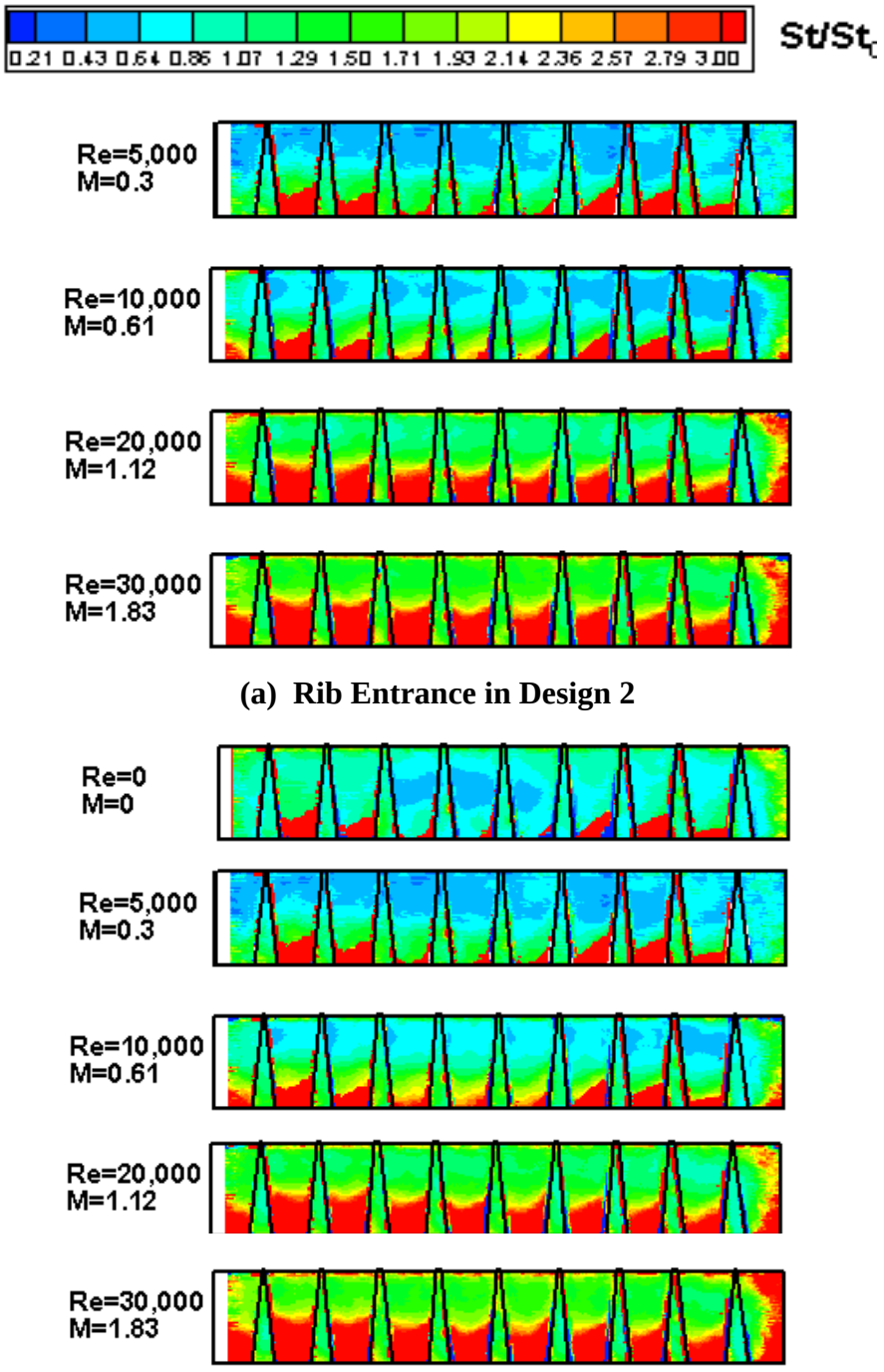

(a) Rib Entrance in Design 2

(b) Rib Entrance and turbulence grid in Design 2

Fig. 41 Stanton Number Ratio Distributions with High Turbulence Flow

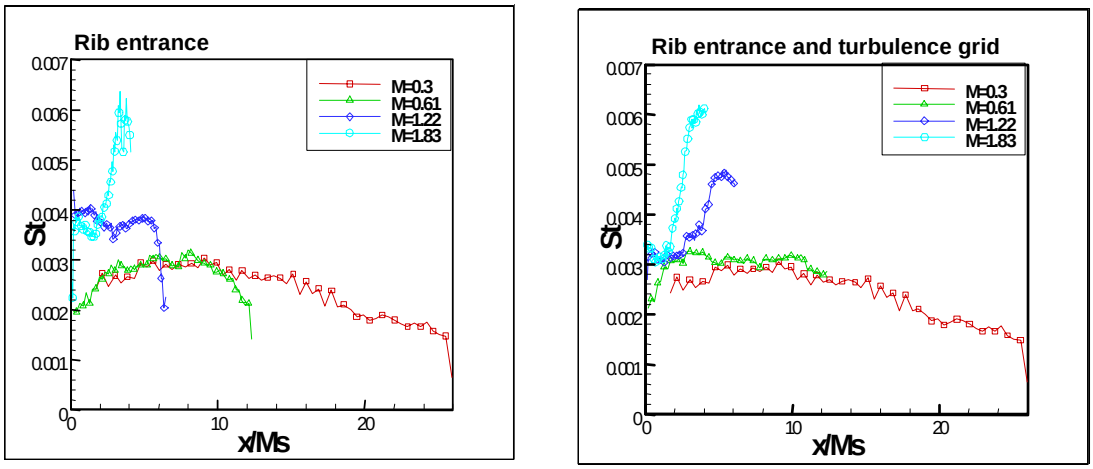

(a) Land Only in Design 2

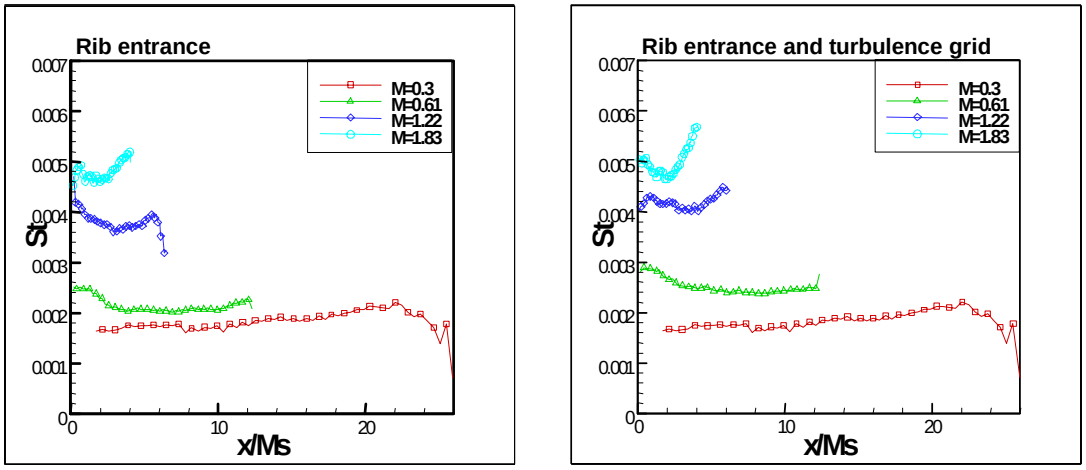

(b) Slot Only in Design 2

Fig. 42 Spanwise Averaged Stanton Number with High Turbulence Flow

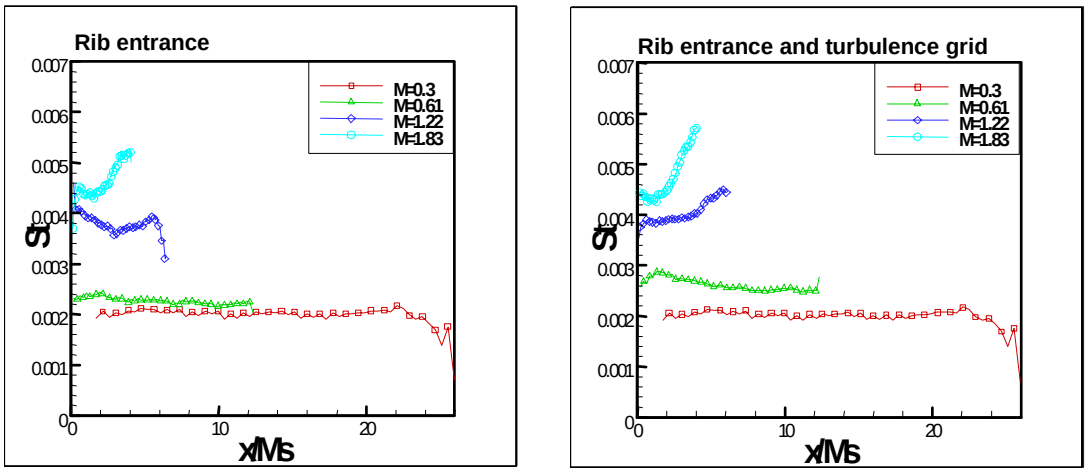

(c) Both slots and Land in Design 2

Fig. 42 Continued

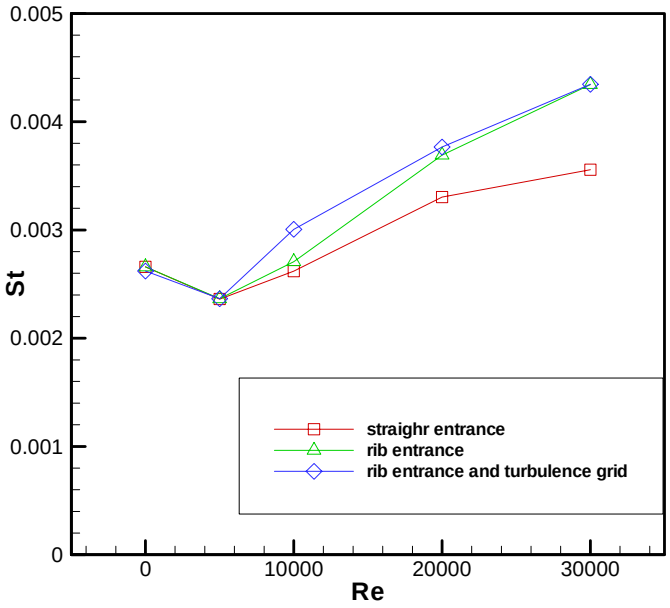

(a) Land

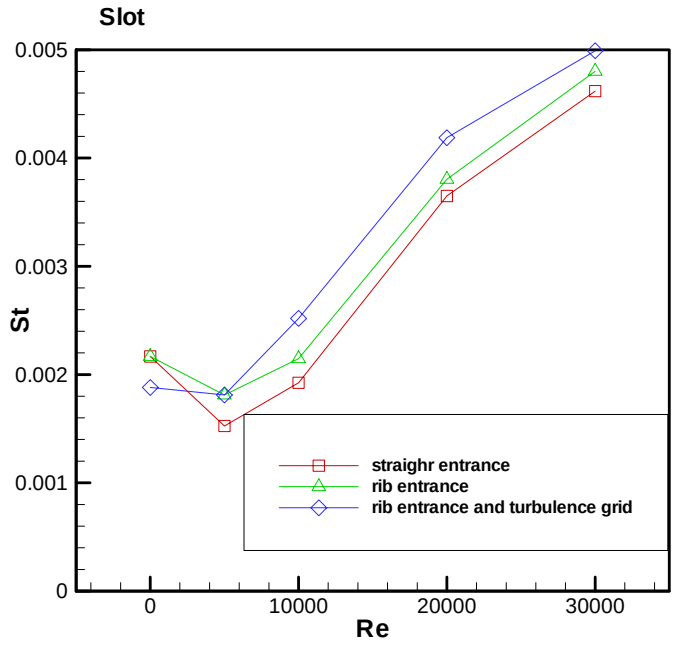

(b) Slot

Fig. 43 Average Stanton Number with High Turbulence Flow

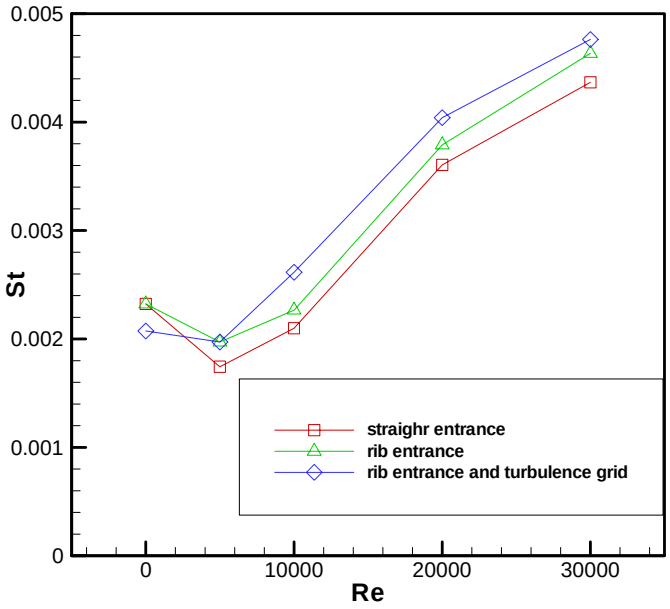

(c) Slot + Land

Fig. 43 Continued

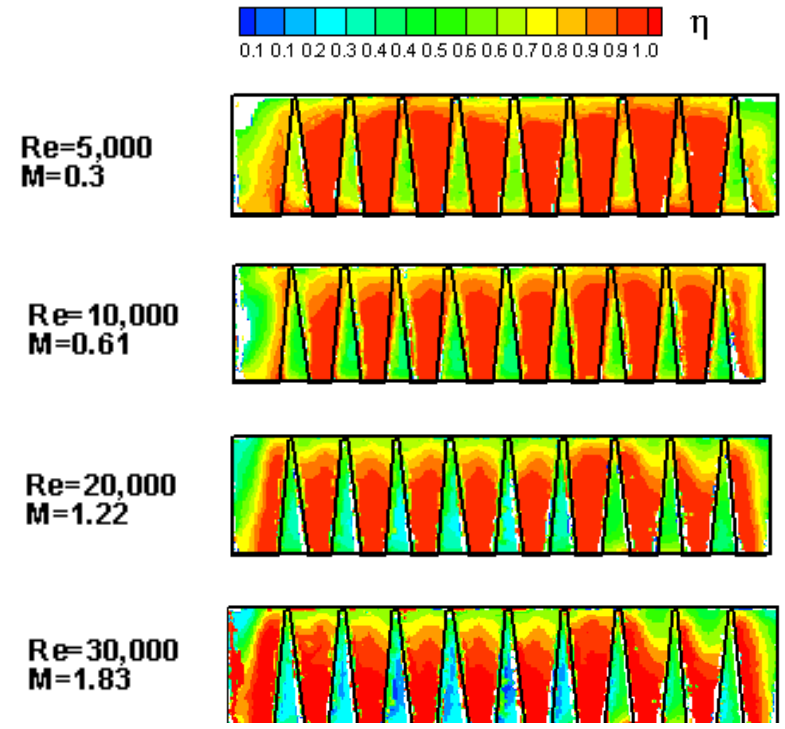

(a) Staggered Exit in Design 1

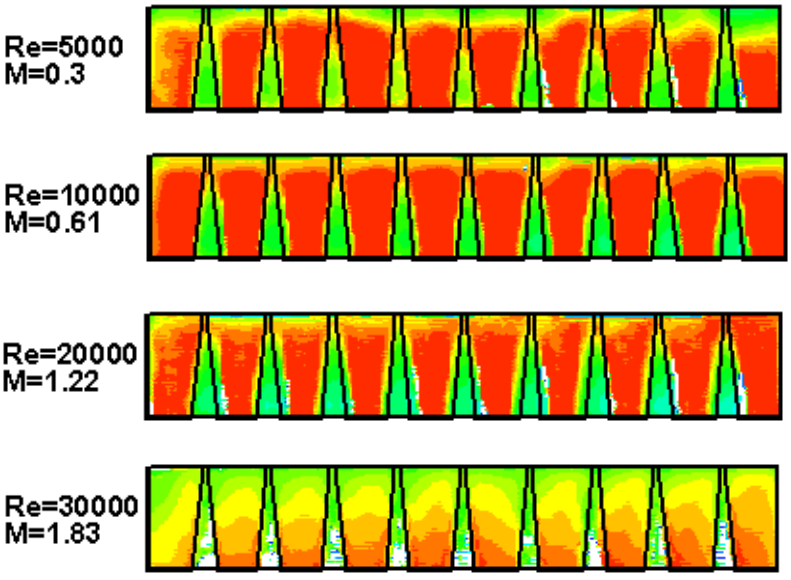

(b) Straight Entrance in Design 2

Fig. 44 Film Cooling Effectiveness with Low Turbulence Flow

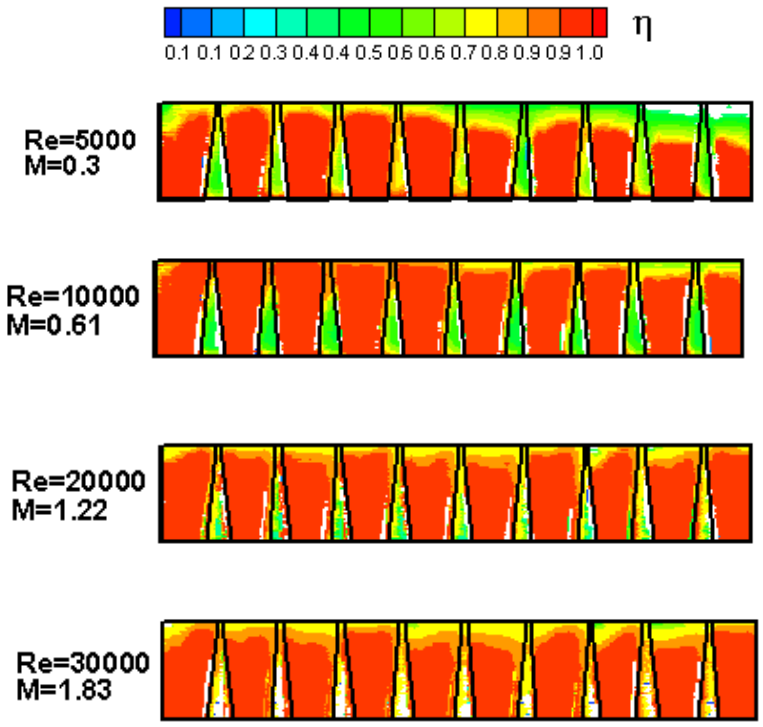

(c) Tapered Entrance in Design 2

Fig. 44 Continued

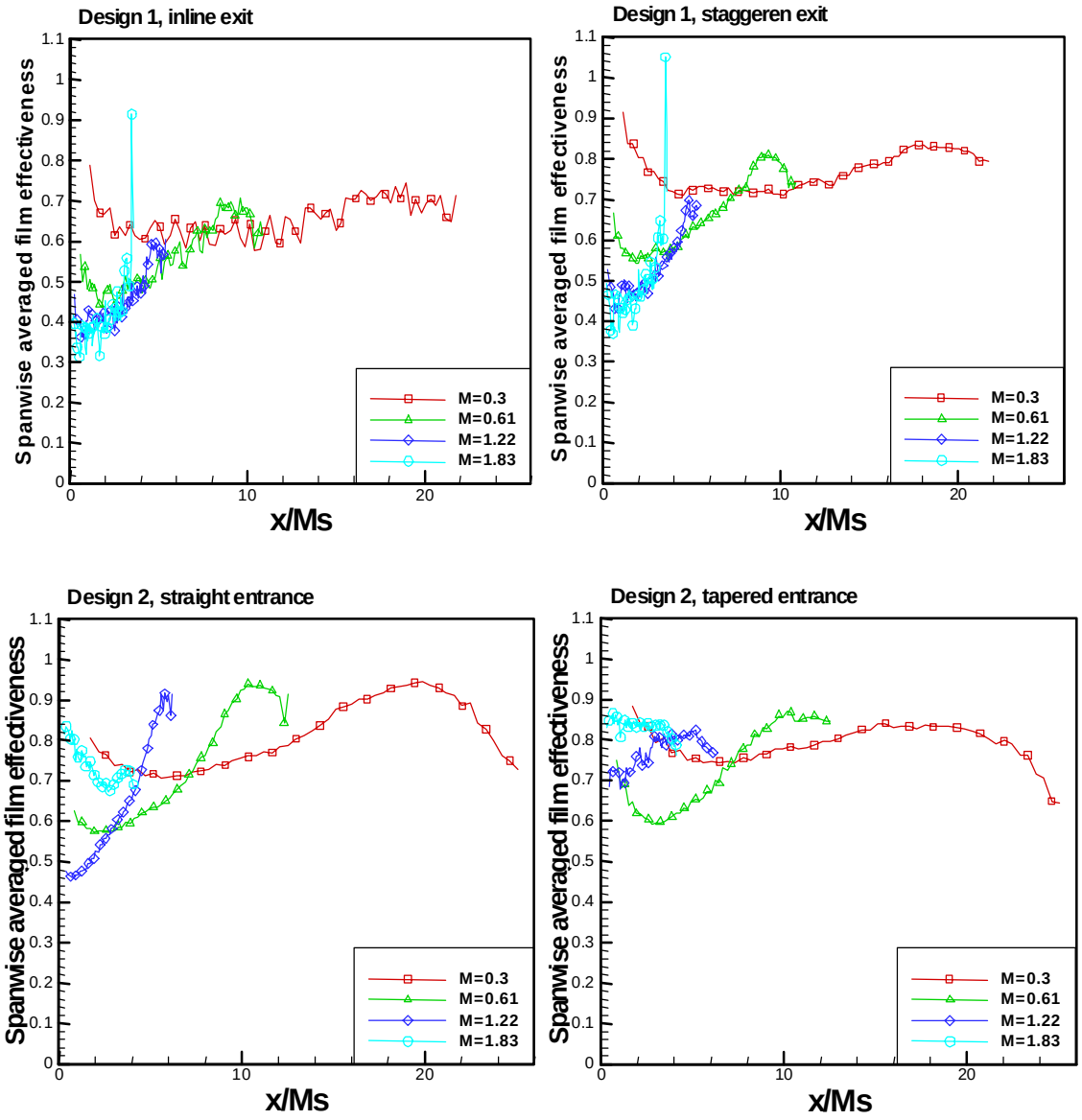

(a) Lands Only

Fig. 45 Spanwise Averaged Film Cooling Effectiveness with Low Turbulence Flow

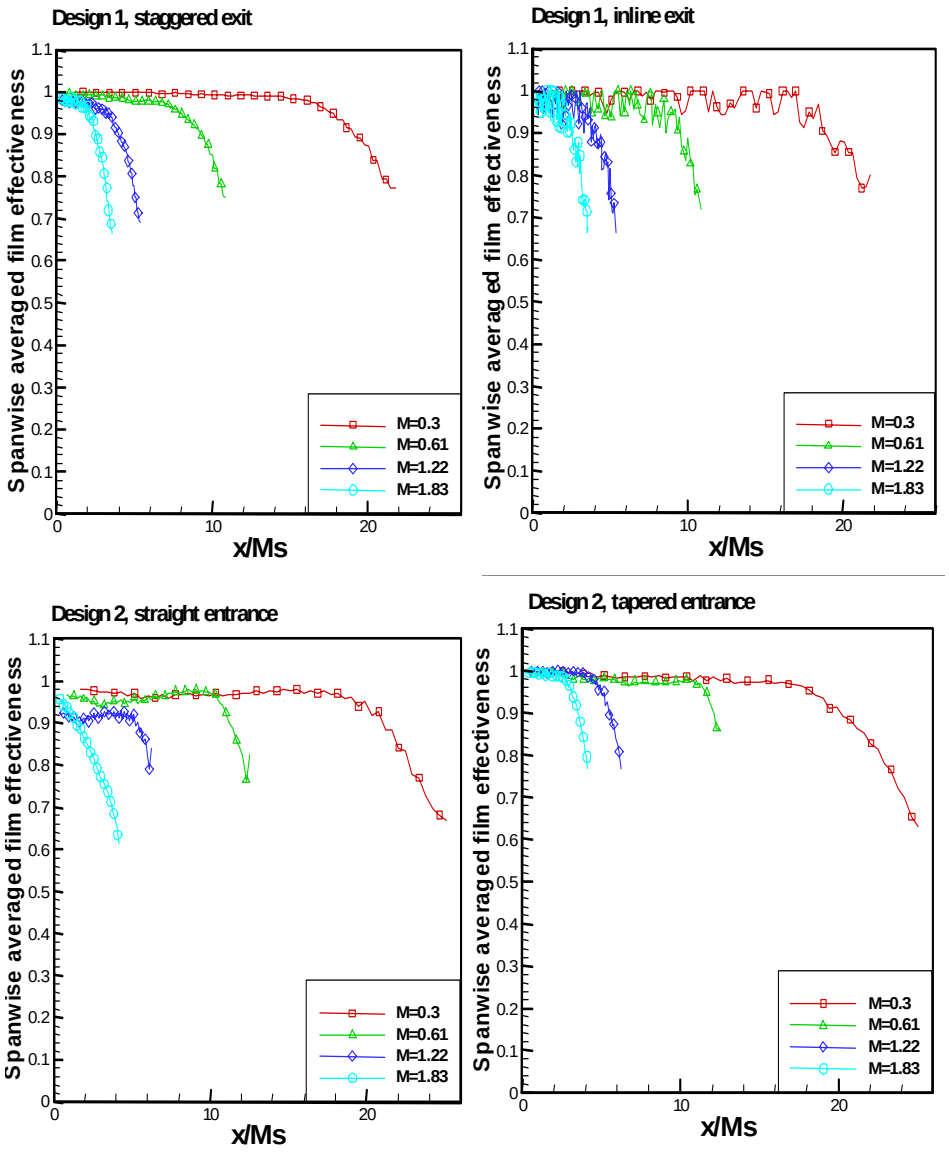

(b) Slot Only

Fig. 45 Continued

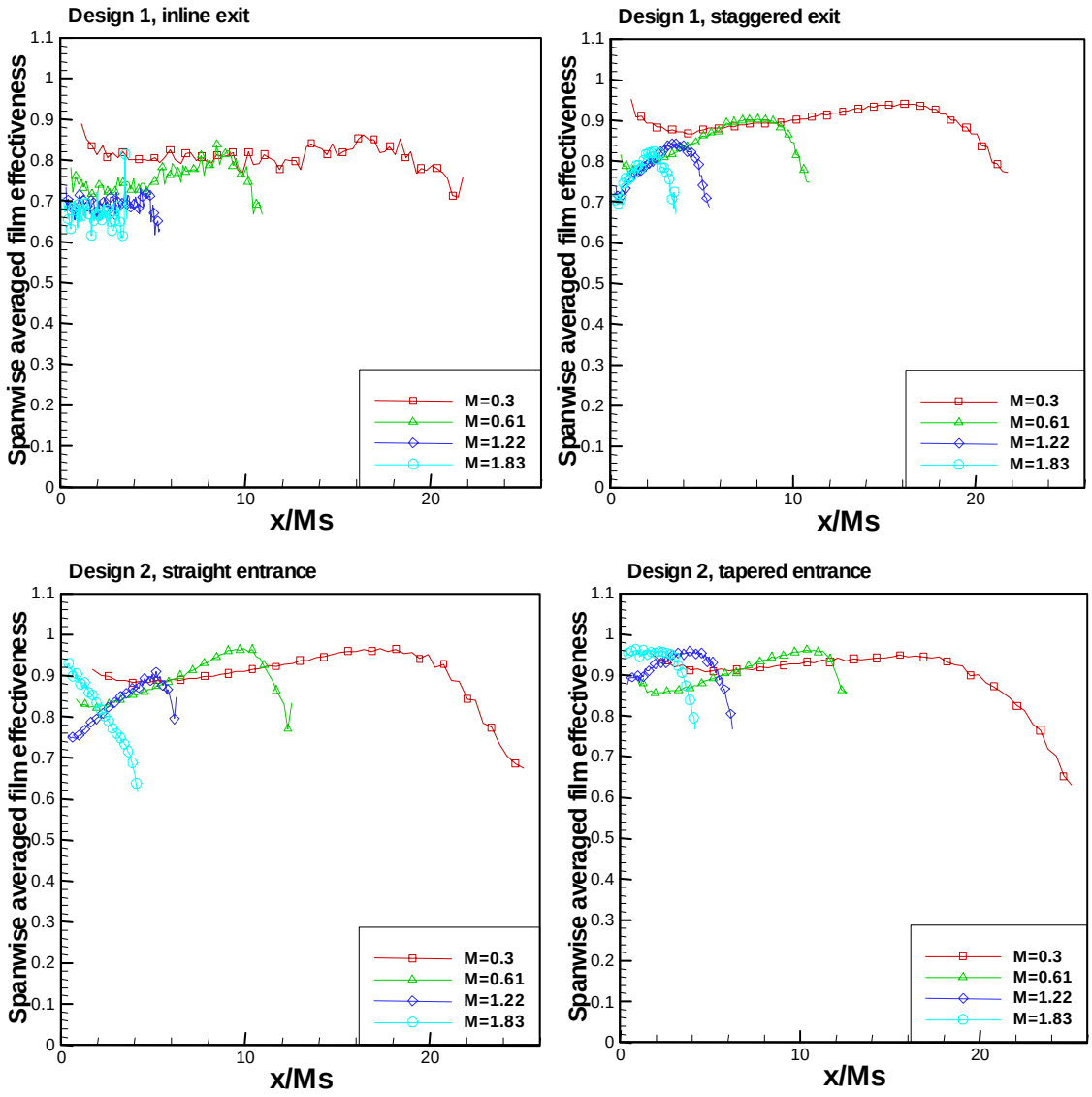

(c) Slots + Lands

Fig. 45 Continued

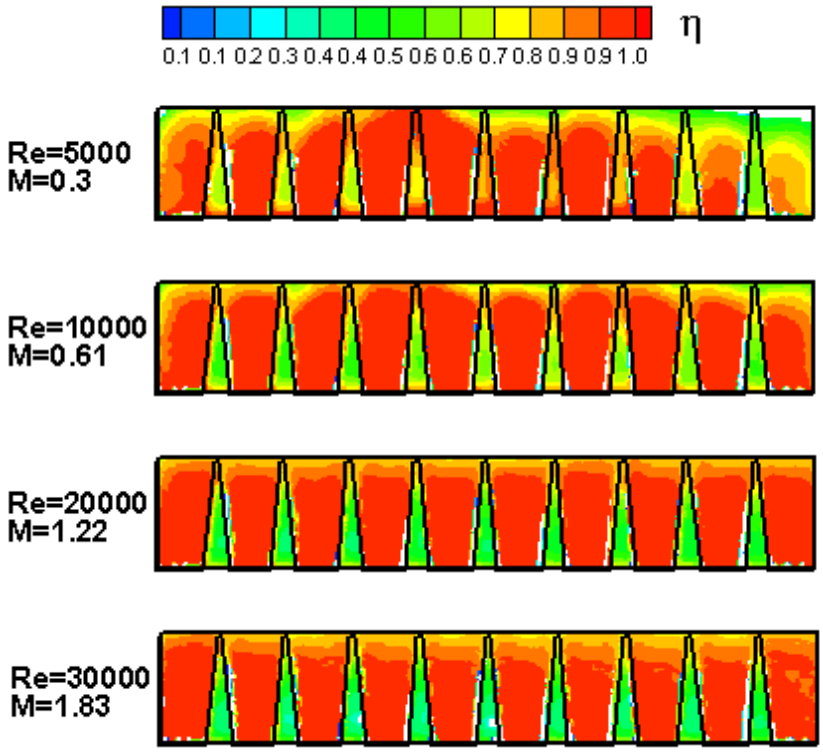

(a) Rib Entrance in Design 2

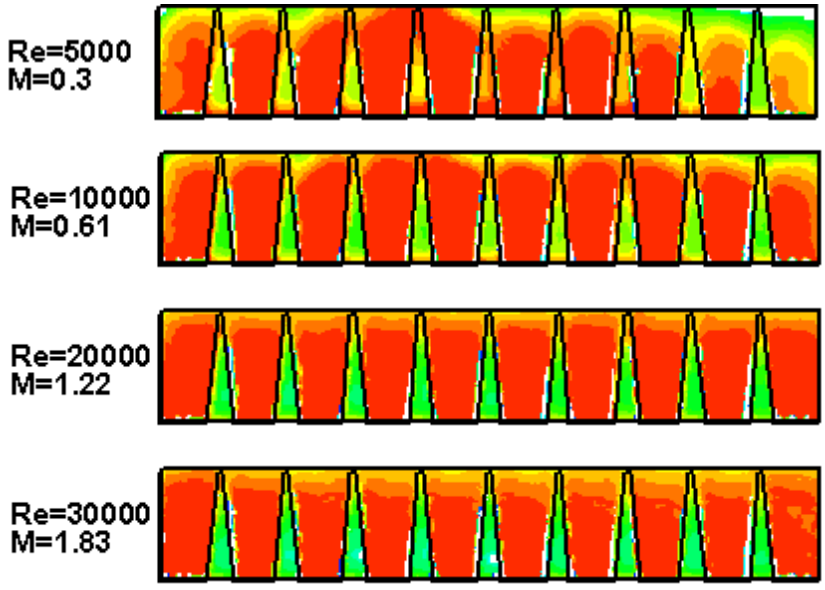

(b) Rib Entrance and Turbulence Grid in Design 2

Fig. 46 Film Cooling Effectiveness with High Turbulence Flow

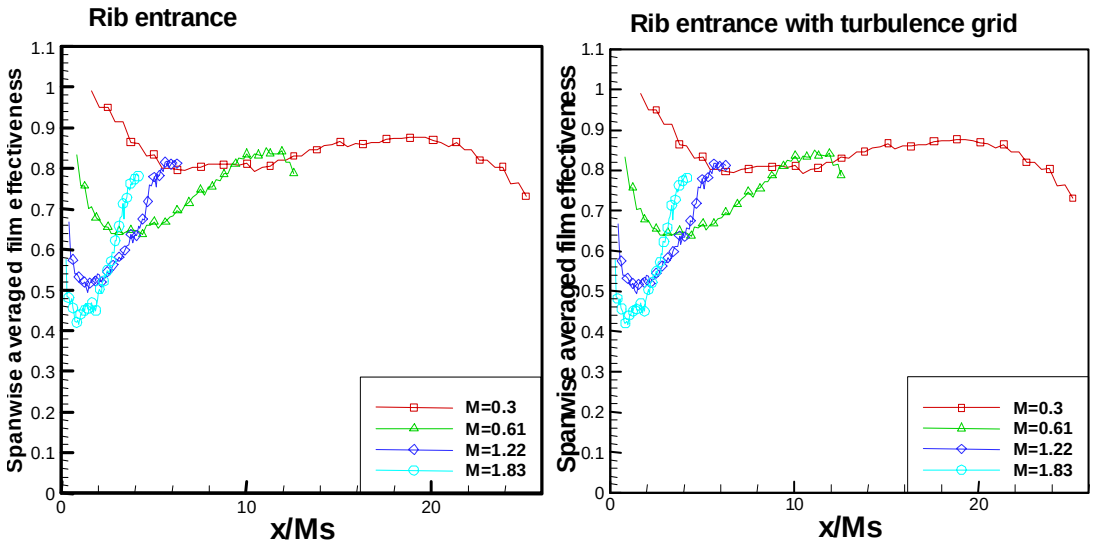

(a) Lands Only

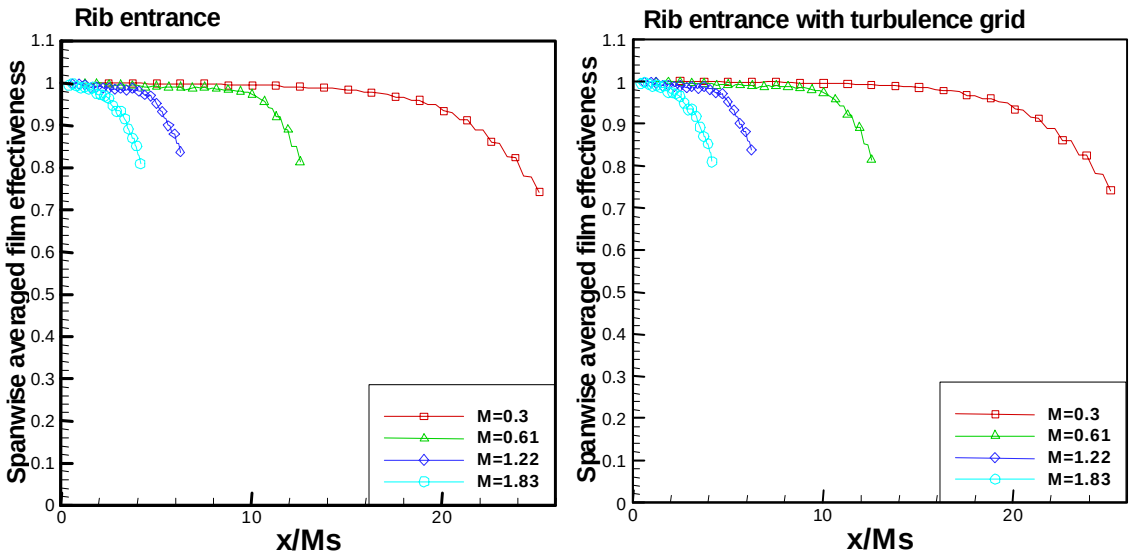

(b) Slot Only

Fig. 47 Spanwise Averaged Film Cooling Effectiveness with High Turbulence Flow

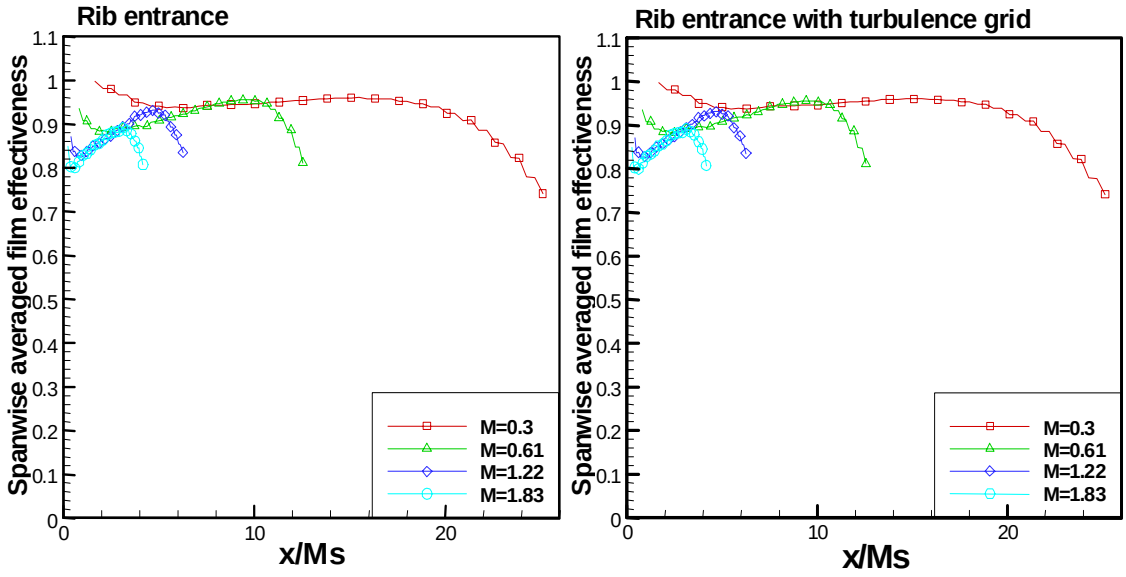

(c) (Slots + Lands)

Fig. 47 Continued

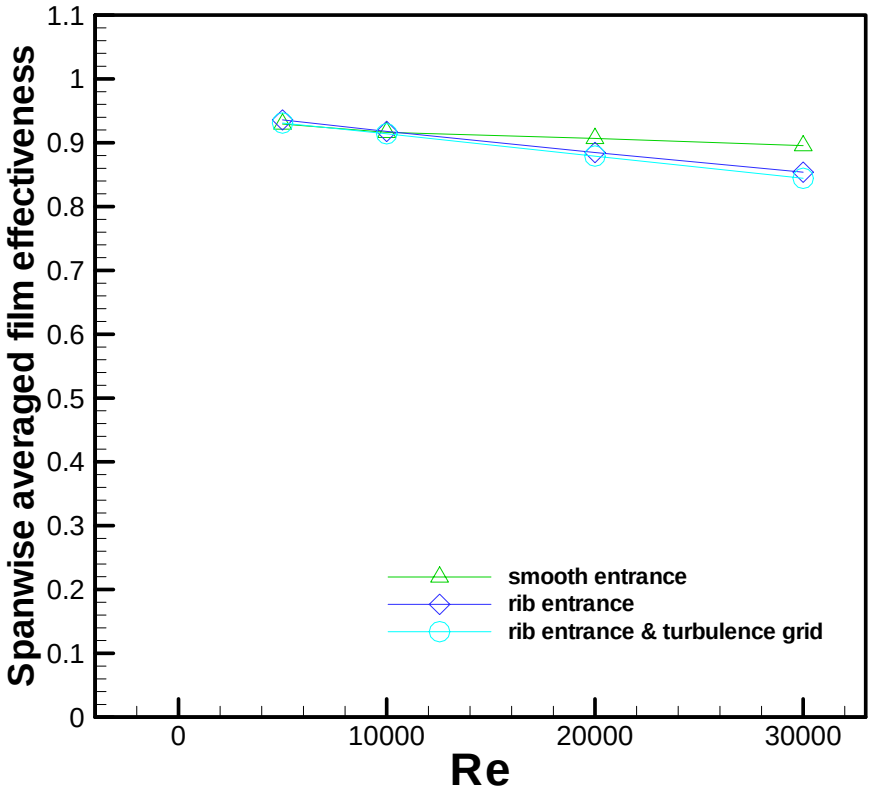

Fig. 48 Turbulence Effect on Spanwise Averaged Film Cooling Effectiveness

VITA

Name : Jungho Choi

Address : Jungbal-Gyungyoung-Bila 603-303, Ilsan, Koyang, Kyunggi, Korea

jungho_choi@hotmail.com

Education

Ph.D. in Mechanical Engineering – Texas A&M University, College Station, TX (December 2004)

M.S. in Mechanical Engineering – Hanyang University, Seoul, Korea (March 1998)

B.S. in Mechanical Engineering – Hanyang University, Seoul, Korea (March 1996)

Professional Experience

Research/Teaching Assistant - (2000 – 2004)

Provided assistance to professor in mechanical engineering course concentrating on research and hands-on application of gas dynamics and heat transfer concepts. Assisted students in conducting heat transfer and flow control experiments. Evaluated and provided assistance in completion of difficult assignments. As Research Assistant, assisted research team in evaluating performance of turbine blade upon introduction of various outside factors. Analyzed and recorded results of wake effect, as well as internal/external heat transfer, and film-cooling on turbine blade trailing edge.